UNIVERSITY OF LIEGE
Faculty of Sciences
Unit of Geomatics

Promoter Pr. R. Warnant

Modelling the Mid-latitude Ionosphere: Assessment of the NeQuick Model using GPS TEC and Ionosonde Data

---

Benoît Bidaine
Master thesis submitted in fulfilment of the
in-depth study diploma in sciences
B.Bidaine@ulg.ac.be

Academic year 2006 - 2007

UNIVERSITY OF LIEGE
Faculty of Sciences
Unit of Geomatics

Promoter Pr. R. Warnant

Modelling the Mid-latitude Ionosphere: Assessment of the NeQuick Model using GPS TEC and Ionosonde Data

Benoît Bidaine
Master thesis submitted in fulfilment of the
in-depth study diploma in sciences
B.Bidaine@ulg.ac.be

Academic year 2006 - 2007

Modelling the Mid-latitude Ionosphere: Assessment of the NeQuick Model using GPS TEC and Ionosonde Data

The **ionosphere** plays a crucial role in Global Navigation Satellite Systems (GNSS) accuracy. In extreme cases, this electrically charged part of the atmosphere can lead to **errors in positioning** exceeding 100 m. At first approximation, ionospheric effects depend mainly on the total content in free electrons of the ionosphere ("total electron content", TEC) defined as the integral of the electron density on the path between the satellite and the receiver.

The modelling of the latter parameter reveals thus itself critical in particular for **single frequency receivers**, the most common ones constituting the mass market. In the framework of GALILEO, the European system in development, the **NeQuick model** has been chosen to this extent. Computing monthly median electron densities as a basis, it will be integrated into a global algorithm providing the users with daily updated information and allowing them to calculate TEC and thus to mitigate the ionospheric effects.

In order to reach the specified correction level, the model itself and its latest evolutions as well as its use for GALILEO are **investigated**. Different situations have to be considered e.g. different latitude regions and the results can be compared to various data sets.

As a first step in a thorough analysis, we take benefit of **ionosonde and GPS TEC data** from the Dourbes Geophysical Observatory (Belgium) to study the mid-latitudes. Constraining the model with ionosonde measurements, we first investigate the difference between GPS-derived vertical TEC (vTEC) for Dourbes station and corresponding values from NeQuick for the latest years (for solar maximum in 2002 and minimum in 2006). With this approach, we reach **residual errors of about 20% RMS for 2002 and 30% for 2006** keeping in mind that TEC values are far lower in this low solar activity year.

Through a **focusing process**, we identify then gradually best and worst months and days for which we observe the evolution between two versions of NeQuick. We highlight among others **improvements from the latest modification in the topside formulation** which appears clearly in the electron density profiles examined at the end of the assessment.

Benoît Bidaine
Master thesis submitted in fulfilment of the
in-depth study diploma in sciences

Board of supervisors

R. Warnant	R. Billen	J.-C. Gérard
Professor	Professor	Professor
ULg (FS/Geomatics)	ULg (FS/Geomatics)	ULg (FS/AGO)
Promoter	Member	Member

Modéliser l'ionosphère aux latitudes moyennes : évaluation du modèle NeQuick au moyen de données de TEC GPS et d'ionosonde

L'**ionosphère** joue un rôle crucial pour la précision des systèmes globaux de navigation par satellite (GNSS). Dans des cas extrêmes, cette partie de l'atmosphère chargée électriquement peut mener à des **erreurs de positionnement** dépassant 100 m. En première approximation, les effets ionosphériques dépendent principalement du contenu total en électrons libres de l'ionosphère ("total electron content", TEC) défini comme l'intégrale de la densité électronique sur le trajet entre le satellite et le récepteur.

La modélisation de ce dernier paramètre se révèle donc critique en particulier pour les **récepteurs simple fréquence**, les plus courants constituant le marché de masse. Dans le cadre de GALILEO, le système européen en développement, le **modèle NeQuick** a été choisi à cette fin. Calculant des densités électroniques mensuelles médianes à la base, il sera intégré à un algorithme global fournissant aux utilisateurs des informations mises à jour de manière journalière et leur permettant de calculer le TEC donc d'atténuer les effets ionosphériques.

Afin d'atteindre le niveau de correction requis, le modèle lui-même et ses dernières évolutions ainsi que son utilisation pour GALILEO sont **étudiés**. Différentes situations doivent être considérées, par exemple des régions de différentes latitudes, et les résultats doivent être comparés à divers ensembles de données.

Comme première étape d'une évaluation complète, nous tirons parti de **données d'ionosonde et de TEC GPS** du Centre de Physique du Globe à Dourbes (Belgique) pour étudier les latitudes moyennes. Conditionnant le modèle avec des mesures d'ionosonde, nous analysons la différence entre le TEC vertical obtenu par GPS pour la station de Dourbes et les valeurs correspondantes provenant de NeQuick pour les dernières années (pour le maximum solaire en 2002 et le minimum en 2006). Avec cette approche, nous atteignons des **erreurs résiduelles d'environ 20% RMS pour 2002 et 30% pour 2006** gardant à l'esprit que les valeurs de TEC sont bien plus faibles au cours de cette année de faible activité solaire.

A travers un **processus de focalisation**, nous identifions ensuite graduellement les meilleurs et moins bons mois et jours pour lesquels nous observons l'évolution entre deux versions de NeQuick. Nous mettons entre autres en évidence les améliorations obtenues grâce à la **dernière modification dans la formulation de la couche supérieure** de l'ionosphère qui apparaît clairement dans les profils de densité électronique examinés à la fin de l'évaluation.

Benoît Bidaine
Master thesis submitted in fulfilment of the
in-depth study diploma in sciences

Jury

R. Warnant	R. Billen	J.-C. Gérard
Professeur	Professeur	Professeur
ULg (FS/Géomatique)	ULg (FS/Géomatique)	ULg (FS/AGO)
Promoteur	Membre	Membre

Acknowledgements

What a small world!

I had indeed to go abroad for three months to get to know such enthusiastic people from a few buildings away from my classrooms beginning with my promoter, René Warnant, towards who I am very grateful. About one year ago he gave me the opportunity to join the Geomatics team where working becomes a pleasure.

I wish also to acknowledge

Michaël Bavier and Luc Lejeune from RMI who provided me with data and explanations about them,

Sandro Radicella, Pierdavide Coïsson and Bruno Nava from ICTP in Trieste for their wise comments about NeQuick of which they entrusted the latest version to me,

Alison, Anne-Marie, Eric and all the people who supported me in my task and I could have forgotten.

My final thoughts go to Reinhart Leitinger whose knowledge I would have really been honoured to share.

Contents

Chapter 1

Introduction

As a **young Belgian scientist working in the space field**, I like to learn about this medium in which I take my first steps. Once I was looking for information about ionosphere modelling, I found out that some Belgians played a major role in that topic. Luc Bossy for example, born in the old village of Fosse-sur-Salm near Malmedy in 1918, has been working at the Royal Meteorological Institute (RMI) after the Second World War till 1983 and chaired between 1984 and 1992 the task group in charge of the International Reference Ionosphere (IRI) model.

To a broader extent, Belgium has always attached a great importance to Space. Our country appears for example among the founder members of the European Space Agency (ESA) which is currently developing the European Global Navigation Satellite System (GNSS) named **GALILEO**. This project based on Earth-space radiowave propagation involves also **ionosphere modelling** as this part of the atmosphere can lead to *errors in positioning* exceeding 100 m. Its intrinsic electron concentration affects indeed the time of flight of navigation signals depending on their frequency and on the total content in free electrons of the ionosphere.

This slant *"total electron content"* (sTEC) is defined as the integral of the electron density on the path between the satellite and the receiver. Its modelling reveals itself of first importance in particular for *single frequency receivers*, the most common ones constituting the mass market, but also for multiple-frequency devices. The latest will indeed comprise a *fallback mode* in single frequency within the framework of critical applications such as civil aviation where the level of precision must be guaranteed in all circumstances.

The framework is then set as my work deals about the ionospheric error correction algorithm for GALILEO single frequency users and in particular its underlying model **NeQuick**. Understanding its *weaknesses and evolutions* and *validating* its results constitutes indeed a task of prime order to reach the best correction level. Therefore *different situations* have to be considered: different latitude regions (space conditions), different hours, seasons and years (time conditions) and specific phenomena occurrence (magnetic storms, Travelling Ionospheric Disturbances - TIDs). In addition the results can be compared to *different data sets* among which GPS slant or vertical TEC measurements, Global Ionospheric Maps, ionosonde profiles, topside soundings but also other ionosphere models results such as IRI. I chose as a first step to investigate NeQuick performance at mid-latitudes using ionosonde and GPS TEC data.

In the present document, we first introduce the **main concepts about the ionosphere**, its influence, modelling and probing (chapter 2). Consisting of a highly variable plasma, its *variations* are considered among which spatial and temporal structure but also disturbances and irregularities which generally raise difficulties for the models. We get then familiar with the ionospheric *effects* on radiowave propagation and on GNSS in particular which are also presented summarily. The NeQuick *model*, providing a monthly median representation, and its use for GALILEO on a daily basis are approached before some details about the *measurement* techniques generating ionosonde and GPS TEC data.

Chapter 3 describes **NeQuick assessment** which exploits on the one hand a major advantage of NeQuick by comparison to other models. Its basic output consists indeed in the electron density then integrated to obtain TEC which allows to compare two parameters. On the other hand we take benefit of collocated measurements from the Dourbes Observatory (Belgium) where ionosonde and GPS TEC data are available on a period of more than one solar cycle. After a *methodology* description, we investigate the difference between GPS-derived and modelled *vertical TEC* for two years of opposite solar activity levels and for several months in these years. For these months, we select *case days* for which we deepen the analysis considering daily TEC graphs. Finally we compare *electron density profiles* from the ionosonde and the two considered versions of NeQuick.

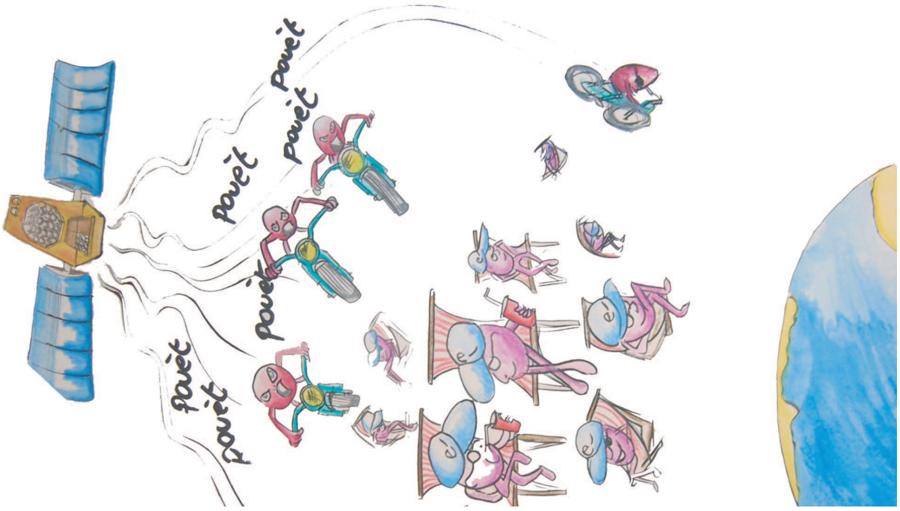

Chapter 2

The ionosphere

2.1 Description

2.1.1 Definition and formation

> The ionosphere is defined, for our purposes, as that part of the upper atmosphere where sufficient ionization can exist to **affect the propagation of radio waves** [Davies, 1990, Chap. 1].

This definition reveals particularly well the intrinsic link binding the ionosphere to its effects and the context of this study. Among different classifications following different criteria (cf. figure 2.1), this atmospheric region is indeed opposed for propagation purposes to the abusively called troposphere even if most of its constituents are electrically neutral.

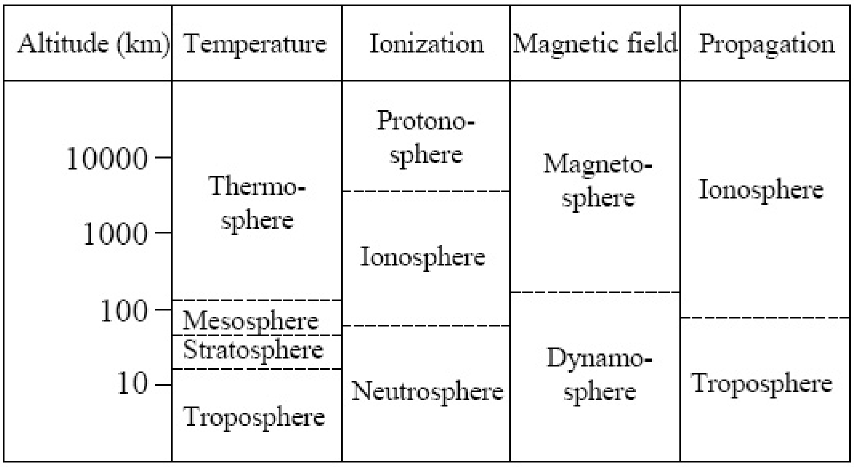

Figure 2.1: Possible subdivisions of the Earth's atmosphere [Odijk, 2002]

The description of its forming and evolution takes into account several **processes** mainly

- photoionization for which X and extreme ultraviolet (EUV) rays tear off electrons from neutral atoms and molecules, leaving free electrons and positive ions ;
- recombination, the inverse reaction ;
- and capture forming negative ions from neutral particles and free electrons.

The competition between these phenomena, depending on space and time, results in a highly variable **electron density** Ne, the major ionospheric characteristic. This parameter can be integrated along a vertical path resulting in the **Total Electron Content (TEC)** which will retain all our interest for its wide use in the evaluation of the ionospheric effects in satellite navigation.

2.1.2 Spatial structure

A first compromise we can observe gives its **vertical structure** to the electron density profile (cf. figure 2.2). Indeed the ionization level raises with height whereas the atmospheric constituents density decreases with altitude giving birth to a peak of electron concentration. The latter plays a crucial role in ionosphere description and effects and is commonly used to divide the profile into its lower and upper parts i.e. the bottom and topsides.

To be accurate, the electron density at a certain height depends mostly on coexisting atmospheric components and type of solar radiation. These allow to split the ionosphere in several regions sometimes confounded with their constitutive layers.

- The *D region* extends between 50 and 90 km where the Ly-α and hard X-rays produce a small ionization. It absorbes extremely low frequencies (ELF) and disappears at night by recombination considering the high neutral density at these altitudes.
- The *E region*, the first to have been studied by Appleton who gave it the name of the electric field, involves O_2^+ and NO^+ as major ions resulting from the effect of soft X-rays. It reaches heights of about 140 km, reflects very low frequencies (VLF) and also almost vanishes at night.
- The *F region*, the densest one, is dominated by EUV radiations and O^+ ions. It is usually divided in the F_1 and F_2 layers. At night, the first goes up into the second which includes the above-mentioned peak at about $300km$. The part above the latter is usually referred to as topside.

- Gradually the H^+ ions become more and more present and give their name to the last region, the *protonosphere*, commonly located above 1000 km.

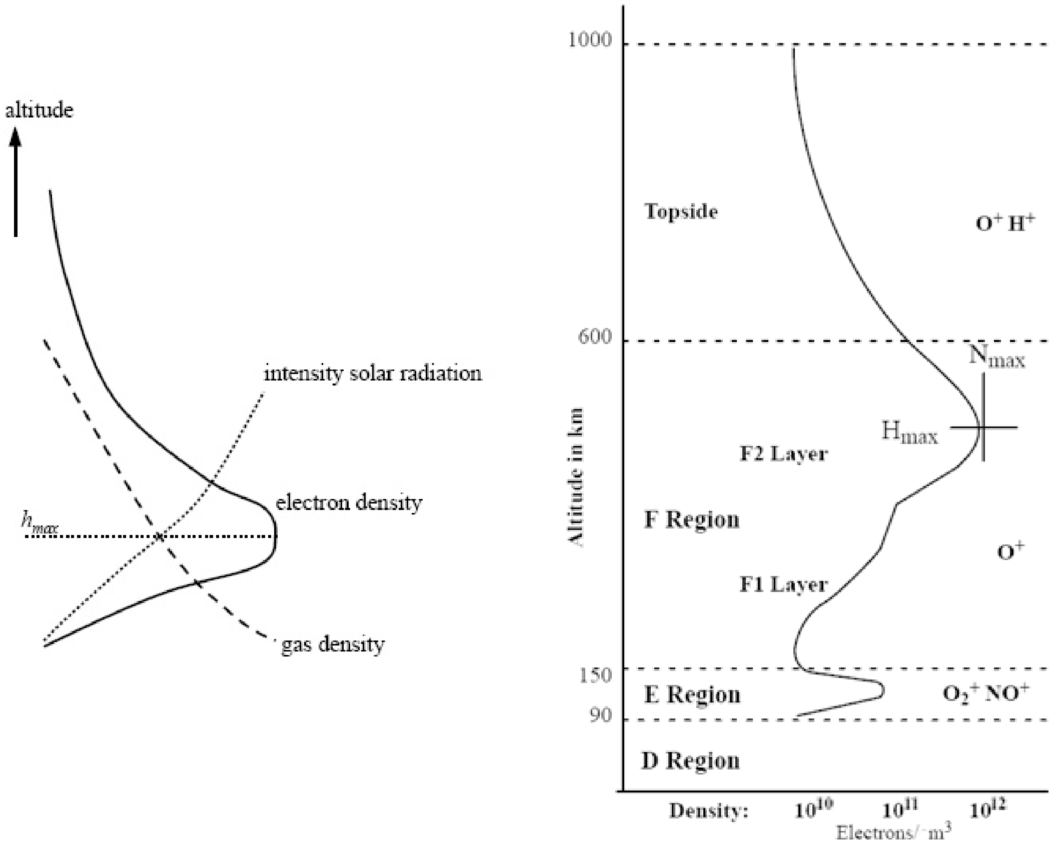

Figure 2.2: Vertical electron density profile resulting from a compromise between different factors (left) [Odijk, 2002] and divided in several layers (right) [Anderson et Fuller-Rowell, 1999]

Table 2.1 gives the orders of magnitude of height and electron densities of the three main ionospheric layers herein considered[1].

Layer	E	F_1	F_2
Height [km]	$90 - 150$	$150 - 200$	$200 - 1000$
Daytime electron density [$el.\ m^{-3}$]	10^{11}	$5\ 10^{11}$	10^{12}
Nighttime electron density [$el.\ m^{-3}$]	$5\ 10^{9}$	–	10^{11}

Table 2.1: Horizontal layers in the ionosphere [Odijk, 2002]

---

[1] These are mainly the layers taken into account within the NeQuick model (cf. subsection 2.3.1) which uses a single function for the topside merging the top F_2 layer and the protonosphere.

In a second approach, the Earth environment constrains the ionosphere horizontally i.e. depending on geographic coordinates latitude and longitude. Apart from the varying angle of incidence of the sun rays also linked to the season, the electron concentration distribution is **influenced by geomagnetism** as every plasma (ionized gas) in an electromagnetic field. The ionosphere dynamics is then conditioned by the Earth magnetic field shape causing for example the electrons to travel on a helicoidal trajectory around the strength lines.

To describe this dependence, geomagnetic variables e.g. latitude must be used but the appropriate parameter for modelling purposes was defined following equation 2.1 [Rawer, 1963] and was called *modified dip latitude* (MODIP) μ [°].

$$\tan\mu = \frac{I}{\sqrt{\cos\phi}} \tag{2.1}$$

I [°] denotes the geomagnetic dip.

ϕ [°] denotes the geographic latitude.

It was first derived by Rawer to build a continuous, physically consistent description of MUF (cf. subsection 2.2.1). It was indeed necessary to consider a physical system of interpolation between the spots of data given by the inhomogeneous station's network. Features such as the equatorial anomaly were then correctly represented even over oceans thanks to the similarity to the shape of the magnetic field (cf. figure 2.3).

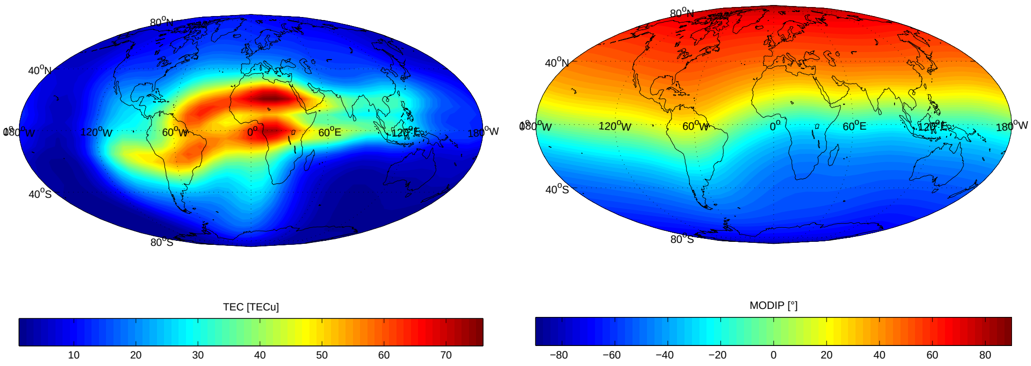

Figure 2.3: Worldwide maps of TEC showing the equatorial anomaly (left) and of MODIP (right)

Following this parameter, the world is divided into *three wide areas* characterized by quite different behaviours (cf. figure 2.4).

- The equatorial region exhibits high average and maximum TEC (resp. 100 and 220 $TECu$)[2] as well as strong gradients (up to 10 $TECu/100$ km).
- The polar region shows really smaller values but is highly variable and disturbed.
- The mid-latitudes, more stable with average and maximum TEC of 20 and 100 $TECu$, define the boundaries of this study.

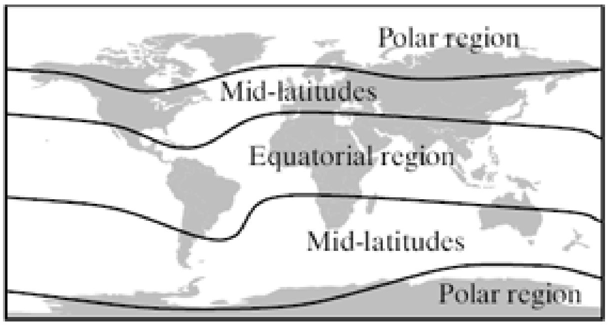

Figure 2.4: Ionospheric regions of the world [Kunches, 1995]

2.1.3 Temporal structure

The temporal behaviour appears as a modulation of the ionosphere ionization i.e. the variation of the sun influence following different **cycles**.

1. A *time-of-day* cycle relates to the solar radiation presence or absence resulting in higher or lower electron densities (cf. table 2.1).
2. A *seasonal* cycle involves the sun height above the horizon and the length of interaction path through the atmosphere.
3. An 11-year *solar* cycle follows the variation of the radiated energy for wavelengths below 200 nm.

---

[2] $1\ TECu = 10^{16}\ el.m^{-2}$ (cf. subsection 2.2.3)

The latter is usually described through two indices strongly related to each other.

1. The *relative sunspot number* R, called the number of Wolf from the Swiss astronomer who introduced it in 1848, is based on the counting of clusters of sunspots (number g) and individual ones (number s).

$$R = k\ (10g + s) \tag{2.2}$$

   The factor k (usually lower than 1) depends on the observatory and is intended to execute the conversion to the original scale. Figure 2.5 shows its evolution and highlights its main advantage of having been computed for more than 150 years. All this data is available from the Solar Influences Data analysis Center (SIDC) in Brussels [SIDC].

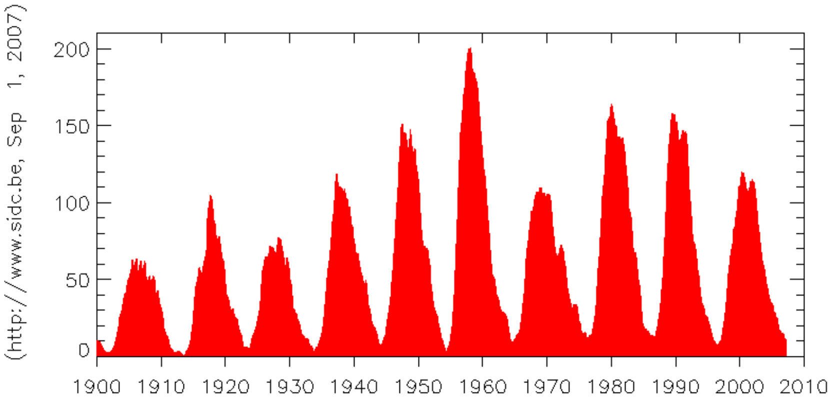

Figure 2.5: General behaviour of the sunspot number [SIDC]

2. The *solar radio noise flux* at 10.7 cm wavelength $F10.7$ (corresponding to a frequency of 2800 MHz) is measured in $10^{-22}\ W\ m^{-2}\ Hz^{-1}$ and originates in the sun chromosphere. It has been recorded in Ottawa from 1947 and is available from the US National Geophysical Data Center (NGDC) in Boulder [NGDC].

For ionospheric modelling, the long-term trend is usually described by means of the *monthly smoothed sunspot number* R_{12} (cf. figure 2.6). For the month n, it is defined as follows [ITU-R, 1999].

$$R_{12}[n] = \frac{1}{12}\left[\frac{R_{n-6}}{2} + \sum_{k=n-5}^{n+5} R_k + \frac{R_{n+6}}{2}\right] \tag{2.3}$$

R_k denotes the mean of the daily sunspot numbers for a single month k.

It thus consists in a 12-month running average with characteristic values of 0 for low, 50 for average and 100 for high solar activity levels.

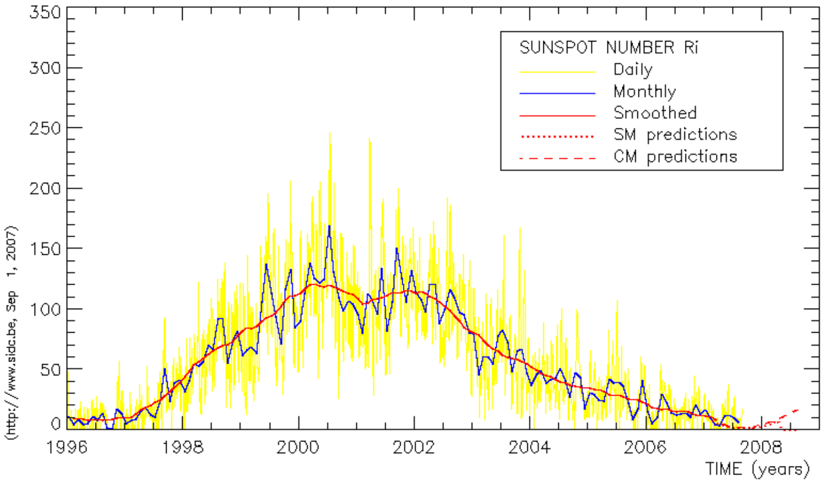

Figure 2.6: Comparison between sunspot numbers [SIDC]

We illustrate further these variations examining the **TEC behaviour** ([Warnant et Pottiaux, 2000, Warnant, 1996, Davies, 1990, Chap. 8] and cf. illustrations in chapter 3) and in particular GPS TEC data (cf. subsection 2.4.2 for details about computing these measurements).

- First of all the inspection of *daily profiles* highlights diurnal values sometimes more than ten times higher then during the night (cf. figures 2.7 and 2.8). Generally a maximum occurs around local noon, at the end of a period of increasing ionization, and a minimum takes place just before sunrise when the sun action reappears.
- The figures show above all the seasonal cycle in the shape of a *monthly median behaviour* with maxima around equinoxes in high solar activity level moving towards summer solstice in the opposite case. However, if the daily profile preserves its shape within a month, its amplitude can greatly vary from day to day e.g. for March 2002 where the local noon TEC ranges from 20 to 70 $TECu$.
- Finally the TEC follows the 11-year *solar cycle* and will then increase in the next years from its current low values towards a maximum around 2011.

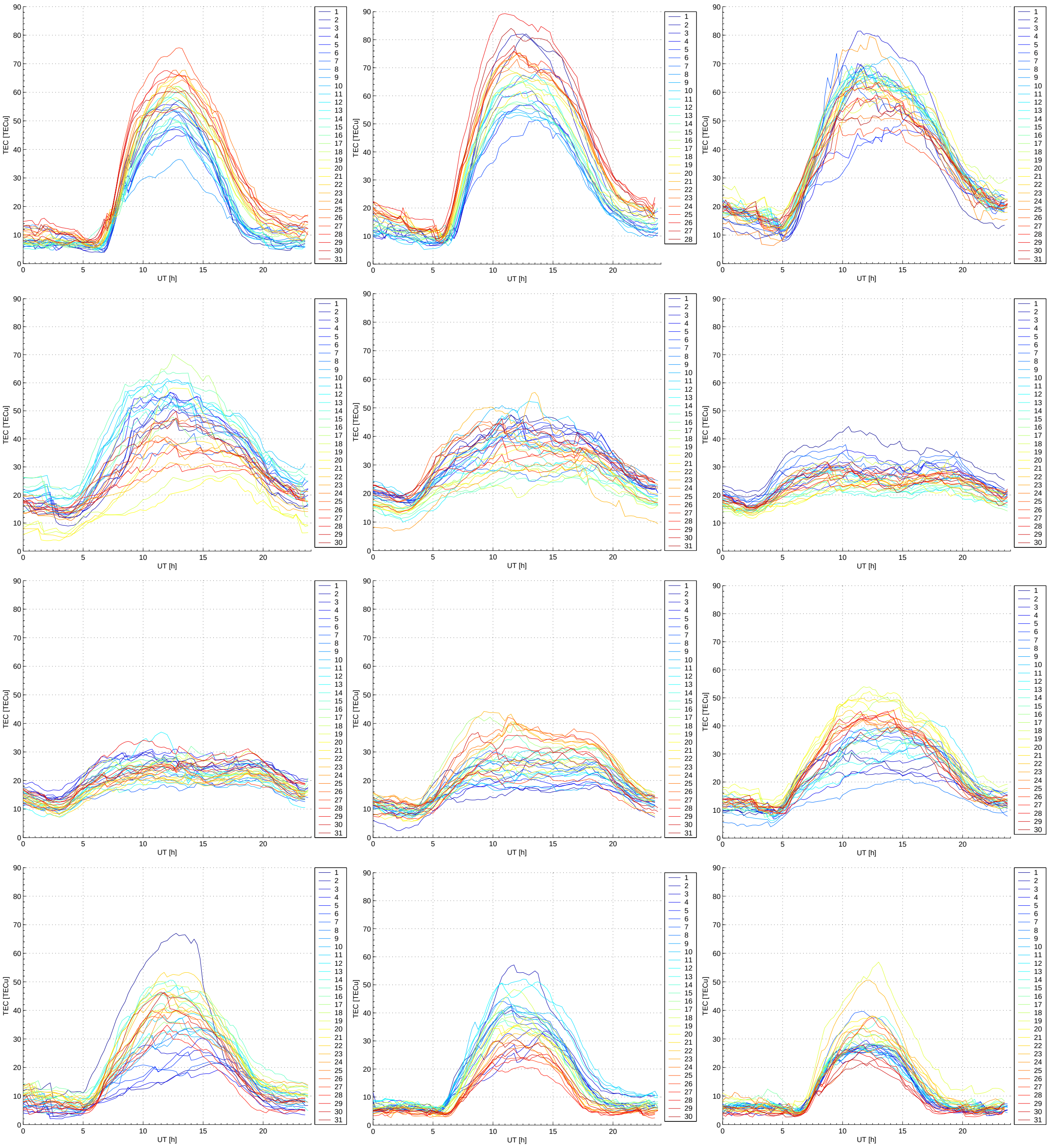

Figure 2.7: Daily GPS TEC profiles over Dourbes for each month of the year 2002

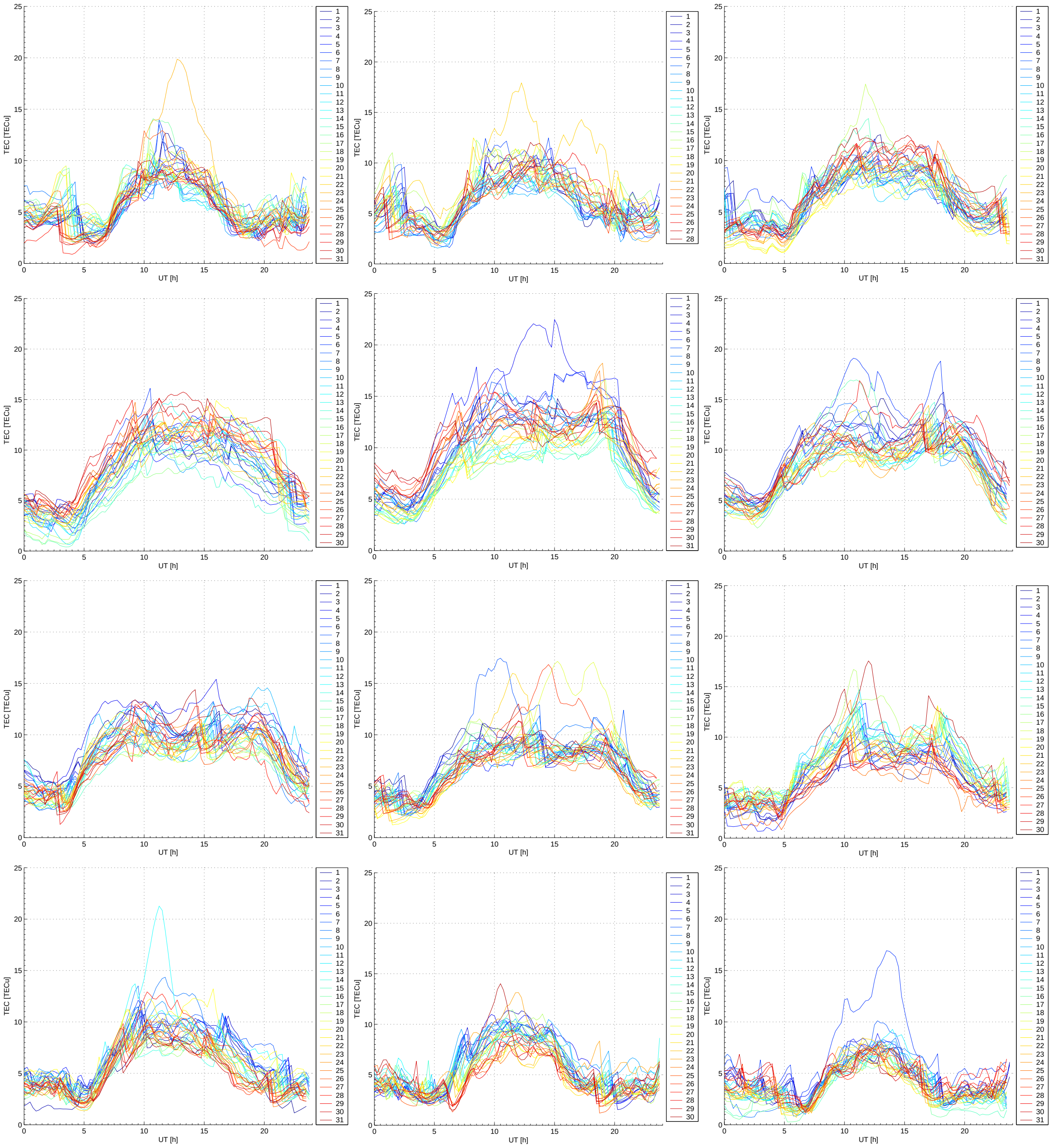

Figure 2.8: Daily GPS TEC profiles over Dourbes for each month of the year 2006

2.1.4 Disturbances and irregularities

A last hot topic to approach in our description of the ionosphere relates to particular phenomena. A first group of **local irregularities** include Travelling Ionospheric Disturbances (TIDs), kinds of waves propagating through the electron density, and scintillations, turbulent features causing amplitude and phase variations in signals crossing the ionosphere. The TIDs affect above all precise positioning applications and the scintillations, resulting in cycle slips and losses of lock, appear mainly in polar and equatorial regions.

On the other hand **global disturbed conditions** can follow some solar events such as solar flares or Coronal Mass Ejections (CMEs). These explosions in the sun atmosphere or ejection of material from the solar corona into the solar wind can interact with the Earth magnetosphere and cause so-called geomagnetic storms [Stankov, 2002]. These disturbances can provoke increase or decrease in the ionospheric electron density and TEC so that their monitoring reveals important.

To this extent, two complementary groups of indices of geomagnetic activity are most widely used (cf. figure 2.9).

1. The *K-index* is a quasi-logarithmic local index of the 3-hourly range in magnetic activity. Its measurements from 13 mid-latitudes observatories around the world are combined to produce the planetary *Kp* index ("planetarische Kennziffer") which estimates the global energy input in the magnetosphere. Its values range from 0 (very quiet) to 9 (very disturbed) by step of a third (5 usually denotes a storm) and are available from the GeoForschungsZentrum in Potsdam [GFZ Potsdam].

2. The *Disturbance Storm-Time (Dst) index* is a more quantitative index as it measures the variation of the ring-current by means of observations near the equator. Its hourly values (in nT) are most of the time negative, become slightly positive at the beginning of a storm and drop in the second phase before returning progressively to their normal state. They can be obtained from World Data Center 2 in Kyoto [WDC Geomagnetism].

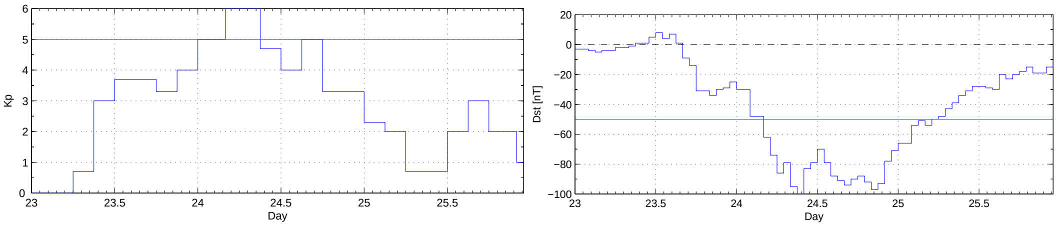

Figure 2.9: *Kp* (left) and *Dst* (right) indices during a geomagnetic storm (March 23rd to 25th, 2002)

2.2 Influence

2.2.1 Radiowaves

To describe radiowave propagation through the ionosphere, some useful quantities are generally defined, including **critical frequencies and transmission factors**. We present here after some conceptual considerations to understand their meaning.

As ionosphere is a dispersive medium, the behaviour of a ray refracting in an ionospheric layer[3] L depends on its frequency f and its initial elevation angle $\frac{\pi}{2} - a_T$ (cf. figure 2.10). It can

- be reflected and come back to the Earth at a certain distance from its emission place known as "sender" (low frequencies ; low elevation angles)
- or cross the ionosphere (high frequencies ; high elevation angles).

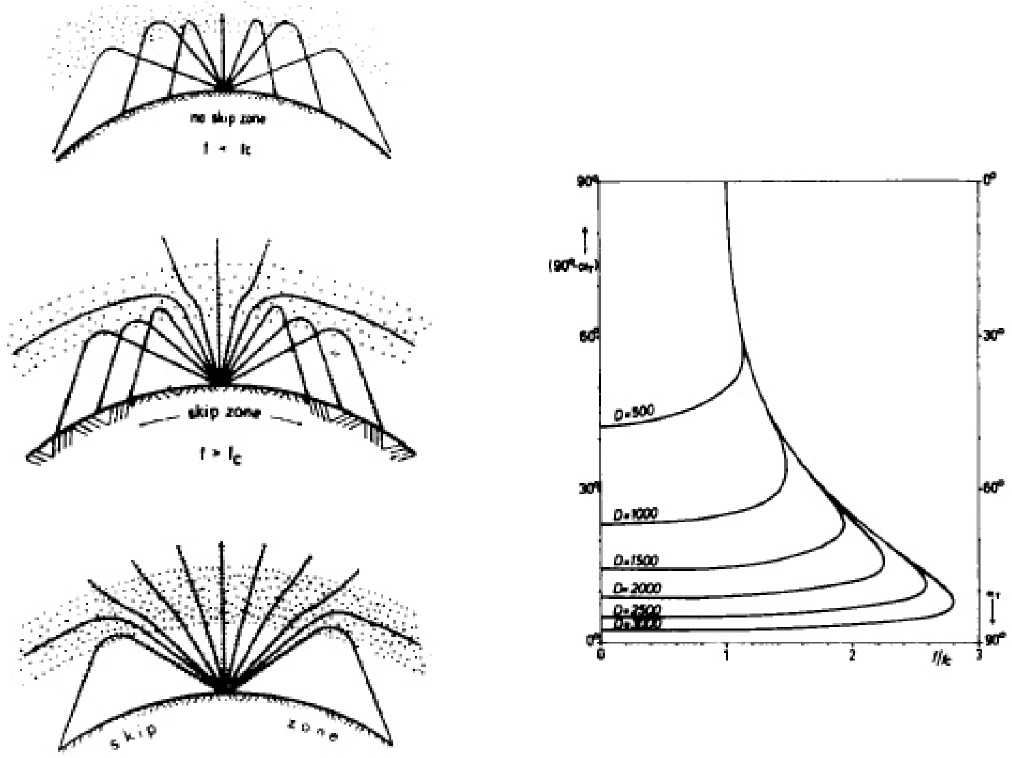

Figure 2.10: Ray geometry (sender on Earth) for different frequencies (left) and elevation angle $\frac{\pi}{2} - a_T$ as a function of f/f_o and with distance as parameter (right) [Rawer, 1963]

---

[3] This general discussion can be applied to the layers of our interest. L stands then for the layer index which possible values are E, F_1 and F_2.

Below a certain frequency (first situation in the left part of figure 2.10), called the *critical frequency* f_oL $[MHz]$, the ray cannot cross the ionosphere for any elevation angle. The layer is somehow dense enough to reflect the ray in all situations – for vertical incidence in particular – so that the critical frequency is linked to the maximum electron density NmL $[10^{12}\ el.\ m^{-3}]$[4] of the layer [Davies, 1990, Chap. 4].

$$N_mL = 1.24\ 10^{-2}\ f_oL^2 \tag{2.4}$$

Above that frequency (other situations in the left part of figure 2.10), a zone around the sender, called "skip zone", exists which cannot be reached by reflection. In other words, at a fixed frequency greater than the critical frequency corresponds a minimum distance of reception. If the latter is now fixed, the corresponding maximum frequency is defined as the maximal usable frequency MUF (cf. right part of figure 2.10).

Considering the F_2 layer, the standard $MUF(3000)F_2$ is obtained for a distance of 3000 km. The *transmission factor* $M(3000)F_2$ comes then from the division of $MUF(3000)F_2$ by f_0F_2 and is linked to the height h_mF_2 where the electron density reaches its maximum value, called the layer peak[5].

$$h_mF_2 = \frac{1490}{MUF(3000)F_2} - 176 \tag{2.5}$$

This factor and the critical frequencies are often involved in models as empirical equations were derived for them on the basis of measured data (cf. subsection 2.4.1) so that they are known as *ionosonde parameters*. These formulas allow usually to compute monthly medians for a set of space and time conditions. For the F_2 characteristics (f_0F_2 and $M(3000)F_2$), they consist in a Fourier time series (cf. equation A.21) reflecting the more complicated dynamics of the F_2 layer. Called numerical maps, the most common ones were released by the Consultative Committee for International Radio in 1967 and are often referred to as *"CCIR maps"*.

The critical frequency can in fact be determined for any electron density constituting an intrinsic characteristic of a plasma. It is therefore also labeled plasma frequency f_p and is involved in another major parameter regarding radio propagation, the **refractive index** n. For a dispersive medium such as the ionosphere, two indices are actually defined.

---

[4] These units are preferred regarding the characteristic orders of magnitude of electron densities in table 2.1.

[5] This equation [Shimazaki, 1955] reveals the influence of $MUF(3000)F_2$ on h_mF_2 but is only an approximation of the more complex formula A.8 generally used.

- The *phase* refractive index n_p is equal to the ratio between the speed of light $c \simeq 3\ 10^8\ ms^{-1}$ and the one of a monochromatic wave propagating through the medium.

$$n_p = \frac{c}{v_p} \tag{2.6}$$

- The second, the *group* refractive index n_g, exhibits a similar formula for a wave packet and is bound to the first through the relation 2.8 where f denotes the signal frequency.

$$n_g = \frac{c}{v_g} \tag{2.7}$$

$$n_g = n_p + f\frac{dn_p}{df} \tag{2.8}$$

Solving Maxwell's equations for a collisional plasma in a uniform magnetic field leads to the complete formula for the phase refractive index known as the Appleton formula[6]. However some *approximations* will be sufficient in our case as we consider navigation frequencies of about 1 GHz (cf. next subsection) for which collisions and geomagnetic field influences can be neglected.

The equation simplifies already drastically for frequencies above 100 MHz (cf. equation 2.9) and reinforces our interpretation of the beginning of this subsection as $f = f_p$ at signal reflection ($n = 0$).

$$n_p^2 = 1 - \left(\frac{f_p}{f}\right)^2 \tag{2.9}$$

For even higher frequencies, a Taylor series development becomes valid and the substitution of f_p $[MHz]$ following a similar equation to 2.4 closes the loop introducing the electron density Ne $[10^{12}\ el.\ m^{-3}]$. The group index differs only by the sign of the second term resulting in a delay for wave packets as they will travel slower than in free space as opposed to monochromatic waves.

$$\begin{aligned} n_p &= 1 - \frac{1}{2}\left(\frac{f_p}{f}\right)^2 \\ &= 1 - 40.3\,\frac{N_e}{f^2} \qquad (2.10) \\ n_g &= 1 + 40.3\,\frac{N_e}{f^2} \qquad (2.11) \end{aligned}$$

---

[6] The interested reader will find the whole development in [Davies, 1990, Chap. 3].

2.2.2 GNSS

As they use electromagnetic signals propagating between Earth and space, **Global Navigation Satellite Systems** (GNSS) are affected by ionospheric effects. This general term (GNSS) refers to sets of ground and space-based equipments providing autonomous positioning anywhere in the world. The United States NAVSTAR[7] Global Positioning System (GPS) is currently the only one fully operational but it is due to be joined by several others. Indeed the Russian GLObal NAvigation Satellite System (GLONASS) is on the way to being restored and the European GALILEO System is in its development phase. China has also indicated its intention to extend the regional BeiDou[8] system and India decided about one year ago to develop its own Indian Regional Navigational Satellite System (IRNSS).

We are most interested in GPS and GALILEO which will own several common features (cf. table 2.2). They will both provide several services with varying broadcast information, accuracies and devoted to different users[9] and they are generally divided in three **segments** (cf. figure 2.11 for GPS).

1. The *Space* segment includes the Medium-Earth Orbit (MEO) constellation of several tens of satellites designed to ensure a sufficient number of visible satellites anywhere on Earth any time. They broadcast the navigation signals through several frequency bands, currently two for GPS where as GALILEO should count three of them.

	GPS	GALILEO
Basic obedience	Military	Civilian
Number of services	2	5
Number of carrier frequencies	2	3
Horizontal accuracy for civilian users $[m]$	20	15
Integrity	no	yes
Search and Rescue services	no	yes
Number of satellites (operational/in orbit)	24/29	27/30
Average altitude $[km]$	20200	23222
Number of orbital planes	6	3
Inclination $[^\circ]$	55	56
Period [hours]	12	14
Ground stations	6	45
Antennas	3	9
Control stations	1	2

Table 2.2: Comparison between current GPS and future GALILEO systems

---

[7] NAVigation Satellite Timing And Ranging

[8] Chinese name for Ursa Major constellation

[9] The interested reader will find further details in [USACE, 2003] and [EU].

2. The *Control* or *Ground* segment consists firstly of ground stations, monitoring the state of the satellites and collecting several kinds of observations. They transmit this information to control stations which analyse them and update the navigation message. The latter is finally uploaded into the satellites memory through antennas.

3. The *User* segment comprises the receivers that have been designed to decode the signals from the satellites for the purposes of determining position, velocity and time.

Furthermore they will be *interoperable* allowing users to combine signals from both systems to compute their position. Some signals will indeed be broadcast in overlapping frequency bands (e.g. L_1 for GPS and $E_2 - L_1 - E_1$ for GALILEO). GALILEO will all the same exhibit several advantages on GPS among which enhanced availability and accuracy as well as the provision of reliability information through an *integrity* message. Nevertheless GPS is on its way to a *modernization* adding for instance several signals and a third frequency band (L_5).

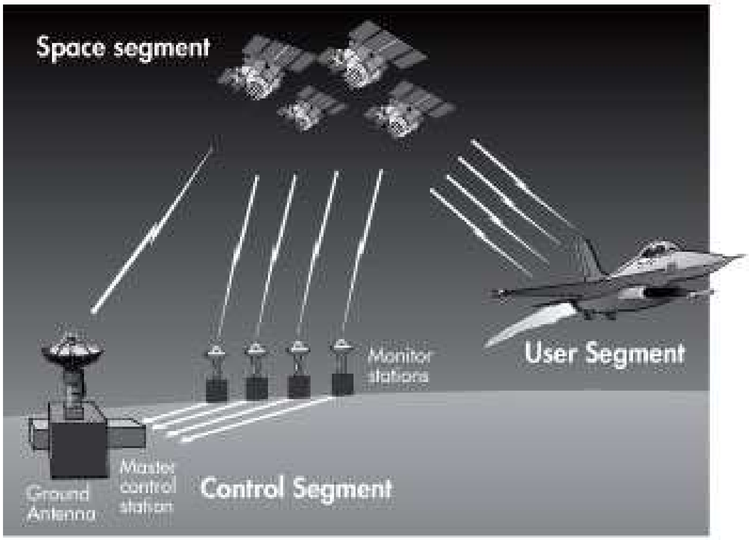

Figure 2.11: GPS segments [The Aerospace Corporation]

Getting closer to GPS **signals** structure, we observe the combination of different elements (cf. equations 2.12 and 2.13 and table 2.3) all based on the most important characteristic of GPS, its own time scale. The latter is defined by ultra stable atomic clocks on board the satellites, generating a fundamental frequency f_0 of 10.23 MHz.

1. The *carrier waves* L_1 and L_2 own frequencies equal to exact multiples of the fundamental frequency. (φ denotes a phase shift.)
2. They are modulated by so-called Pseudo Random Noise (PRN) *codes*, the Coarse-Acquisition code C/A on L_1 and the Precision code P on both, in quadrature with C/A. The first repeats itself identically every millisecond whereas the second has a period of 38 weeks. Both are binary and allow to identify uniquely each satellite. (A_P denotes the P code amplitude.)
3. Before the modulation, the *navigation message* D is added modulo 2 to the codes. It contains information about the satellites health, orbits, clock correction, etc.

$$\begin{aligned} L_1(t) &= A_P\,[P(t) \oplus D(t)]\cos(2\pi f_1 t + \varphi) \\ &\quad + \sqrt{2}A_P\,[C/A(t) \oplus D(t)]\sin(2\pi f_1 t + \varphi) \qquad (2.12) \\ L_2(t) &= A_P\,[P(t) \oplus D(t)]\cos(2\pi f_2 t + \varphi) \qquad (2.13) \end{aligned}$$

	Frequency
f_0	$10.23\ MHz$
L_1	$f_1 = 154 f_0 = 1575.42\ MHz$
L_2	$f_2 = 120 f_0 = 1227.60\ MHz$
C/A	$f_{C/A} = f_0/10 = 1.023\ MHz$
P	$f_P = f_0 = 10.23\ MHz$
D	$50\ bit/s$

Table 2.3: GPS signals elements and associated frequencies

The receiver processes these signals to provide the user with a number of information among which its position. To this extent, it uses a trilateration method locating somehow the receiver at the intersection of three spheres centered about three satellites. More precisely **positioning** is based on the determination of the distance D_p^i between the receiver p of unknown position (X_p, Y_p, Z_p) and the satellite i with known coordinates (X^i, Y^i, Z^i). The latest are indeed computed thanks to the ephemeris from the navigation message for example. This technique is called Time Of Arrival (TOA) ranging as it employs the propagation time between emission at t_e and reception at t.

$$\begin{aligned} D_p^i &= c(t - t_e) \qquad (2.14) \\ &= \sqrt{(X^i - X_p)^2 + (Y^i - Y_p)^2 + (Z^i - Z_p)^2} \qquad (2.15) \end{aligned}$$

This distance appears in the expression of measurements performed on codes and carriers known as observables. On the one hand the code observable called *pseudo-distance* does not exactly correspond to the geometric distance between satellite and receiver. The latest exhibit indeed time scales more or less different from the GPS reference so that clock errors have to be added, $\Delta t_p(t)$ for the receiver at time of reception and $\Delta t^i(t_e)$ for the satellite at time of emission.

$$\begin{aligned} P_p^i &= c(t_p(t) - t^i(t_e)) \\ &= D_p^i + c\left(\Delta t^i(t_e) - \Delta t_p(t)\right) \end{aligned} \tag{2.16}$$

As for the satellite position, the clock correction is calculated from the information in the navigation message leaving four unknowns namely the receiver position (X_p, Y_p, Z_p) and clock error Δt_p. At least four equations and associated satellite signals are thus necessary to find an absolute positioning solution. Even more satellites can often be observed simultaneously and a least squares adjustment furnishes then the receiver position with a certain precision[10]. The latter depends among others on the systems geometry (cf. figure 2.12) through the resulting cofactor matrix from which characteristic parameters are derived. They are referred to as Dilution Of Precision (DOP) and are used in the determination of horizontal (HDOP) or vertical (VDOP) coordinates, position (PDOP) or time (TDOP), or all unknowns (geometric DOP, GDOP). The lower the DOP the better the precision, with values generally below 10.

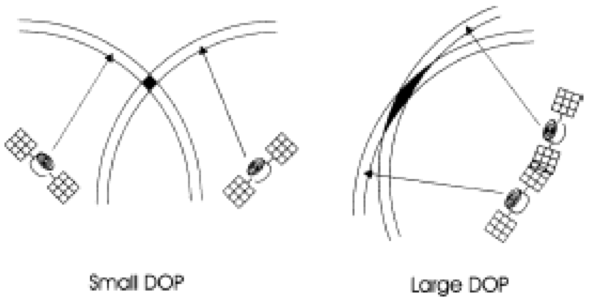

Figure 2.12: Dilution of precision [Kintner et Ledvina, 2005]

On the other hand, the *phase observable* corresponds to beat phase measurements on the carriers and is more involved in relative positioning techniques. It is defined as follows with an additional unknown in the shape of an integer number of wavelength N_p^i called ambiguity.

---

[10] See [Warnant, 2006] for complete development.

$$
\begin{aligned}
\varphi_p^i &= \varphi_p\left(t_p(t)\right) - \varphi^i\left(t^i(t_e)\right) + N_p^i \\
&= f\frac{D_p^i}{c} + f\left(\Delta t^i(t_e) - \Delta t_p(t)\right) + N_p^i
\end{aligned}
\tag{2.17}
$$

Finally a wide range of **phenomena**, among which ionospheric effects, **affect** the carriers and codes **propagation times** so that several terms have to be added into the equations to represent them. To derive the most general expressions here under, it is also necessary to differentiate between the carriers (index $k = 1, 2$) and, for those terms which appear in both equations, the code (index m for modulation) and the phase (index φ) observables. To express it in terms of distances, the phase observable is multiplied by the wavelength λ_k.

$$
\begin{aligned}
P_{p,k}^i = D_p^i + c\left(\Delta t^i(t_e) - \Delta t_p(t)\right) \\
+ T_p^i + I_{p,k}^i + M_{p,k,m}^i - G_k^i + G_{p,k} + \varepsilon_{p,k,m}^i
\end{aligned}
\tag{2.18}
$$

$$
\begin{aligned}
\Phi_{p,k}^i = D_p^i + c\left(\Delta t^i(t_e) - \Delta t_p(t)\right) + \lambda_k N_{p,k}^i \\
+ T_p^i - I_{p,k}^i + M_{p,k,\varphi}^i - p_k^i + p_{p,k} + \varepsilon_{p,k,\varphi}^i
\end{aligned}
\tag{2.19}
$$

T_p^i denotes the tropospheric or neutrospheric effect.

$I_{p,k}^i$ denotes the ionospheric effect depending on frequency (cf. subsection 2.2.3).

$M_{p,k,m}^i$ and $M_{p,k,\varphi}^i$ denote modulations and phases multipath effects.

G_k^i, $G_{p,k}$, p_k^i and $p_{p,k}$ denote the biases associated to delays produced by the receiver and the satellite hardware.

$\varepsilon_{p,k,m}^i$ and $\varepsilon_{p,k,\varphi}^i$ denote measurement noises.

Coming back to the case of absolute positioning using codes, we can now complete our definition of the **positioning accuracy**. Some of the above-mentioned effects are indeed modelled but never perfectly so that residual errors combine with the other terms to produce the so-called User Equivalent Range Error (UERE). Its components (cf. figure 2.13) are usually classified as in table 2.4 which gives orders of magnitude and includes also the error on satellite orbit (ephemeris). The UERE propagates then through the system of equations defining with the DOP the positioning accuracy.

$$
\epsilon = DOP * UERE \tag{2.20}
$$

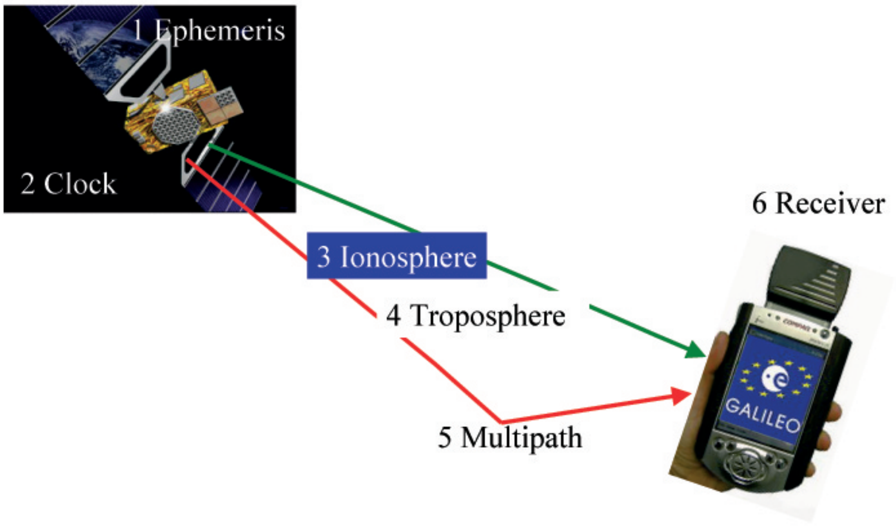

Figure 2.13: Different elements contributing to the positioning error

1. Ephemeris	$1-2\ m$
2. Clock	$1-2\ m$
3. Ionosphere	$1\ cm-50\ m$
4. Troposphere	dm
5. Multipath	$1-2\ m$
6. Receiver	$0.3-2\ m$

Table 2.4: Orders of magnitude of the components of the User Equivalent Range Error [Warnant, 2006]

2.2.3 Ionospheric error

To represent the ionospheric effects on the positioning accuracy, we consider the ionospheric propagation delay τ or the **ionospheric range error** I in terms of distance. They measure respectively the time delay and the length difference between the real case of signals propagating through the ionosphere at speed v and the hypothetic situation where they would reach the receiver following a straight path in free space.

$$\tau = \int_{sat.}^{rec.} \frac{ds'}{v} - \int_{sat.}^{rec.} \frac{ds}{c} = \frac{1}{c}\left(\int_{sat.}^{rec.} n ds' - \int_{sat.}^{rec.} ds\right) \tag{2.21}$$

$$I = \int_{sat.}^{rec.} n\ ds' - \int_{sat.}^{rec.} ds \tag{2.22}$$

Beside the changes in the signals speed, the refraction implies actually modifications in their direction of propagation. The latest are however negligible for satellites above 10° elevation [Warnant, 2006] so that we can merge the integrals and substitute the refractive index by its phase and group expressions (cf. equations 2.10 and 2.11) obtaining opposed *phase and group* range errors.

$$I_g = \int_{sat.}^{rec.} (n_g - 1)\ ds = \frac{40.3}{f^2} \int_{sat.}^{rec.} N_e\ ds \tag{2.23}$$

$$I_p = \int_{sat.}^{rec.} (n_p - 1)\ ds = -\frac{40.3}{f^2} \int_{sat.}^{rec.} N_e\ ds = -I_g \tag{2.24}$$

The carriers range will thus appear shorter whereas the modulations will travel longer due to the ionosphere. Thanks to the latest equations, we can also improve our interpretation of TEC which we recognize behind the integral. Here it is defined as the amount of free electrons in a cylinder of unit cross-section aligned with the line-of-sight and as long as the path between the satellite and the receiver. Its units are $[el.\ m^{-2}]$ or more generally TEC units $[TECu = 10^{16}\ el.m^{-2}]$, one $TECu$ inducing an error of 0.16 m for the L_1 carrier (1575.42 MHz).

$$I_g = -I_p = \frac{40.3}{f^2} sTEC \tag{2.25}$$

$$sTEC = \int_{sat.}^{rec.} N_e\ ds \tag{2.26}$$

This oblique or slant TEC ($sTEC$) generalizes thus our previous definition (cf. subsection 2.1.1) which corresponds to the particular case of vertical propagation and could therefore be referred to as vertical TEC ($vTEC$). To study its behaviour or to take its effect into account, it is often necessary to *convert it to equivalent vertical* TEC as it depends on satellite elevation. To this extent, a common procedure consists in modelling the ionosphere as a spherical shell of infinitesimal thickness, concentrating all the free electrons at a height h_i of about 350 km (cf. figure 2.14). The satellite line-of-sight pierces this layer at a point called ionospheric point (IP) associated to the whole electron content allowing to derive a simple relation between $sTEC$ and $vTEC$ in function of the satellite zenith angle χ_{IP}. The latter is different from its value observed by the receiver χ and is then calculated thanks to the sine law and the Earth radius R_E. The resulting second factor in the following equation is known as "mapping function".

$$sTEC = \frac{vTEC}{\cos \chi_{IP}} = vTEC \left(\sqrt{1 - \left(\frac{R_E \sin \chi}{R_E + h_i} \right)^2} \right)^{-1} \tag{2.27}$$

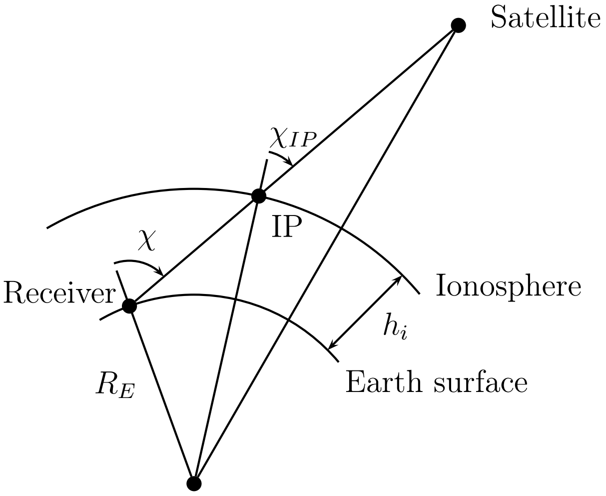

Figure 2.14: The thin shell approximation and the ionospheric point definition

The final goal consists of course in **suppressing the ionospheric effects** as far as possible to increase the positioning accuracy.

1. Consequently two frequencies were originally implemented to take advantage of the dispersive property of the ionosphere. They allow *multiple frequency* receivers to compute so-called ionospheric free combinations defined for code observables (cf. equation 2.18) by the following equation.

$$P^i_{p,IF} = \frac{f_1^2 P^i_{p,1} - f_2^2 P^i_{p,2}}{f_1^2 - f_2^2} \tag{2.28}$$

   In that expression, ionospheric effects (cf. equation 2.25) interact destructively as follows.

$$\frac{f_1^2 I^i_{p,1} - f_2^2 I^i_{p,2}}{f_1^2 - f_2^2} = \frac{1}{f_1^2 - f_2^2}\left(f_1^2 \frac{40.3}{f_1^2} sTEC^i_p - f_2^2 \frac{40.3}{f_2^2} sTEC^i_p\right) = 0$$

2. For *single frequency* users on the other hand, TEC has to be predicted to derive and subtract the ionospheric error. Several methods exist for this purpose and employ various modelling tools approached in the next section.

2.3 Modelling

2.3.1 NeQuick

We distinguish **three main categories** of models dedicated to the description of ionospheric parameters [Cander et al, 1998]. *Theoretical* models, such as the Global Theoretical Ionospheric Model (GTIM), attempt to solve principle equations governing the processes in the ionospheric plasma. *Parametric* models, such as the Parameterized Ionospheric Model (PIM), simplify the first in terms of a small number of parameters. Finally *empirical* models, such as the International Reference Ionosphere (IRI), are based on observations.

The last group includes a set of three models based on the same philosophy, referred to as "DGR family" [Di Giovanni et Radicella, 1990], NeQuick, COSTprof and NeUoGplas. Designed at the Abdus Salam International Centre for Theoretical Physics [ICTP], Italy, and at the University of Graz, Austria, they are known as "*profilers*" as they fit analytical functions on a set of anchor points, namely the E, F_1 and F_2 layer peaks, to compute the electron density profile. **NeQuick**, the simplest one, was adopted by the ITU-R recommendation for TEC modelling. Thanks to its computational speed where its name comes from, it was chosen for the calculation of the ionospheric UERE contribution for GALILEO so that it constitutes the very basis of our concerns.

The NeQuick model is divided into two regions: the *bottomside*, up to the F_2-layer peak, consists of a sum of five semi-Epstein layers[11] and the *topside* is described by means of an only sixth semi-Epstein layer with a height-dependent thickness parameter.

The shape of an *Epstein layer* representing the electron density $N(h)$ [10^{12} $el.\ m^{-3}$] is given by the following function [Rawer, 1982] shown in figure 2.15.

$$N(h) = 4\ N_{max}\ \frac{e^{\frac{h-h_{max}}{B}}}{(1+e^{\frac{h-h_{max}}{B}})^2} \tag{2.29}$$

N_{max} [10^{12} $el.\ m^{-3}$] denotes the peak amplitude.

h_{max} [km] denotes the height of the peak.

B [km] denotes the thickness parameter.

---

[11] The prefix "semi" means that different thickness parameters are used below and above the layer peak.

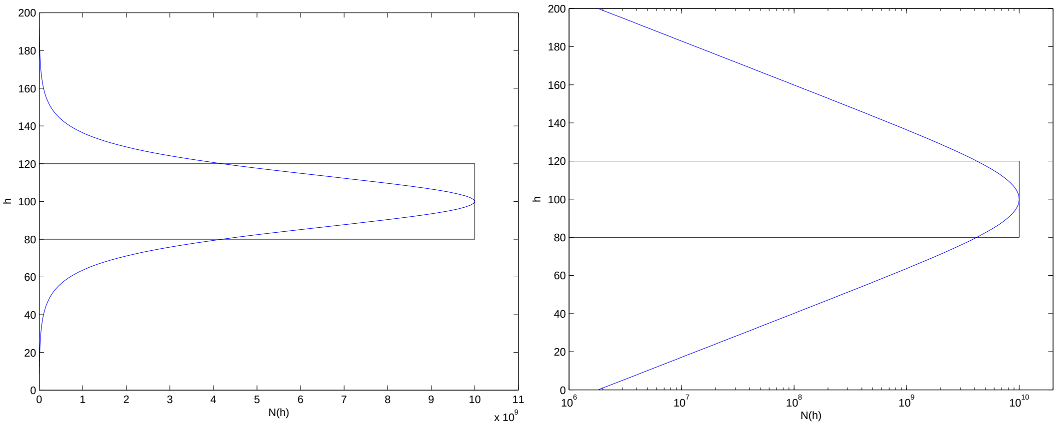

Figure 2.15: The Esptein function with linear (left) and logarithmic (right) scales

We can find an interesting interpretation of B by calculating the surface under the curve as follows, posing $x = e^{\frac{h-h_{max}}{B}}$.

$$\begin{aligned} C &= \int_{-\infty}^{+\infty} 4\ N_{max}\ \frac{e^{\frac{h-h_{max}}{B}}}{(1+e^{\frac{h-h_{max}}{B}})^2} dh \\ &= 4\ N_{max} \int_{0}^{+\infty} \frac{B}{(1+x)^2} dx \\ &= 4\ N_{max}\ B \left[\frac{-1}{1+x}\right]_0^{+\infty} \\ &= 4\ N_{max}\ B \end{aligned} \tag{2.30}$$

$4B$ and N_{max} are then the edges of a rectangle with same surface[12].

To compute the parameters for the Epstein layers, the thickness parameters and the anchor points coordinates i.e. peaks electron density and height, NeQuick employs the *ionosonde parameters* defined in subsection 2.2.1. f_oE, f_oF_1, f_oF_2 and $M(3000)F_2$ are themselves obtained from empirical equations among which the CCIR maps for the F_2 characteristics[13] so that a monthly median situation is represented. However the power of NeQuick consists in its ability to accommodate other sources of data for these parameters e.g. measured values.

Figure 2.16 shows profile examples for current conditions applying the complete model of which the detailed set of equations is reported in appendix A.2.

---

[12] Note the diverting impression with logarithmic scale: the surface below the curve and within one thickness parameter around peak height represents almost half of C.

[13] Note that NeQuick f_oE and f_oF_1 should be referred to as *effective* critical frequencies as their definition does not correspond exactly to the reference ITU-R recommendation [ITU-R, 1997].

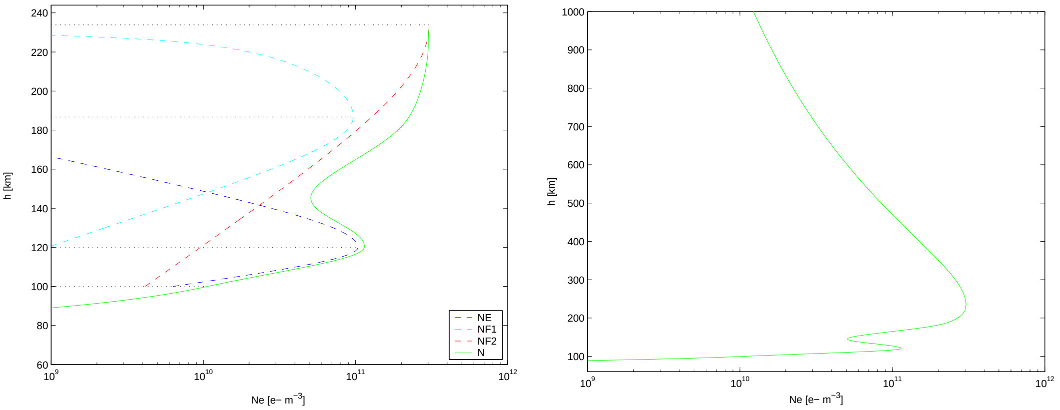

Figure 2.16: Bottomside (left) and complete (right) profiles example from NeQuick version 1 (Dourbes – $50.1^\circ N$, $4.6^\circ E$; August ; low solar activity – $R_{12} = 10$; 12 UT)

NeQuick FORTRAN 77 code was submitted to and accepted by the ITU-R in 2000 and revised in 2002. It is downloadable from the Internet [ITU-R, 2002], is referred to either as *version 1* or ITU-R and constitutes the current baseline for GALILEO. This package, of which a comprehensive description of the implementation can be found in [BIDAINE, 2006], includes also numerical integration subroutines[14] allowing to compute $vTEC$ and $sTEC$.

Since then the model has undergone a series of evolutions leading to a **second version** [BIDAINE et al, 2006] detailed in appendix A.3 and available from the model designers[15].

- *Bottomside simplifications* and associated changes in the calculation of the E and F_1 peak amplitudes and f_oF_1 [LEITINGER et al., 2005] allow to avoid some unrealistic features (cf. figure 2.17).
- Topside soundings data were processed to modify the formulation of the *shape parameter* k involved in the *topside* thickness parameter calculation [COÏSSON et al., 2006].
- Finally a *new MODIP file* was introduced for MODIP interpolation in the framework of CCIR maps use [NAVA, 2007].

Consequently potential improvements need to be assessed in particular for the GALILEO ionospheric correction algorithm for single frequency users described in next subsection.

---

[14] They consist in 2nd order Gauss-Legendre quadratures associated to Richardson extrapolations [WEISSTEIN a, WEISSTEIN b], tools that we adapted for the purpose of this study.

[15] Pr Sandro Radicella, Bruno Nava and Pierdavide Coïsson from ICTP in Trieste [ICTP].

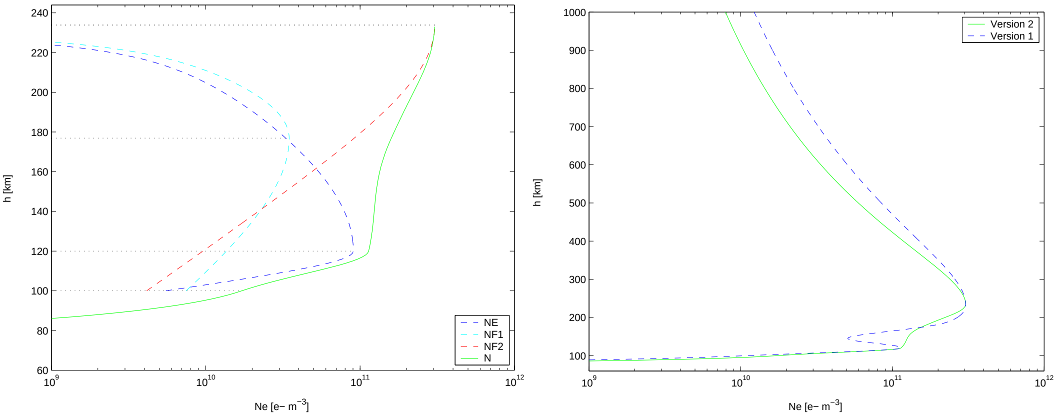

Figure 2.17: Bottomside (left) and complete (right) profiles example from NeQuick version 2 (Dourbes – $50.1^{\circ}N$, $4.6^{\circ}E$; August ; low solar activity – $R_{12} = 10$; 12 UT)

2.3.2 Mitigation

The **mitigation of the ionospheric effects** for GALILEO **single frequency users** will consist in a sensibly different method then for GPS. In the latter, the so-called KLOBUCHAR algorithm, designed in 1987 on the basis of the Bent model [KLOBUCHAR, 1987], uses eight broadcast coefficients from the navigation message to compute vTEC. Assuming a thin shell ionosphere as in subsection 2.2.3, sTEC in then computed and converted to time delay. This technique, illustrated in figure 2.18, is supposed to provided a 50% root mean square (RMS) correction of the ionospheric time delay.

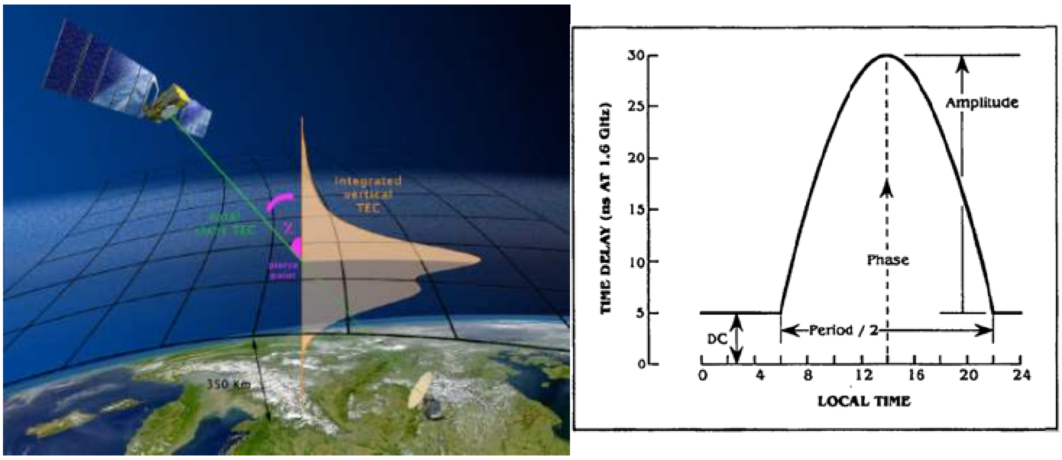

Figure 2.18: KLOBUCHAR algorithm scheme [RADICELLA, 2003] and daily time delay profile example [WARNANT, 2006]

In the case of GALILEO, NeQuick will be used along the ray path to generate electron densities subsequently integrated to obtain sTEC (cf. figure 2.19). According to its specification, this method should exhibit a maximum residual error of 20 $TECu$ or 30% of the actual sTEC, whichever is larger, for satellites above 10° elevation and nominal ionospheric conditions[16] [Arbesser-Rastburg, 2006].

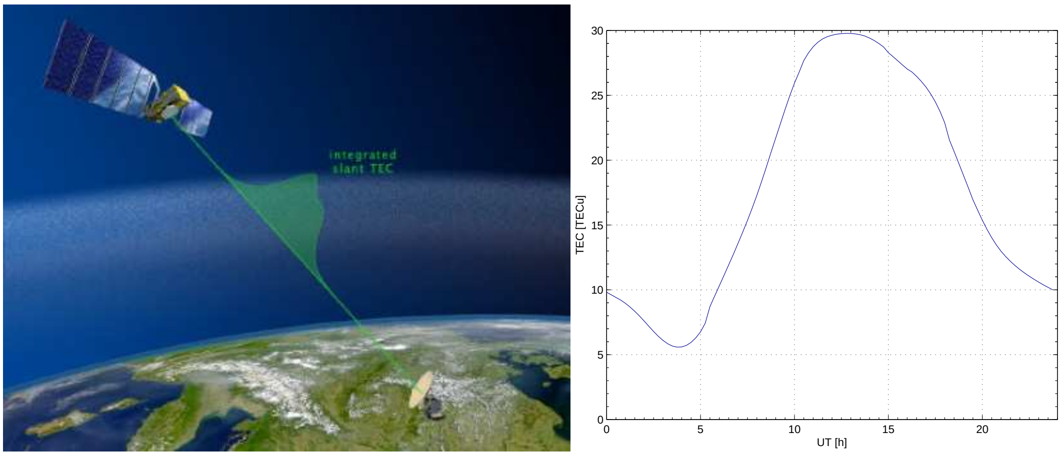

Figure 2.19: NeQuick algorithm scheme [Radicella, 2003] and daily TEC profile example

To reach this goal, NeQuick, providing originally monthly medians, has to be completed by a proper algorithm in order to give daily values. The solution was found [Arbesser-Rastburg et Prieto-Cerdeira, 2005] defining an **effective ionization level** Az for the whole world, applicable for a period of typically 24 hours, depicting solar activity instead of solar flux $F10.7$ (or equivalent sunspot number R_{12}). Its implementation follows NeQuick noticed mis-modelling depending on location with respect to the magnetic field as a second order polynomial of MODIP μ.

$$Az = a_0 + a_1\ \mu + a_2\ \mu^2 \tag{2.31}$$

The three coefficients a_0, a_1 and a_2 will be calculated following an optimization process based on measurements performed at the Ground segment stations (cf. figure 2.20). They will then be broadcast to the user through the navigation message. This algorithm has been evaluated in several ways and has proven in the last study to meet the specification more than 95% of the time [Prieto-Cerdeira et al, 2006].

---

[16] Disturbance flags, computed separately for each MODIP region (cf. figure 2.4), will indeed inform the user about disturbed conditions for which the correction might not be reliable.

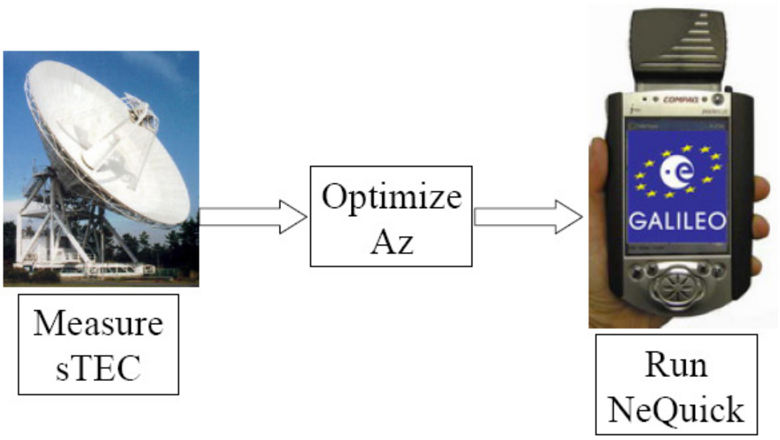

Figure 2.20: GALILEO single-frequency algorithm

2.4 Measuring

2.4.1 Ionosonde

To complete this introduction about the ionosphere, we must present some probing techniques. Indeed models need ionospheric data to be tested against them or even to be constructed on their basis. Major instruments in this field, **ionosondes**, provided the data underlying the CCIR maps or the NeQuick model among others.

Based on the principles of radiowave propagation described in subsection 2.2.1, these devices emit pulsed signals vertically from the ground. They sweep frequencies from about 0.1 to more than 30 MHz mainly reflected by ionospheric layers depending on their electron concentration (cf. equation 2.4). The latter increases with altitude allowing them to probe higher and higher regions until the F_2 peak. Therefore measuring the time of flight t elapsed until reception provide them with information about the height of reflection. They compute so-called *virtual heights* h' taking the half of the apparent distance covered.

$$h' = \frac{c\,t}{2} \tag{2.32}$$

As the waves do not travel at the speed of light, some processing is needed to convert virtual height in actual altitude which is know as *true height inversion*. A graph of virtual height against frequency is called an *ionogram* (cf. figure 2.21). On these plots, *characteristic points* are routinely *scaled* i.e. several parameters among which the ionosonde parameters defined in subsection 2.2.1 are systematically identified.

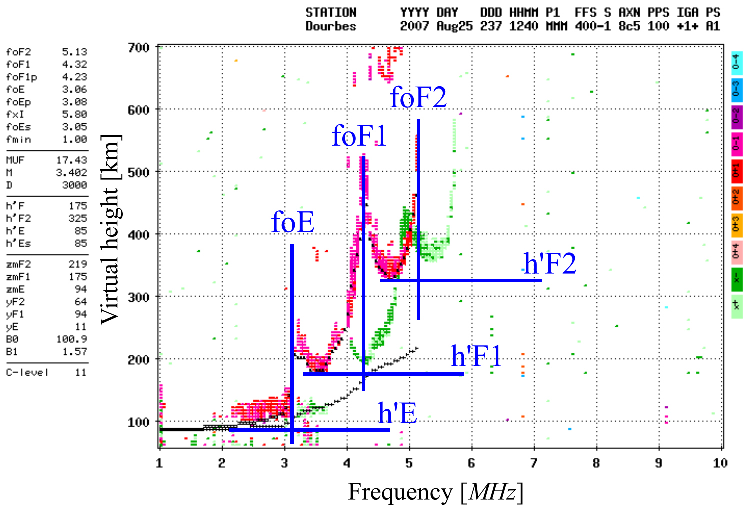

Figure 2.21: Example of ionogram from Dourbes digisonde (August 25th, 2007, 12h40 UT) [RMI et UMLCAR]

Among the existing types of ionosondes, one retains our attention for one of its models is installed at the Dourbes Geophysical Centre [RMI b]. The **digisonde** has been developed at the University of Massachusetts Lowell (UML) and is installed in more than 70 stations around the world [UMLCAR]. It is associated to an automatic scaling software called ARTIST including a true height inversion program denominated NHPC. The latter describes the electron density profile for each layer of the *bottomside* in terms of *shifted Chebyshev polynomials* [Huang et Reinisch, 1996]. It includes a valley model for the $E-F$ transition and approximates the *topside* profile by an α-*Chapman function* with a constant scale height derived from the bottomside profile shape near the F_2 peak [Reinisch et Huang, 2001]. Its results do thus not correspond to NeQuick output in an obvious way as shown in figure 2.22.

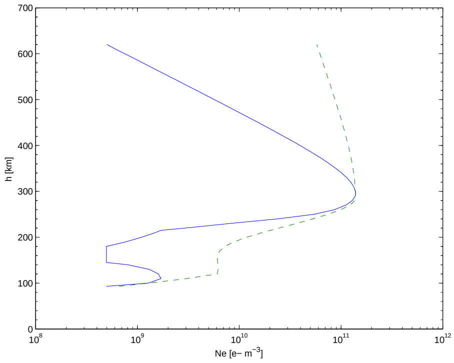

Figure 2.22: Electron density profiles from Dourbes digisonde (blue) and NeQuick (dashed green) for January 7th, 2007 at 21:40 UT

To use data from such equipments for validation purpose, we need orders of magnitude for their **accuracy** which depends on various factors e.g. the accuracy of the calibration method and the reading accuracy in ionograms scaling [Piggot et Rawer, 1978]. Common values for this latter contribution are 0.1 MHz for f_oF_2 and 0.05 for $M(3000)F_2$ so that the global accuracy can be twice or three times higher e.g. 0.2 MHz for f_oF_2 [Reinisch et al, 2005].

Anyway ionograms *scaling* constitutes a hard task, subject to interpretation as the plots obtained are rarely as clear as figure 2.21. It was originally performed manually and, even if automatic algorithms have been developed, the results must still be *checked manually* most of the time. Moreover missing parameters e.g. f_oE are sometimes modelled to provide complete profiles. *Models* are also employed to avoid some intrinsic limitations such as the description of inaccessible regions namely the valley between E and F layers and the topside where the electron density decreases with altitude.

2.4.2 GPS

If ionospheric effects must be suppressed when they provoke undesirable errors, we can employ the latter to get information about the ionosphere. Other growing techniques to collect ionospheric data, mainly TEC in this case, are thus based on GPS measurements. Lots of them are indeed available from permanent networks of GPS stations such as the International GNSS Service (IGS) stations, the European Reference Frame (EUREF) Permanent Network (EPN) or the Belgian Active Geodetic Network (AGN)[17].

To **compute** $sTEC$, *geometric free* (or ionospheric) *combinations*, $P^i_{p,GF}$ for codes and $\Phi^i_{p,GF}$ for phases, are computed aiming to cancel all terms frequency independent as opposed to free ionospheric combinations (cf. equation 2.28). In the resulting equations, hardware delays and ambiguities combine, neglecting multipath effects and noises[18].

$$\begin{aligned}
P^i_{p,GF} &= P^i_{p,2} - P^i_{p,1} \\
&= I^i_{p,2} - I^i_{p,1} + M^i_{p,2,m} - M^i_{p,1,m} - G^i_2 + G_{p,2} - (-G^i_1 + G_{p,1}) \\
&\quad + \varepsilon^i_{p,2,m} - \varepsilon^i_{p,1,m} \\
&= 40.3 \left(\frac{1}{f_2^2} - \frac{1}{f_1^2} \right) sTEC^i_p + CG^i_{p,GF}
\end{aligned} \tag{2.33}$$

---

[17] The latter includes the WALlonia Continuous Operating System (WALCORS), GPSBru for Brussels and the FLEmish POsitioning Service (FLEPOS)

[18] Notations may vary between sources.

$$\begin{aligned}\Phi^i_{p,GF} &= \Phi^i_{p,1} - \Phi^i_{p,2} \\ &= -I^i_{p,1} + I^i_{p,2} + M^i_{p,1,\varphi} - M^i_{p,2,\varphi} - p^i_1 + p_{p,1} - (-p^i_2 + p_{p,2}) \\ &\quad + \lambda_1 N^i_{p,1} - \lambda_2 N^i_{p,2} + \varepsilon^i_{p,1,\varphi} - \varepsilon^i_{p,2,\varphi} \\ &= 40.3\left(\frac{1}{f_2^2} - \frac{1}{f_1^2}\right) sTEC^i_p + CP^i_{p,GF} + N^i_{p,GF}\end{aligned} \tag{2.34}$$

$$CG^i_{p,GF} = -G^i_2 + G_{p,2} - (-G^i_1 + G_{p,1}) \tag{2.35}$$

$$CP^i_{p,GF} = -p^i_1 + p_{p,1} - (-p^i_2 + p_{p,2}) \tag{2.36}$$

$$N^i_{p,GF} = \lambda_1 N^i_{p,1} - \lambda_2 N^i_{p,2} \tag{2.37}$$

Phase combinations exhibit noise levels far lower than code measurements but they contain amibiguities ($N^i_{p,GF}$) which are now not entire anymore and an unknown term $CP^i_{p,GF}$ containing the hardware phase delays. Considering that the hardware delays are constant in time at least for a few hours, it will then be possible to take benefit from both combinations [Warnant, 1996, Warnant et Pottiaux, 2000].

The first step consists in the *determination of the hardware group delays* included in the term $CG^i_{p,GF}$ by means of pseudo-distance measurements. Substituting this expression in equation 2.38 allows then to compute the unknowns in the *phase combination*. Preferring the latter for its lower noise level, $sTEC$ can be deduced from equation 2.34 where the two last terms have been determined.

$$P^i_{p,GF} - \Phi^i_{p,GF} = CG^i_{p,GF} - CP^i_{p,GF} - N^i_{p,GF} \tag{2.38}$$

To compute **daily $vTEC$ profiles** for a given GPS station, the thin shell approximation is once more applied *mapping slant values to vertical* ones associated to the corresponding ionospheric points (cf. subsection 2.2.3). Indeed few satellites pass exactly at the station zenith so that it is needed to combine nearby converted $vTEC$ measurements assumed to represent the same ionospheric conditions. Data at ionospheric points in a *1°-latitude interval* around the station latitude are thus collected and *averaged every quarter*.

For this complex method, care must also be taken about the results **accuracy**. The latter suffers the most from the hardware group delays evaluation so that the uncertainty generally accepted varies between 2 and 3 $TECu$.

Chapter 3

NeQuick assessment

3.1 Description

3.1.1 Tools and method

As we have seen in last chapter, the ionosphere is a highly variable medium, depending on many parameters. Therefore its modelling proves itself tricky and evolves constantly. For **our interest**, the NeQuick model has been modified since it has been published by the ITU-R (cf. subsection 2.3.1) so that it appears interesting to

- point out the weaknesses of the ITU-R version (denoted as v1 from now on),
- describe the improvements of version 2 (denoted as v2 from now on)
- and to highlight elements to investigate further.

Among the different analysis methods using NeQuick in different ways, we chose as a first step to **uncouple NeQuick formulation from its underlying data**. To this extent, we replaced the CCIR maps of f_oF_2 and $M(3000)F_2$ by their measured values by means of a digisonde which we call DGS parameters from now on. In other words, we constrained the model to a daily behaviour, anchoring it in a real ionosphere, instead of considering the monthly median output[1]. We decided not to feed NeQuick with digisonde data for f_oE and f_oF_1 because they are less available and sometimes resulting from

---

[1] The DGS parameters condition the F_2 peak electron density and height but also the F_2 bottom thickness parameter and the topside shape parameter k involved in the F_2 top thickness parameter (cf. appendix A for details). Therefore we considered $M(3000)F_2$ as a primary parameter and we use its measured values instead of h_mF_2 which is not the only parameter depending on $M(3000)F_2$.

a model (cf. subsection 2.4.1 and [Huang et Reinisch, 1996]). We should also have needed to use NeQuick formulation for some of the missing values, especially for foF_1, leading to a mix of measured and modelled data for these parameters.

Furthermore we needed solar activity indices as additional input that we find from online data centers (monthly average solar flux Φ for f_oE from NGDC and R_{12} for topside parameter k from SIDC ; cf. subsection 2.1.3)[2].

Given this use of NeQuick, we compared its results with **two kinds of measurements**: vertical TEC, the valuable parameter for navigation purpose, computed by GPS and vertical electron density profiles from a digisonde[3]. We took there benefit of collocated independent data, a part exploited to constrain the model and the other as reference. As NeQuick is not expected to represent correctly geomagnetically active periods leading sometimes to abnormally low or high TEC values, we removed these periods for the statistical analysis thanks to geomagnetic activity indices from online data centers (Kp from NOAA and Dst from WDC Kyoto ; cf. subsection 2.1.4).

We performed the assessment by means of a **home-made Matlab GUI** enabling us to browse measured and modelled TEC and electron density profiles as well as input data. We also included a module allowing to analyse statistically TEC differences computing mainly bias and root mean square (RMS) for each year, month, day and UT in a month or year (cf. table 3.1).

	Absolute	Relative
Bias	$\langle TEC_{meas} - TEC_{mod} \rangle$	$\frac{\langle TEC_{meas} - TEC_{mod} \rangle}{\langle TEC_{meas} \rangle}$
RMS	$\sqrt{\langle (TEC_{meas} - TEC_{mod})^2 \rangle}$	$\frac{\sqrt{\langle (TEC_{meas} - TEC_{mod})^2 \rangle}}{\langle TEC_{meas} \rangle}$

Table 3.1: Statistical characterization of differences in TEC analysis

On the one hand, the bias, as a position parameter, indicates us the order of global overestimation or underestimation of the model where the RMS includes also dispersion information and is considered as a global quality index. On the other hand, absolute values will catch the attention of GPS users where relative will allow ionospherists to compare the quality of a model independently from

---

[2] R_{12} constitutes also an input for the CCIR maps requiring the recommended formula for flux conversion [ITU-R, 1999] and a 150-limit [ITU-R, 1997] which we have consequently removed.

[3] The profiles available are characterized by a 10-km height increment between varying height limits corresponding to low electron concentrations, a minimum of about 90 km and a maximum between 600 and 1000 km. They include a few additional points mainly the layer peaks and the valley limits.

the situation e.g. between low and high solar activity periods where TEC is respectively lower and higher.

In the following sections, we present the adopted **focusing process**: for a year of data,

- we compare the global TEC behaviour of each version of the model with GPS TEC,
- we turn to the best (resp. worst) month on relative RMS sense,
- we concentrate on the best (resp. worst) day in the best (resp. worst) month on relative RMS sense and we describe the daily TEC profile
- and we observe the electron density profile associated to a small (resp. big) TEC bias in the neighbourhood of the daily maximum of measured TEC.

Figures will systematically depict the results for v1 on the left and for v2 on the right.

3.1.2 Data set

We applied the methodology depicted in last subsection using data from the **Dourbes Geophysical Centre** [RMI b] (50.1°N ; 4.6°E ; cf. figure 3.1) where are installed the GPS EUREF station "DOUR" [EPN Central Bureau] and the UML digisonde DGS-256 "DB049" [RMI et UMLCAR].

Figure 3.1: Dourbes localization in Belgium

We collected data for **two years** characterized by different solar activity levels (high in 2002, low in 2006) for which we need to consider the **number of points** for a correct statistics interpretation (cf. table 3.2). For each year, we count maximum 35040 GPS TEC values (one every quarter) and 8760

DGS parameters couples and profiles (soundings every hour in 2002 and every 20 minutes in 2006 ; we kept the more restrictive one-hour rate). For the geomagnetic activity filter, we chose respectively 5 and -50 nT for Kp and Dst thresholds (storm thresholds from [Stankov, 2002]) and we used both indices because of their complementarity (cf. subsection 2.1.4).

	Maximum	2002	%	2006	%
GPS	35040	33979	97.0	34567	98.7
+ DGS	8760	6973	79.6	6150	70.2
+ storm filter	8760	6076	69.4	6009	68.6

Table 3.2: Maximum amounts of data and amounts of available data for 2002 and 2006

We observe only a few missing GPS points but rather degraded proportions of available DGS and filtered data calling some comments. In 2002, long periods are absent from the soundings (cf. figure 3.2 ; January and April 30th to May 8th) which accounts for a significative part of the missing points (960 out of 1787). Some of them include geomagnetic storms which could thus constitute one of the explanations for the missing ionograms (May 10th to 15th and November 21st to 24th ; 240 out of 827 remaining). Considering now the geomagnetic activity filter, we could define storms only as sufficiently long periods 20 of which we notice in the Dst plot (between 15 to 94 hours ; cf. 3.3) gathering a good portion of removed points (659 out of 897).

We note the same effect in 2006 (6 periods of 9 to 40 hours corresponding to 118 out of 141 removed data) but we state a poorer availability in the soundings consisting only in auto-scaled ionograms for that year. Partially due to technical problems, this weakness could thus also originate in the fact that they were not manually checked yet. Moreover the auto-scaling procedure could have left some unrealistic values of the DGS parameters.

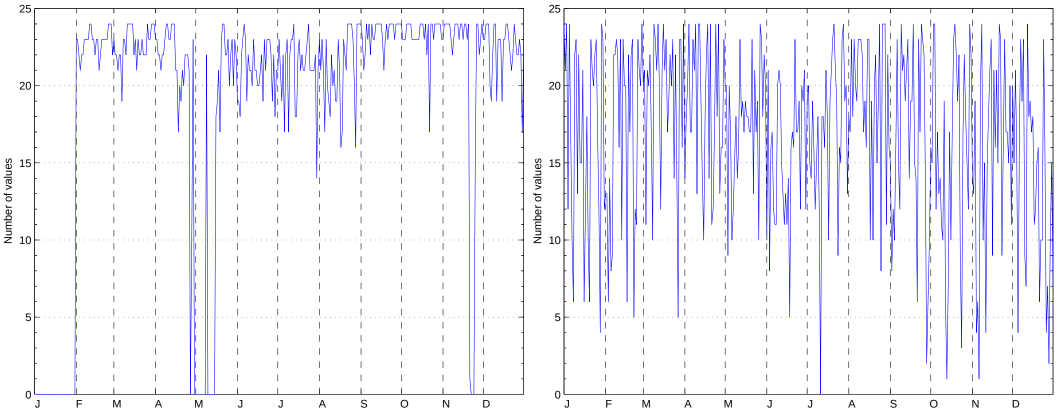

Figure 3.2: Daily amount of DGS data for 2002 (left) and 2006 (right)

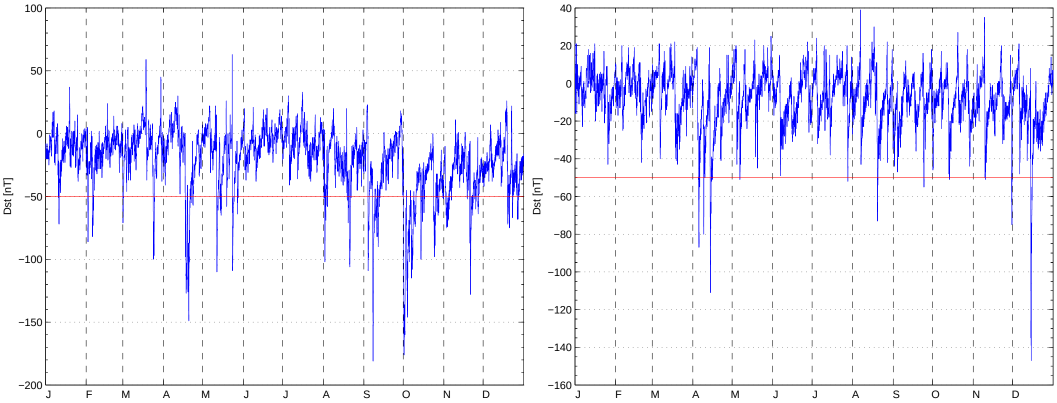

Figure 3.3: Dst index for 2002 (left) and 2006 (right)

3.2 TEC analysis

3.2.1 Yearly behaviour

The analysis of global TEC behaviour on a yearly basis informs us about the impact of **solar activity** insofar as we selected extreme conditions i.e. high and low levels. Table 3.3 illustrates this choice as the average solar indices are lower in 2006 than in 2002 as well as measured TEC. This parameter we consider in this section follows to a certain extent the evolution of the denser region of the ionosphere, the F_2 peak[4]. Indeed the latter electron concentration and height decrease respectively in function of f_oF_2 and of the inverse of $M(3000)F_2$ (cf. subsection 2.2.1).

	2002	2006
TEC_{meas} $[TECu]$	24.6	6.9
Number	6076	6009
R_{12}	100.8	16.2
Φ $[10^{-22}\ W\ m^{-2}\ Hz^{-1}]$	175.1	80.2
f_oF_2 $[MHz]$	7.4	4.5
$M(3000)F_2$	2.95	3.30

Table 3.3: Yearly average characteristics

Examining the **yearly statistics** for modelled TEC, we state an average low underestimation in 2002 which increases with v2 (cf. table 3.4). Never-

---

[4] Following the interpretation of subsection 2.3.1, the thickness parameter $B_{bot}^{F_2}$ will also force a diminution in TEC as it decreases when f_oF_2 declines or when $M(3000)F_2$ gets higher (cf. equation A.11).

theless this version seems better because of its lower RMS despite the bigger bias attesting really less spread differences.

We note the same improvement in 2006 where the RMS decreases even more (almost a half against a third) and the big average overestimation becomes a really small underestimation. However we must moderate these observations for 2006 because of the lower availability and quality of auto-scaled data partially due to technical problems (cf. subsection 3.1.2) and the lower TEC values. These implies partly bigger relative statistics and a growing influence of measurement accuracies (cf. subsections 2.4.1 and 2.4.2).

Globally we remark

- **average decreasing TEC** between v1 and v2
- and decreasing RMS testifying a **better global behaviour**.

	2002			2006		
	v1	v2	*Evolution*	v1	v2	*Evolution*
TEC_{mod} $[TECu]$	23.0	22.3	*96.9%*	8.7	6.6	*76.3%*
Bias $[TECu]$	1.6	2.3	*143.9%*	−1.8	0.2	*−13.2%*
Relative [%]	6.5	9.4		−26.5	3.5	
RMS $[TECu]$	7.7	5.2	*67.3%*	3.8	2.1	*56.2%*
Relative [%]	31.4	21.1		55.1	31.0	

Table 3.4: Yearly statistics

The above conclusion is confirmed observing **smoother, more symmetrical and narrower TEC differences distributions** for v2 than for v1 (cf. figures 3.4 and 3.5). The dissymmetry in v1 in 2002 seems to result from the superposition of two distributions, the principal one associated to an underestimation and the other one to an overestimation. This tendency is less clear in 2006 even if the curve is skewed to the right of the mean.

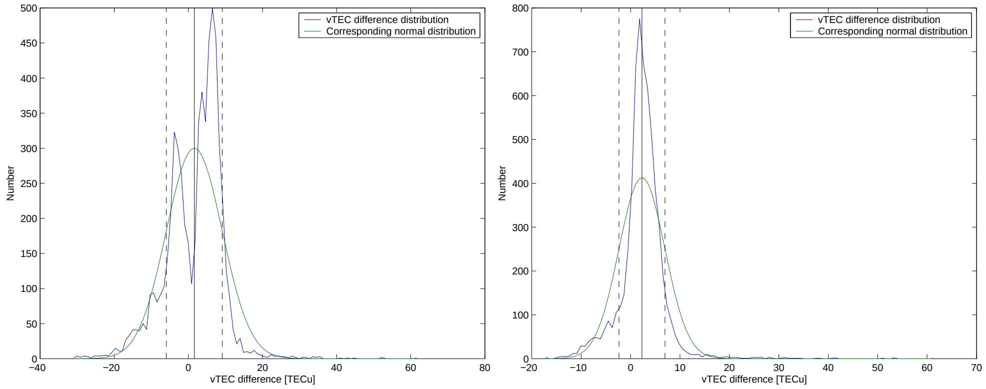

Figure 3.4: TEC difference distributions for 2002 (v1 left and v2 right)

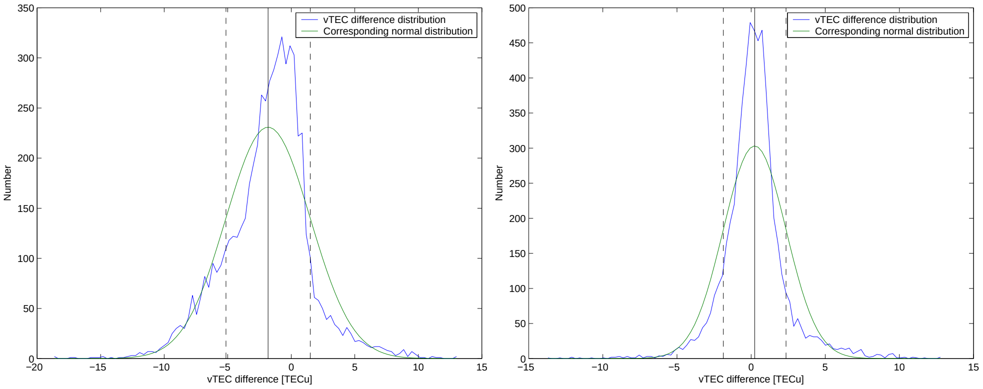

Figure 3.5: TEC difference distributions for 2006 (v1 left and v2 right)

3.2.2 Monthly behaviour

We get now to a finer timescale to inspect the **seasonal** variations. In *2002*, the equinoxes maxima appear modulated by solar activity (cf. figure 3.8) as average measured TEC is higher in March than in September (cf. figure 3.6). Their NeQuick representation, the best among all months (cf. figure 3.7), even improves with v2 which ensures also a better correspondance eliminating February maximum. We consider thus *September* as the best month for both versions (18.4% and 12.4% RMS) for the following of the analysis.

We observe then a double behaviour for v1 explicating the apparent distribution superposition (cf. figure 3.4): an overestimation occurs during autumn and winter and an underestimation takes place in spring and summer. We attribute this phenomenon to the topside shape parameter k formulas (cf. equation A.13) of which the selection corresponds to these periods. Moreover they are replaced by a unique formulation in v2 (cf. equation A.28) leading to the disappearing of the observed difference even if November and December still show a different behaviour than the other months (average overestimation).

We further note a minimum in measured TEC around winter solstice which implies high relative RMS for *December* (66.7% and 37.0%). Consequently we choose this month as worst allowing to study the suitable evolution of the above-mentioned behaviour between both NeQuick versions. Indeed most of its exaggerated values appropriately decrease accounting for the bigger average underestimation in v2 (cf. subsection 3.2.1).

Finally we suggest the consequence of the lack of January data: if available, the expected high TEC values should have increased average modelled TEC and decreased the bias as January belongs to the overestimated period.

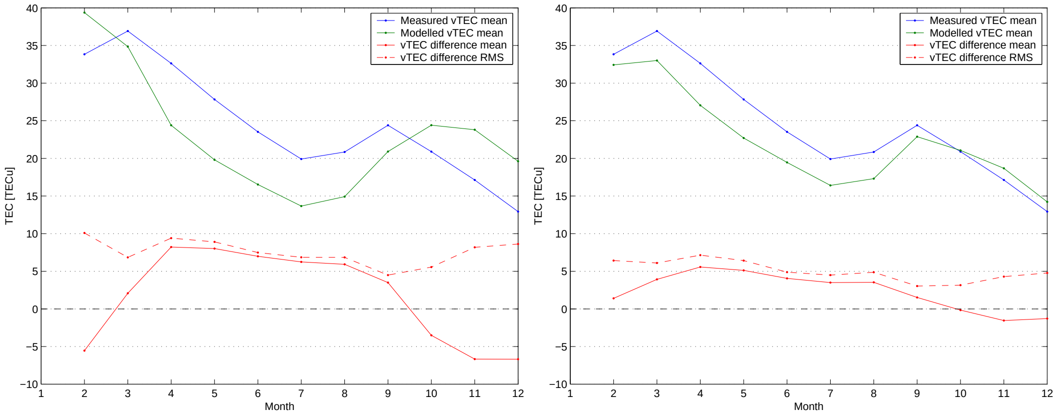

Figure 3.6: Monthly TEC values for 2002 (v1 left and v2 right)

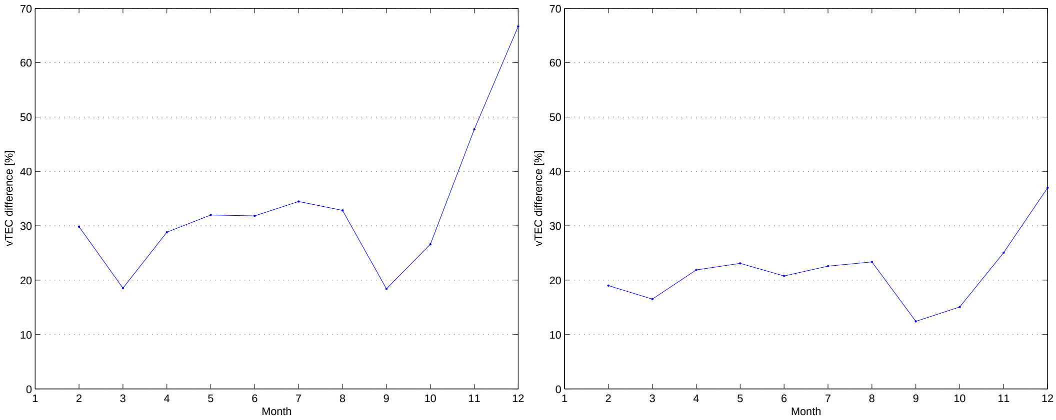

Figure 3.7: Monthly TEC difference relative RMS for 2002 (v1 left and v2 right)

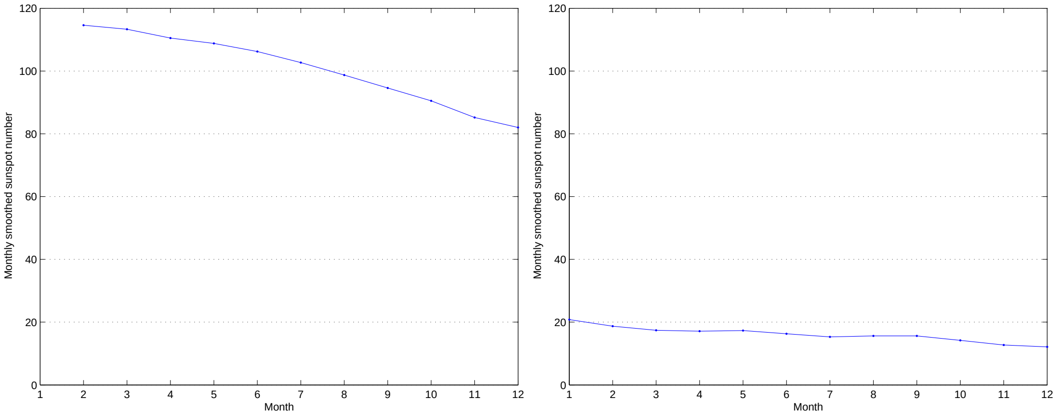

Figure 3.8: Monthly smoothed sunspot number R_{12} for 2002 (left) and 2006 (right)

For *2006*, we draw rather similar conclusions. On the one hand the maximum average measured TEC is now located before summer solstice (cf. figure 3.9) and is still well modelled with v1 but less well with v2 (cf. figure 3.10). On the other hand the double behaviour remains visible for v1, disappears for v2 but the best period becomes a little bit underestimated. We will thus dicuss these first disadvantages of v2 electing *June* as best month on relative RMS sense (25.5% and 24%) but with increasing bias (1.2% and 10.5%).

To explicate the small yearly underestimation, we observe that autumn and winter representation improve substantially for v2 but that October to December average TEC is still overestimated. For the same reason than in 2002, we retain anyway *December* as worst month for its decreasing high relative RMS (131.4% and 49.4%).

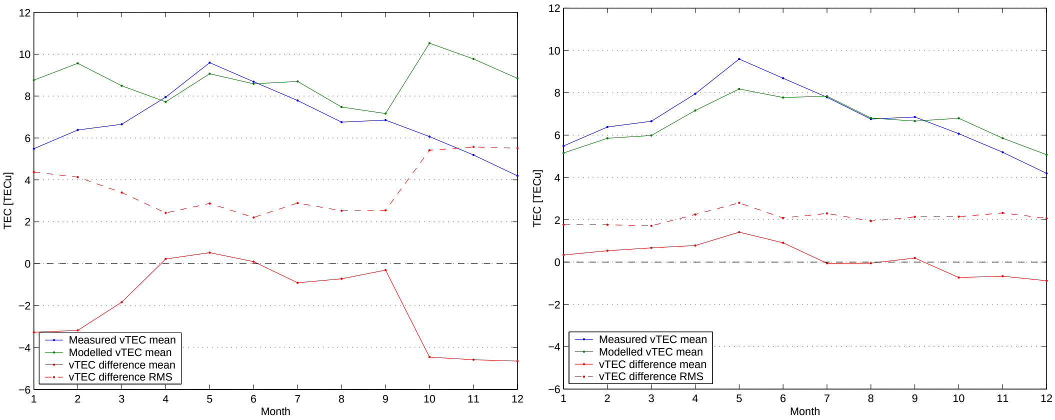

Figure 3.9: Monthly TEC values for 2006 (v1 left and v2 right)

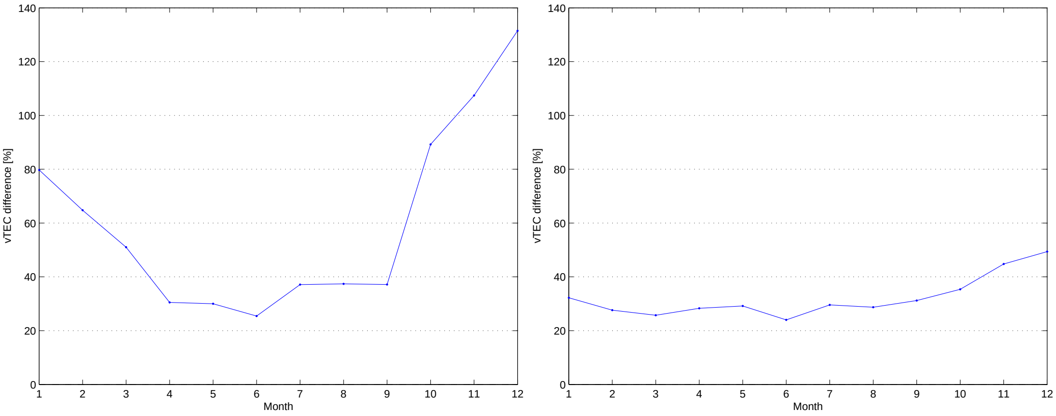

Figure 3.10: Monthly TEC difference relative RMS for 2006 (v1 left and v2 right)

We can now refine the conclusions of subsection 3.2.1 insofar as modelled TEC decreases on average with v2 essentially in autumn and winter but not enough for autumn. In spring and summer, it increases towards measured values in high solar activity period but decreases a little below reference data for low solar activity level. This evolution corresponds to the **unification of the topside shape parameter** k which **enhances NeQuick seasonal performances** as indicated by all decreasing relative RMS statistics.

	Sep. 2002	Dec. 2002	Jun. 2006	Dec. 2006
TEC_{meas} $[TECu]$	24.4	12.9	8.7	4.2
Number	574	645	458	399
R_{12}	94.6	82.0	16.3	12.1
Φ $[10^{-22}\ W\ m^{-2}\ Hz^{-1}]$	175.8	157.2	80.1	84.3
f_oF_2 $[MHz]$	7.7	5.9	4.8	3.9
$M(3000)F_2$	2.95	3.13	3.26	3.27

Table 3.5: Monthly average characteristics for selected months

	September 2002			June 2006		
	v1	v2	*Evolution*	v1	v2	*Evolution*
TEC_{mod} $[TECu]$	20.9	22.9	*109.5%*	8.6	7.8	*90.6%*
Bias $[TECu]$	3.5	1.5	*43.4%*	0.1	0.9	*910.0%*
Relative [%]	14.3	6.2		1.2	10.5	
RMS $[TECu]$	4.5	3.0	*67.6%*	2.2	2.1	*94.4%*
Relative [%]	18.4	12.4		25.4	24.0	
	December 2002			December 2006		
	v1	v2	*Evolution*	v1	v2	*Evolution*
TEC_{mod} $[TECu]$	19.6	14.2	*72.5%*	8.8	5.1	*57.4%*
Bias $[TECu]$	-6.7	-1.3	*19.3%*	-4.6	-0.9	*18.9%*
Relative [%]	-51.7	-10.0		-110.8	-21.0	
RMS $[TECu]$	8.6	4.8	*55.5%*	5.5	2.1	*37.6%*
Relative [%]	66.7	37.0		131.4	49.4	

Table 3.6: Monthly statistics for selected months

3.3 Case days

3.3.1 Best month in high solar activity

For each month identified in previous section, we study the **monthly median behaviour** as well as the **daily TEC profile** for a particular day. In september 2002, we observe a rather big range of mean measured TEC (between 18 and 31 $TECu$; cf. figure 3.11) which illustrates the variability around the monthly median behaviour (cf. subsection 2.1.3).

To measure the variation range, we do not consider September 4th neither 7th to 12th because of their low or zero number of associated measurements coming from their identification as geomagnetically active periods (cf. figure 3.13). Indeed diurnal (resp. night) missing data affect statistics differently as their higher (resp. lower) measured TEC can lead for example to lower (resp. higher) relative values (cf. figure 3.12).

The trends of measured and modelled TEC appear similar, with the expected average underestimation for v1 decreasing with v2 following the conclusions of subsection 3.2.2. We find the best representation (lower biases and relative RMS) in the end of the month for high measured TEC in particular for *September 22nd* selected as best case day (9.7% and 5.5% RMS).

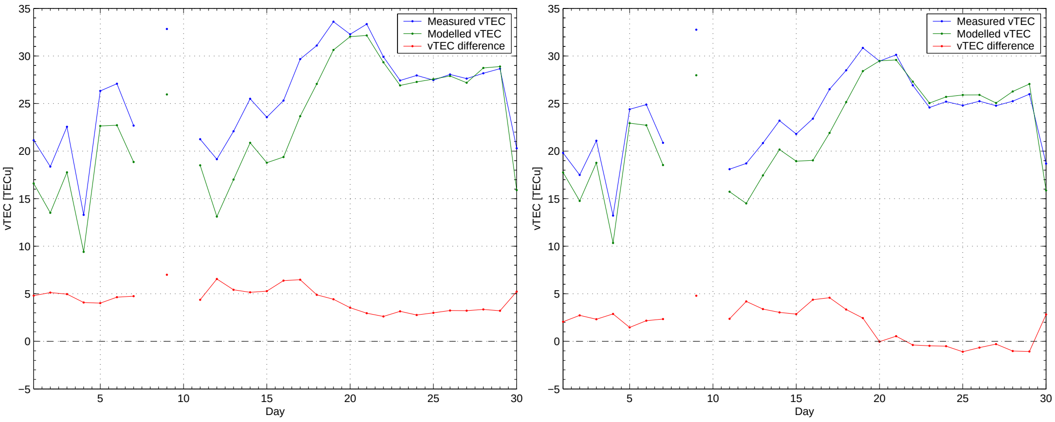

Figure 3.11: Daily TEC values for September 2002 (v1 left and v2 right)

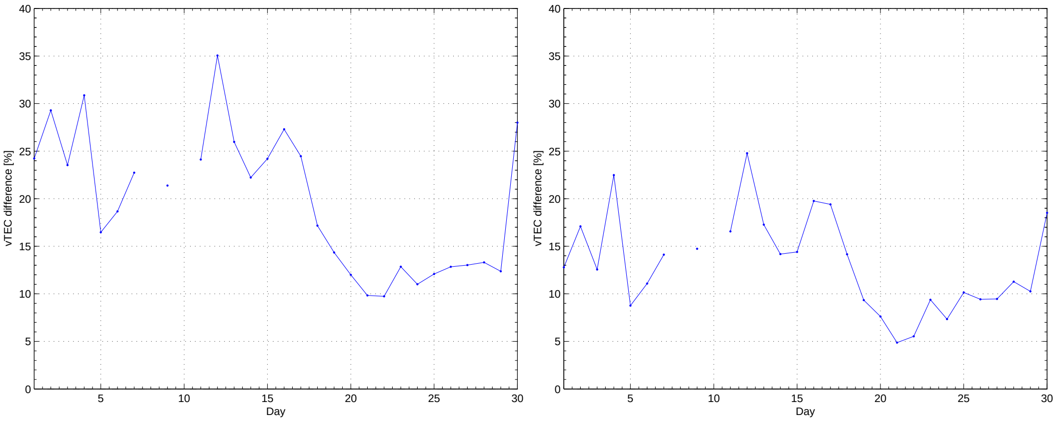

Figure 3.12: Daily TEC difference relative RMS for September 2002 (v1 left and v2 right)

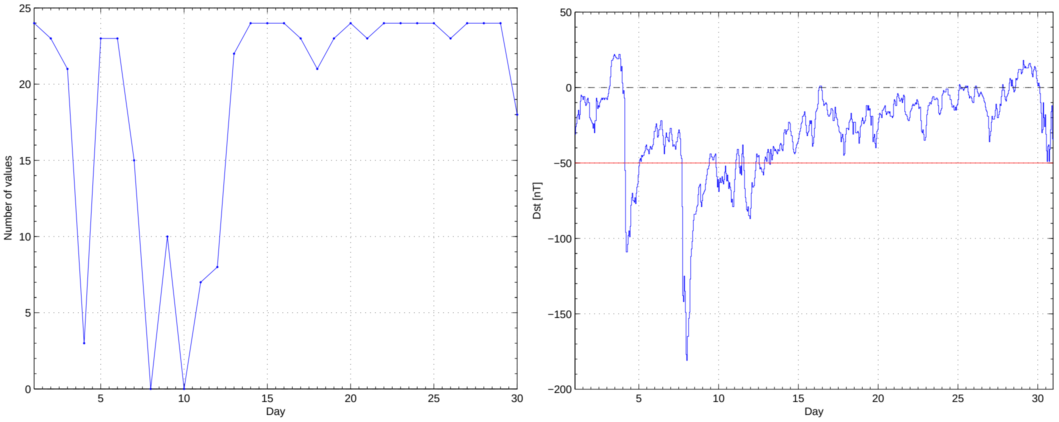

Figure 3.13: Daily number of values (left) and Dst index (right) for September 2002

Figure 3.14 shows the daily TEC profile for September 22nd with a maximum (45 $TECu$) just before local noon and a minimum (10 $TECu$) in the end of the night depicting the last variation described in subsection 2.1.3. Figure 3.15 reminds us about the major influence of f_oF_2 on modelled TEC according to reality as mentioned at the very beginning of this analysis.

The evolution between both versions of NeQuick, an average underestimation becoming a little overestimation, looks like a constant offset for all hours but smaller for some of them (10, 12, 13, 14 and 15) which already own the lower differences. These become then comparable with GPS TEC uncertainty ($2-3$ $TECu$) for all hours attesting the effectiveness of NeQuick for this situation. To deepen the analysis, we will examine the electron density profiles associated with the smaller TEC bias in the maximum around local noon, at *10 Universal Time (UT)* for both versions.

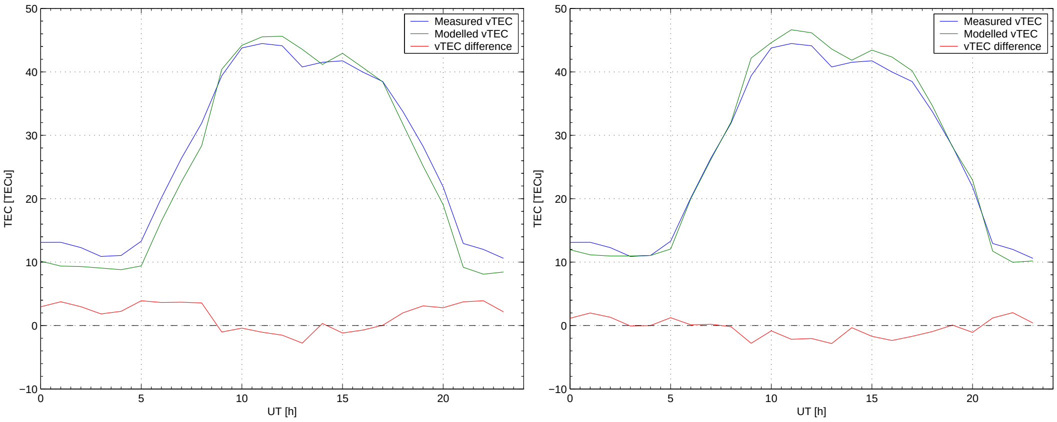

Figure 3.14: Hourly TEC values for September 22nd, 2002 (v1 left and v2 right)

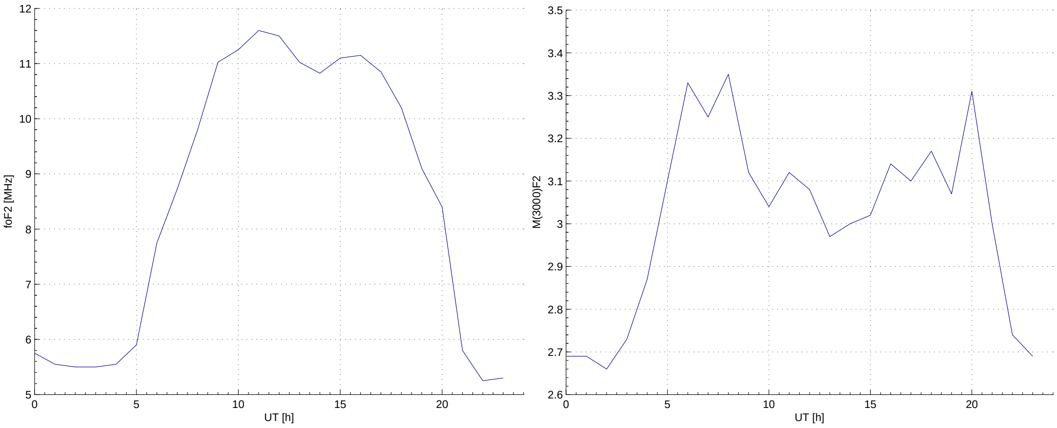

Figure 3.15: DGS parameters for September 22nd, 2002 (f_oF_2 left and $M(3000)F_2$ right)

3.3.2 Worst month in high solar activity

We expect a much more outstanding progress for December 2002. Providing the same precautions about the geomagnetically active periods (several data points removed for December 19th to 21st, 23rd and 27th ; cf. figure 3.18), we still observe variations around a monthly median (between 10 and 16 $TECu$) and similar trends of measured and modelled TEC (cf. figure 3.16).

As for monthly statistics, the average overestimation decreases very much with v2. For both versions, the bias oscillates in an interval of 2 $TECu$ around a constant value apart for the last days of the month. For these, lower measured TEC raise the relative RMS as for *December 29th* which we take as worst case day for its highest relative RMS values (116.9% and 64.5%).

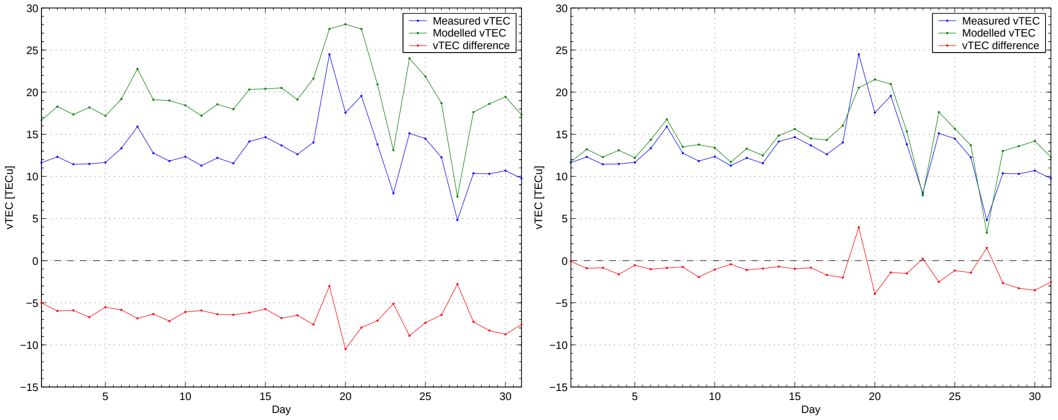

Figure 3.16: Daily TEC values for December 2002 (v1 left and v2 right)

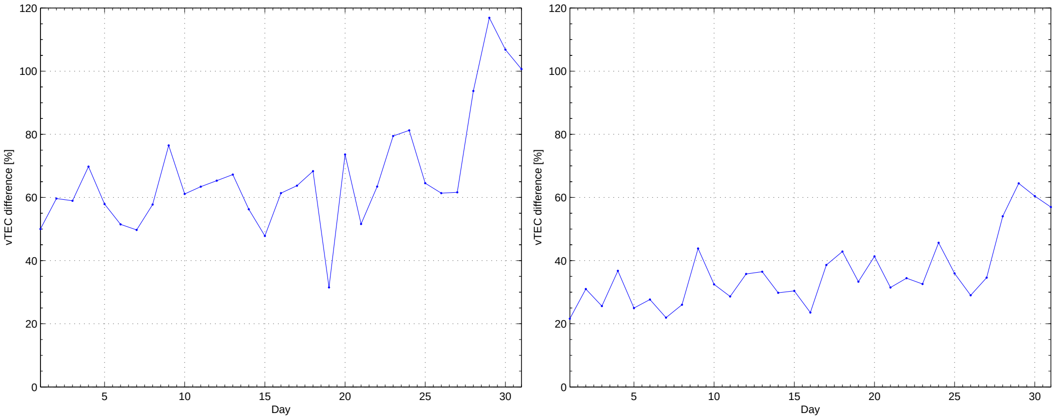

Figure 3.17: Daily TEC difference relative RMS for December 2002 (v1 left and v2 right)

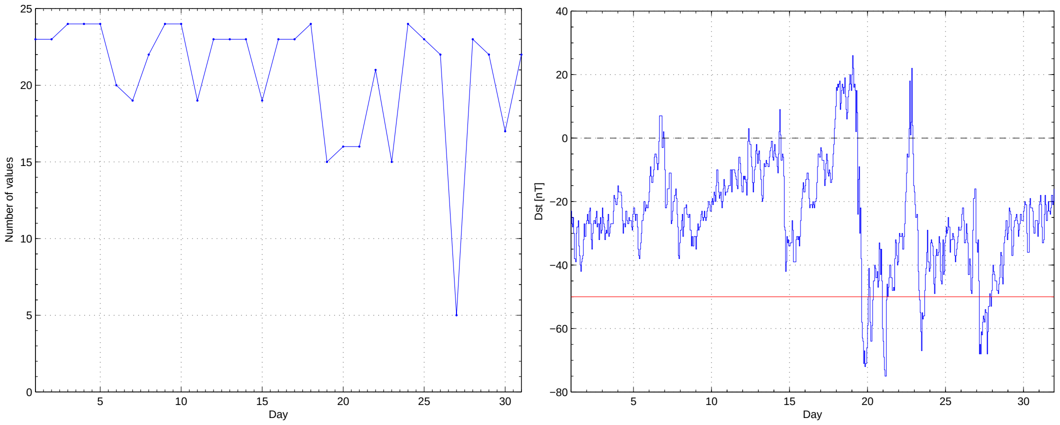

Figure 3.18: Daily number of values (left) and *Dst* index (right) for December 2002

For a high solar activity level, TEC around solstice winter reveals itself far inferior to autumn (cf. figure 3.19) with daily maximum of 26 $TECu$ and minimum of 3 $TECu$ which also follows later sunrise. We still recognize the repercussion of f_oF_2 in the shape of measured and modelled TEC profiles (cf. figure 3.20) but we find a lower TEC maximum for the same frequencies (around 11 MHz) then for September 22nd. Turning to $M(3000)F_2$, we discover higher factors (3.6 instead of 3.1) giving way to lower F_2 peak heights as already mentioned but also smaller thicknesses decreasing TEC to a certain extent (cf. equation A.11 and thickness interpretation subsection 2.3.1).

This effect, apparently not well taken into account in v1, could still suffer from a not sufficiently adequate representation in v2. Indeed the overestimation, decreasing more like a scaling with little lower low TEC (-2 $TECu$) and high values appreciably eroded (-10 $TECu$), remains huge with a maximum at *11 UT* for which we will study the electron density profiles.

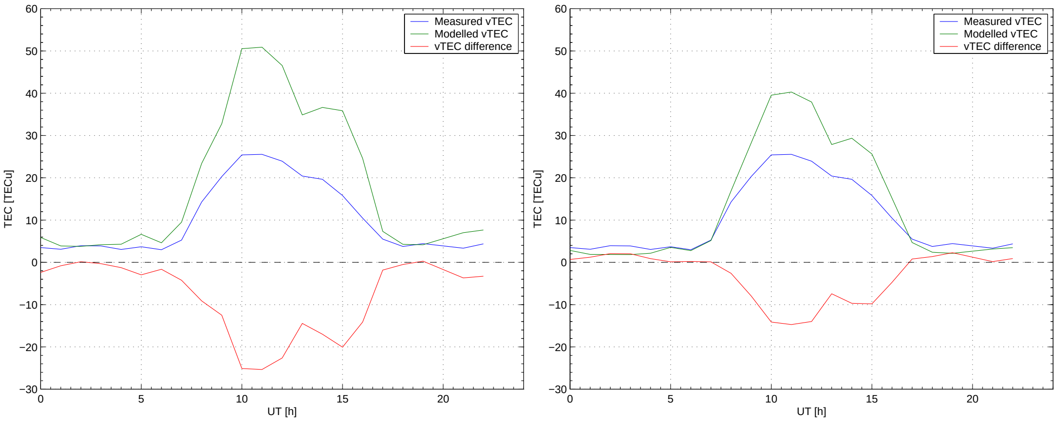

Figure 3.19: Hourly TEC values for December 29th, 2002 (v1 left and v2 right)

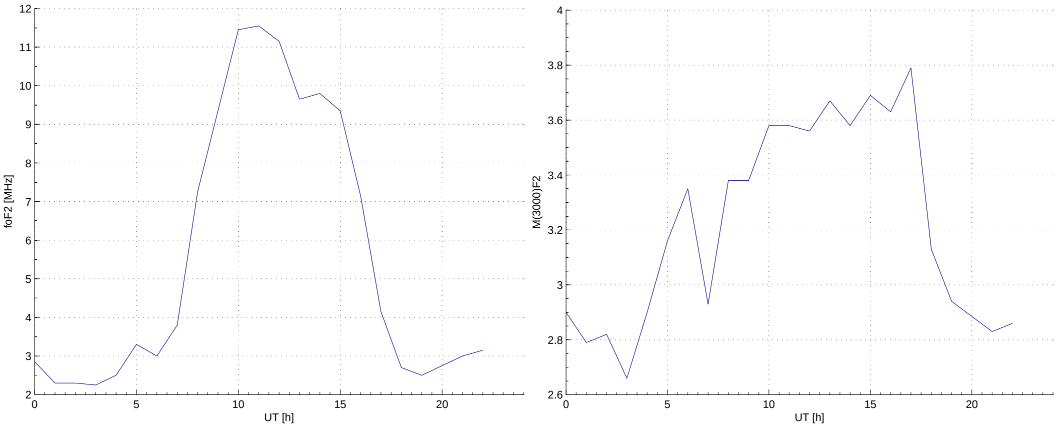

Figure 3.20: DGS parameters for December 29th, 2002 (f_oF_2 left and $M(3000)F_2$ right)

3.3.3 Best month in low solar activity

June 2006 belongs to a period where an increasing underestimation between v1 and v2 attenuates the enhanced quality (decreasing relative RMS). The average adequation of measured and modelled values with v1 becomes indeed an underestimation for v2 for all days (cf. figure 3.21). Furthermore the varying evolution for relative RMS denotes a compromise between worse biases and less spread data (cf. figure 3.22).

We still have to pay attention to the number of values included in statistics (cf. figure 3.23). Missing soundings probably due to technical problems lead here to a clearly poorer data availability highlighting the need for better quality data for 2006 so that we cannot compare daily statistics so easily. To identify the best case day (low bias and relative RMS), we consider those with a high number of available data and we pick out *June 22nd* as an example of potential degradation of v2 (increasing bias and relative RMS: 17.7% and 21.7%).

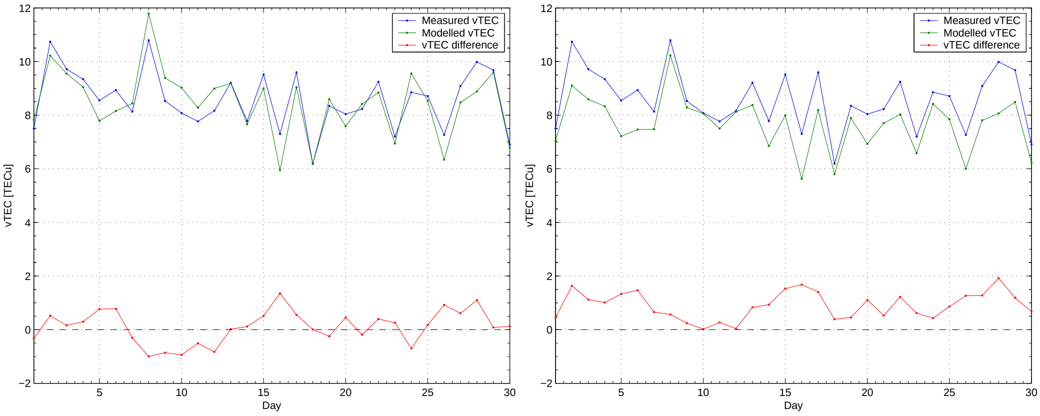

Figure 3.21: Daily TEC values for June 2006 (v1 left and v2 right)

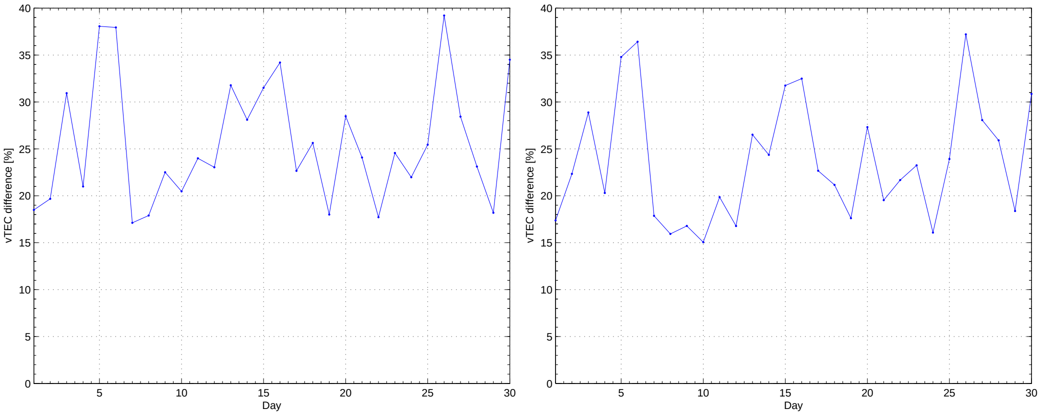

Figure 3.22: Daily TEC difference relative RMS for June 2006 (v1 left and v2 right)

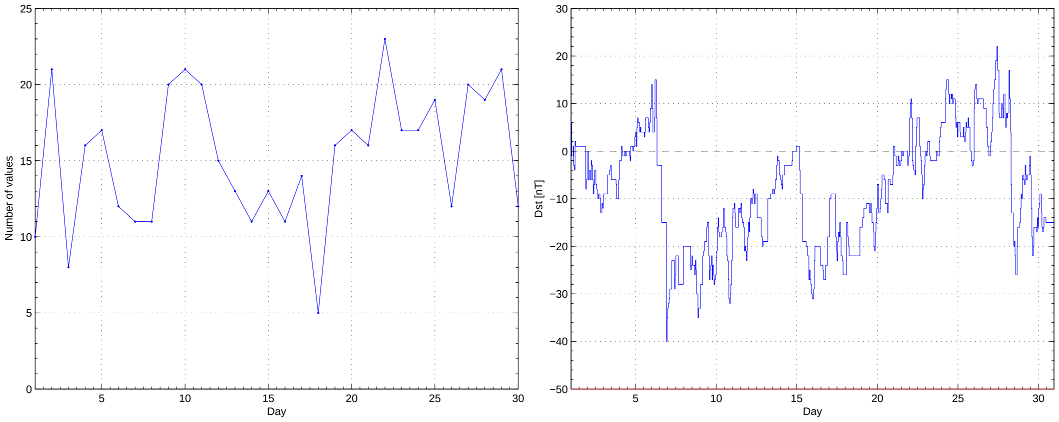

Figure 3.23: Daily number of values (left) and Dst index (right) for June 2006

The daily profile for this day exhibits the characteristics already pointed out (maximum of 12 $TECu$ before local noon and minimum of 4 $TECu$ in the end of the night) but significatively smaller TEC by comparison with high solar activity case days (cf. figure 3.24). It also presents a second maximum in the evening (14 $TECu$) which is regularly observed during the months around summer solstice.

In addition to the parallelism with f_oF_2, we detect a new influence of the DGS parameters on modelled TEC: a bigger variability following $M(3000)F_2$ during the day (cf. figure 3.25). It could be more visible here because of the lower average TEC but the peaks of the transmission factor (at 13 and 20 for example), corresponding to local TEC minima, suggest to investigate the auto-scaling results, not yet manually checked.

We finally discuss the increasing underestimation noting that only the modelled values above 6 $TECu$ declined, in particular the one with the smaller bias before local noon at *10 UT* which we keep for profiles analysis.

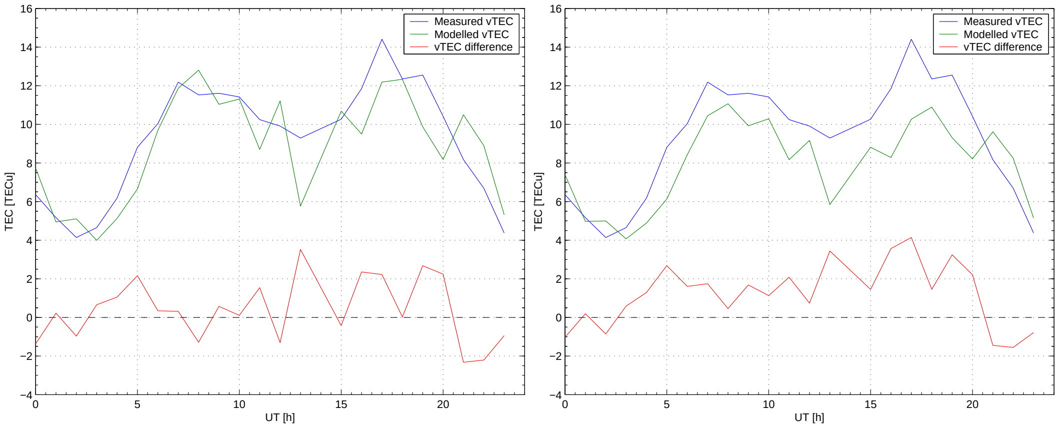

Figure 3.24: Hourly TEC values for June 22nd, 2006 (v1 left and v2 right)

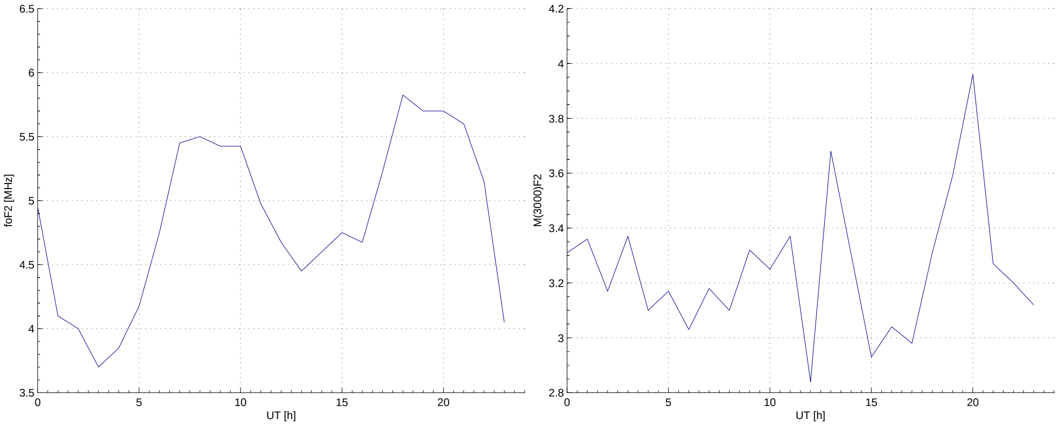

Figure 3.25: DGS parameters for June 22nd, 2006 (f_oF_2 left and $M(3000)F_2$ right)

3.3.4 Worst month in low solar activity

Most of the observations of previous subsections apply once more to the worst month in low solar activity characterized by the lowest average TEC in the data set (4.2 $TECu$). The reference TEC, slightly oscillating around the monthly median[5], is exaggerated with v1, a weakness which evolves the best on a relative scale with v2 (cf. figure 3.26).

Moderating this cheerful conclusion because of the low data availability (cf. figure 3.28), we adopt as worst case day (high relative RMS) with a high number of data points, *December 9th* with its residual overestimation and its reduced relative RMS (150.4% and 57.7%).

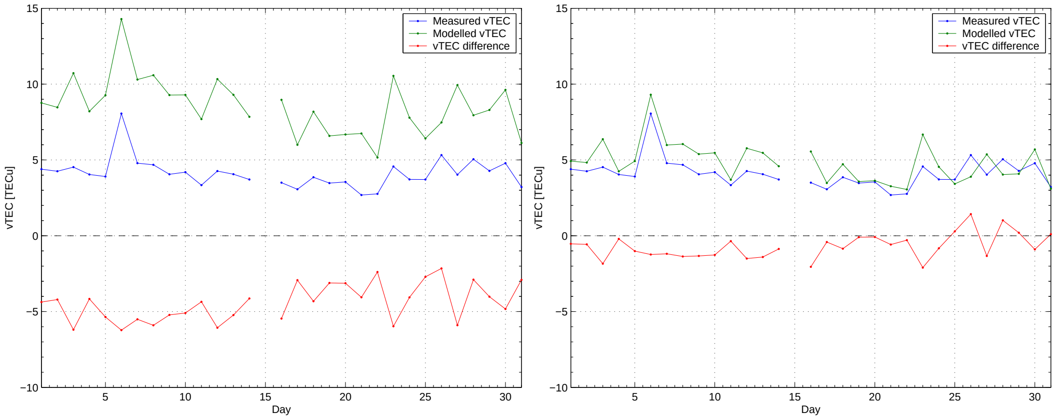

Figure 3.26: Daily TEC values for December 2006 (v1 left and v2 right)

---

[5] The only exception on December 6th corresponds to an X-6 solar flare associated to a famous radio burst which caused many receivers to loose GPS signals [NOAA, 2007].

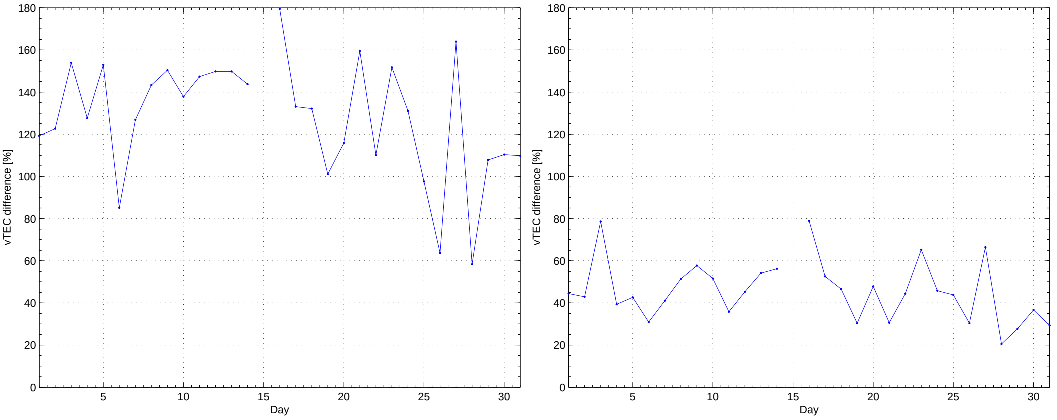

Figure 3.27: Daily TEC difference relative RMS for December 2006 (v1 left and v2 right)

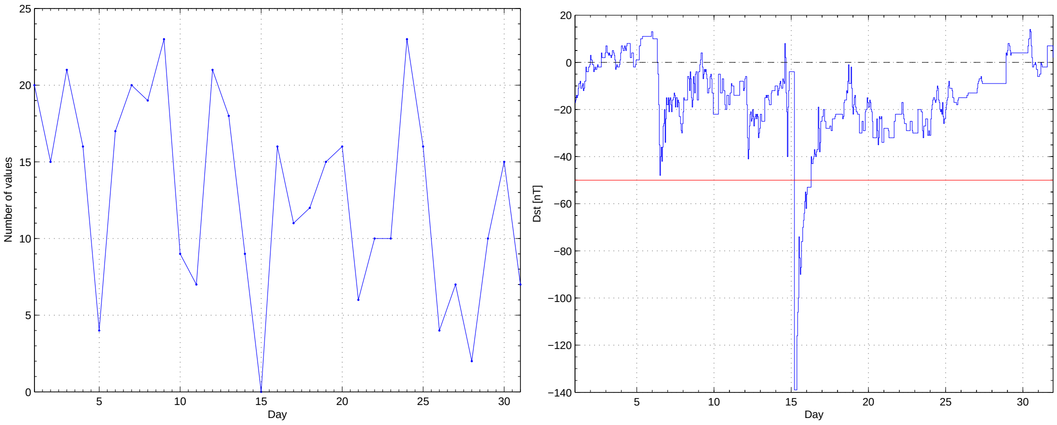

Figure 3.28: Daily number of values (left) and Dst index (right) for December 2006

In this case, the common features of TEC curve occur both later in daytime then for the best case: the 8-$TECu$ maximum arises after local noon and the minimum (1.5 $TECu$) follows later sunrise (cf. figure 3.29). As modelled TEC strongly depends on f_oF_2, we discover a secondary maximum in their graphs absent from the reference (cf. figure 3.30). We attribute this phenomenon either to an irregular value to be removed after manual ionogram examination, either to the fundamental difference between GPS averaged data (on a quarter) and digisonde instantaneous soundings or to a problem with GPS TEC.

For the profiles comparison, we take *13 UT* coincident with the diurnal maximum for which NeQuick results drop between both versions.

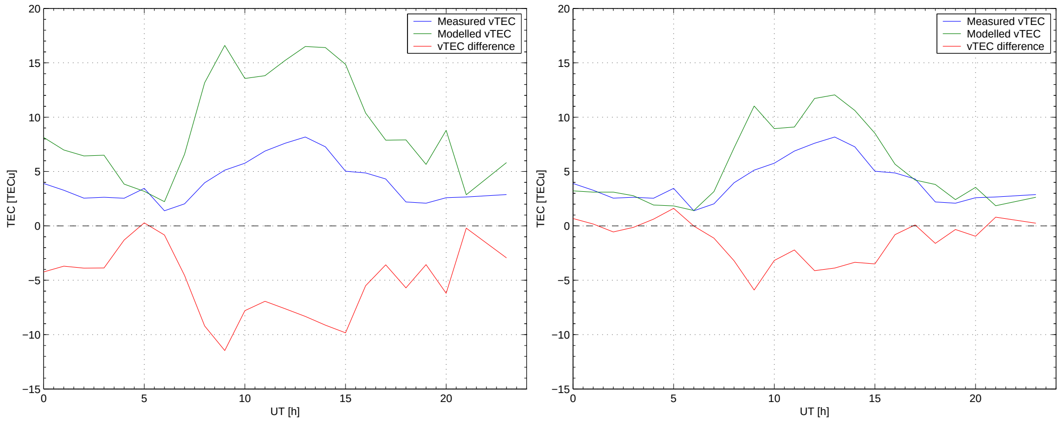

Figure 3.29: Hourly TEC values for December 9th, 2006 (v1 left and v2 right)

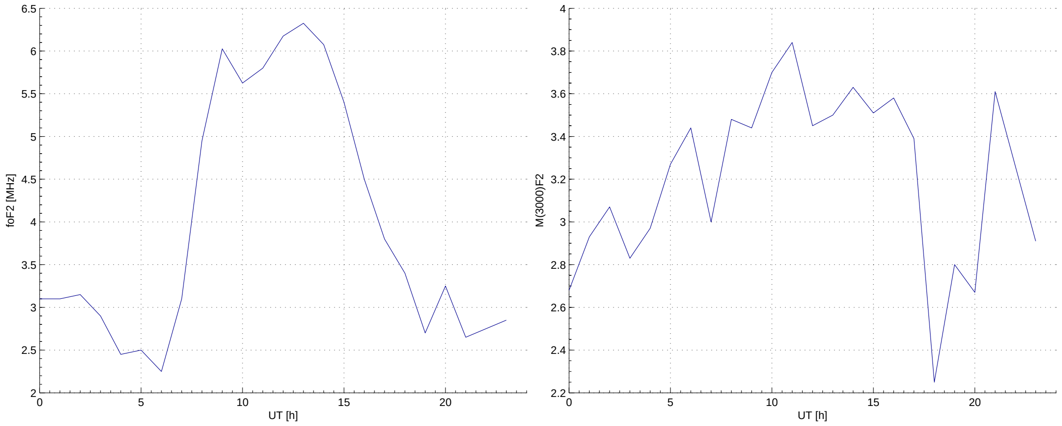

Figure 3.30: DGS parameters for December 9th, 2006 (f_oF_2 left and $M(3000)F_2$ right)

3.3.5 Synthesis

During the case day selection process,

- we observed **measured TEC variations**, seasonal, with departures from monthly median behaviour, and daily, with maximum values around local noon greatly varying with solar activity and season ;
- for each month considered, we noticed **similar trends of measured and modelled TEC** for both versions apart from some days partly because of missing and filtered data ;
- we watched the **evolution between v1 and v2**, compared to a scaling, constituting a clear **improvement** apart from one case (low solar activity summer solstice) ;

- we began to describe how the **DGS parameters** could **condition NeQuick** and we are looking forward to studying electron density profiles for identified days and hours to deepen our understanding of their effect on anchor points and thickness parameters.

3.4 Electron density profiles analysis

3.4.1 Best month in high solar activity

Even if TEC receives our principal interest because of its importance for navigation, the main advantage of NeQuick by comparison with other models such as Klobuchar algorithm resides in its ability to predict electron densities integrated in a second step. On the one hand it allows to consider slant rays without mapping functions to convert vertical TEC. On the other hand it permits us now to pursue our investigation decomposing TEC in its underlying vertical electron density profile.

However we will miss a potential part of the difference between measured and modelled TEC as errors on DGS parameters will affect both measured and modelled profiles in a similar way. For instance the F_2 peak electron concentration corresponds in all profiles, as it is directly computed from f_oF_2, illustrating the anchoring process we successfully applied (cf. subsection 3.1.1). For the peak height, we observe the expected difference resulting from the input of $M(3000)F_2$ and not directly h_mF_2 (cf. figure 3.31). It is however small in this case (294.3 km vs. 283.9 km measured) and consistent with DUDENEY's formula (cf. equation A.8) generally accepted accuracy (±20 km [ZHANG et al., 1999]).

Regarding the bottomside, the region we may compare with ionosonde profiles, the first distinctive feature we notice is a higher and denser E peak (3.6 MHz at 120 km vs. 3.4 MHz at 101.8 km). NeQuick indeed fixes h_mE at 120 km so that the whole profile seems a bit too high and the $E-F$ valley vanished. Furthermore we kept NeQuick simplified formulation for f_oE computing a monthly median value for this parameter (cf. equation A.19) but the impact of this approximation appears rather small for h_mF_2 ($\Delta h_mF_2/h_mF_2 \simeq 0.4\%$), for the bottomside ($\Delta TEC_{bot}/TEC_{bot} \simeq -0.7\%$ for v1 and -1.2% for v2) or for the topside ($\Delta B_{top}^{F_2}/B_{top}^{F_2} \simeq -0.4\%$ and -0.2%)[6].

---

[6] For these calculations, we never used the function junction for piece-wise functions (cf. equation A.34) neither the restricted exponentials (cf. equation A.35). To obtain TEC_{bot}, we integrated analytically the five semi-Epstein layers constituting NeQuick bottomside (cf. equation A.1) between 100 km and h_mF_2 without considering the fading-out effect and we neglected the lowest part of the ionosphere (below 100 km). These approximations should only lead to little overestimations of NeQuick results.

The consequences on the F_1 layer, depending on f_oE on various ways as f_oF_1 is estimated as 1.4 f_oE, should thus not modify our statement of an underestimation of the bottomside electron density. A quantitative comparison of the F_1 layer characteristics is more hazardous as no ionosonde measurement of f_oF_1 nor h_mF_1 is available and most of the definitions were modified in v2. However we notice an appropriate evolution towards a denser profile thanks to these developments.

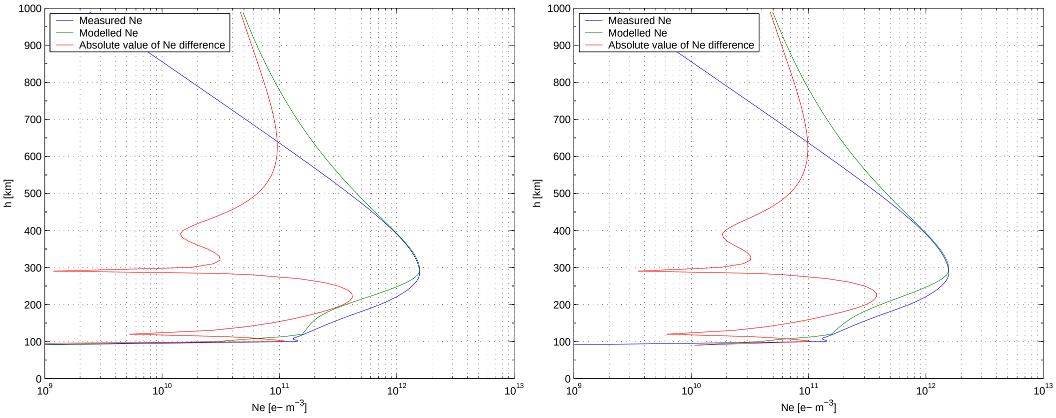

Figure 3.31: Measured and modelled profiles for September 22nd, 2002 at 10 UT (v1 left and v2 right)

We cannot distinguish any clear evolution of the topside representation between NeQuick versions so that we need to try somehow to dissociate it from the bottomside. To this extent, we integrate numerically the bottomside profiles[7] and we subtract the obtained bottomside TEC (TEC_{bot}) from corresponding global TEC to get an estimate of topside TEC (TEC_{top}).

For September 22nd at 10 UT, all TEC values slightly increase with v2 compared to v1 (cf. table 3.7) which was expected for both bottomside and global profiles. In the case of the topside, it corresponds to the modification of the shape parameter k leading to a higher thickness parameter $B_{top}^{F_2}$[8]. Anyway we state that NeQuick still overestimates the topside highlighting for the first time a compromise between topside and bottomside. The apparent very good behaviour in TEC appears in fact as a compensation from the too dense topside to the too weak bottomside.

---

[7] We employ the trapezoidal rule [Weisstein c] for we got 10-km height-separated points apart from some of them e.g. measured F_2 layer peak. This one allows us to split the ionosonde profile with a good accuracy. For NeQuick profiles, we add the appropriate points for the same reason and we use the same integration method to ensure similar integration errors.

[8] The direct comparison of v1 and v2 k parameters would not be relevant because of the suppression in v2 of the corrective factor v of the order of 1.5 in selected situations (cf. equation A.13). We must consider k/v for v1 and k for v2 i.e. the ratio $B_{top}^{F_2}/B_{bot}^{F_2}$ as the bottom thickness parameter formulation does not change.

We would thus like to quantify the bottomside thickness to evaluate $B_{bot}^{F_2}$ accuracy which constitutes a potential source of error we did not consider yet. Following the illustration of subsection 2.3.1, computing so-called equivalent thicknesses B_{bot}^{eq} dividing TEC_{bot} by 2 N_mF_2 could constitute an interesting means and confirms the improvement of v2, to be extended. More rigorously, we should follow $B_{bot}^{F_2}$ definition (cf. appendix A.2) calculating the height or gradient of the inflection point at the base of the F_2 layer to compare pseudo-thicknesses but we would then need a better height resolution than 10 km. In this case, a raise of $B_{bot}^{F_2}$ seems suitable and would also decrease k ($dk/dB_{bot}^{F_2} \simeq -0.50\ km^{-1}$) which should anyway decline further to diminish $B_{top}^{F_2}$.

	Reference	v1	v2
TEC $[TECu]$	43.8	44.2	44.6
TEC_{bot} $[TECu]$	13.6	11.4	11.7
TEC_{top} $[TECu]$	30.2	32.8	32.9
B_{bot}^{eq} $[km]$	43.3	36.2	37.4
$B_{bot}^{F_2}$ $[km]$		32.3	
$B_{top}^{F_2}$ $[km]$		58.1	58.4
Ratio		1.80	1.81

Table 3.7: Profiles characteristics for September 22nd, 2002 at 10 UT (v1 left and v2 right)

3.4.2 Worst month in high solar activity

Winter 2002 shows also a good agreement for h_mF_2 (237.0 km vs. 231.9 km measured) and a small difference for the E peak (2.8 MHz at 120 km vs. 2.7 MHz at 110 km). To obtain the ionosonde critical frequency, we inverted the electron concentration at 110 km as no value was available. We knew indeed that this parameter was computed from a model for ionograms without E trace and associated to a 110-km height. The replacement of missing data by modelled ones justifies our choice of using NeQuick simplified formulation for f_oE and f_oF_1 (cf. subsection 3.1.1) even if it is again of little consequence ($\Delta h_mF_2/h_mF_2 \simeq 0.3\%$; $\Delta TEC_{bot}/TEC_{bot} \simeq -0.8\%$ for v1 and -0.9% for v2 ; $\Delta B_{top}^{F_2}/B_{top}^{F_2} \simeq 1.5\%$ and -0.1%).

Between the E and F_2 peaks, the latest version of NeQuick computes little higher electron concentrations (cf. figure 3.32) as for the best case and for the same reason (E and F_1 layers modifications). However NeQuick inflates here this region accounting for a part of the global TEC overestimation. The latter drops between both versions following the topside as we can observe from the figure.

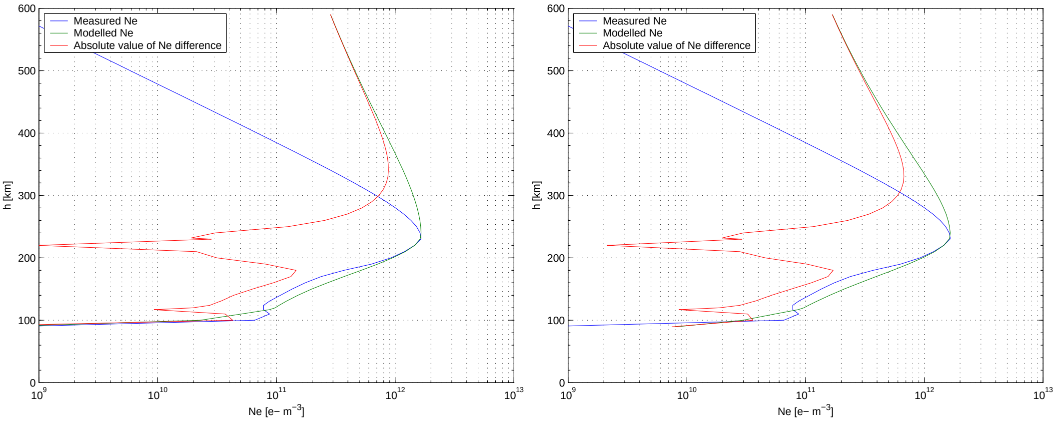

Figure 3.32: Measured and modelled profiles for December 29th, 2002 at 11 UT (v1 left and v2 right)

The TEC dissociation corroborates our considerations of too dense bottom and topsides as well as the significative improvement from v2 new k formulation (cf. table 3.8). Nevertheless we still need to diminish TEC_{top}, which proves as the biggest component of TEC (almost three quarters in this case), by 13 $TECu$ and we could reach this aim by acting on $B^{F_2}_{top}$ i.e. $B^{F_2}_{bot}$ or k. As for the best case, k should apparently decrease further but on the contrary $B^{F_2}_{bot}$ also. Higher values of $M(3000)F_2$, already high by comparison with best case (3.58 vs. 3.04), could imply such evolution as well as an F_2 peak lowering consistent with its too high height. We note indeed the big influence of $M(3000)F_2$ on these parameters comparing their values with those of the best case characterized by a similar F_2 critical frequency ($\Delta B^{F_2}_{bot} \simeq 8.9\ km$ and $\Delta h_m F_2 \simeq 57.3\ km$).

	Reference	v1	v2
$TEC\ [TECu]$	25.6	50.9	40.3
$TEC_{bot}\ [TECu]$	6.7	8.1	8.2
$TEC_{top}\ [TECu]$	18.9	42.8	32.0
$B^{eq}_{bot}\ [km]$	20.2	24.5	24.9
$B^{F_2}_{bot}\ [km]$		23.4	
$B^{F_2}_{top}\ [km]$		71.9	53.8
Ratio		3.07	2.30

Table 3.8: Profiles characteristics for December 29th, 2002 at 11 UT

3.4.3 Best month in low solar activity

As we observed in section 3.3, lower TEC sometimes lead to surprises as the situation chosen as best case for the low solar activity level becomes apparently slightly worse for v2. We state indeed bigger differences for h_mF_2 (225.1 km vs. 210.5 km measured) and for the E peak (3.2 MHz at 120 km vs. 3.5 MHz at 90.6 km) implying more than a too high modelled profile (cf. figure 3.33). Taking the ionosonde f_oE as an input would not influence h_mF_2 at all nor the topside[9] as the ratio f_oF_2/f_oE in DUDENEY's formula is limited at a minimum value of 1.75 superior to the actual ratio in both cases.

However the modelled bottomside, once more less underestimated in v2, increases then in v2 ($\Delta TEC_{bot}/TEC_{bot} \simeq 0.9\%$ for v1 and 15.4% for v2) so that its analytically integrated TEC reaches the numerically integrated measured value (cf. table 3.9). Furthermore the most visible improvement between NeQuick versions in this case i.e. the intended removing of unrealistic features leads to an appropriate positive TEC difference bigger than for the other cases. This could partially explain the reinforced average TEC in summer and spring for the high solar activity level (cf. subsection 3.2.2).

The comparison of the topside between v1 and v2 shows finally the well-known decline which is unfortunately too heavy in this case as we learn from the TEC dissociation. An increase of both thickness parameters seems thus necessary.

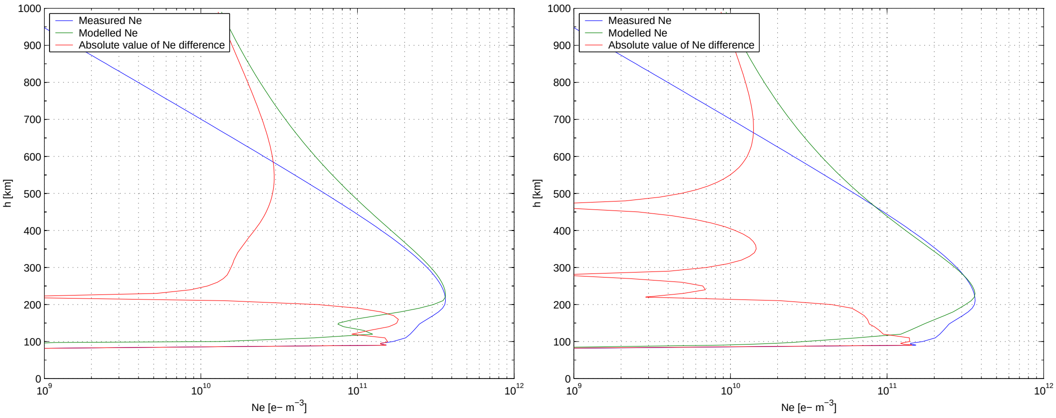

Figure 3.33: Measured and modelled profiles for June 22nd, 2006 at 10 UT (v1 left and v2 right)

---

[9] This region depends on f_oE only through k function itself of h_mF_2.

	Reference	v1	v2
TEC $[TECu]$	11.4	11.3	10.3
TEC_{bot} $[TECu]$	3.3	2.2	2.8
TEC_{top} $[TECu]$	8.1	9.1	7.5
B_{bot}^{eq} $[km]$	44.8	30.0	37.8
$B_{bot}^{F_2}$ $[km]$		22.9	
$B_{top}^{F_2}$ $[km]$		69.8	57.8
Ratio		3.04	2.52

Table 3.9: Profiles characteristics for June 22th, 2006 at 10 UT

3.4.4 Worst month in low solar activity

The last situation we decided to study gathers most of the interesting observations from this section i.e.

- a slightly too high F_2 peak (235.1 km vs. 228.8 km measured) within the admitted accuracy ;
- a different E peak (2.4 MHz at 120 km vs. 2.6 MHz at 107.5 km) leading to small differences for h_mF_2 ($\Delta h_mF_2/h_mF_2 \simeq -1.8\%$), for the bottomside ($\Delta TEC_{bot}/TEC_{bot} \simeq -0.4\%$ for v1 and 4.0% for v2) or for the topside ($\Delta B_{top}^{F_2}/B_{top}^{F_2} \simeq -9.0\%$ and 0.2%) – the ionosonde value would thus have given slightly better results ;
- a too small electron concentration in the bottomside, higher for v2 with a smoothed valley (cf. figure 3.34) ;
- a clearly less dense topside in NeQuick latest version.

As for winter in high solar activity, the TEC dissociation reveals that the topside eroded only the half of what it should have (cf. table 3.4.4). This situation corresponds also to a higher transmission factor (3.50) so that it would be interesting to establish the potential existence of difficulties with high values of $M(3000)F_2$ studying other cases.

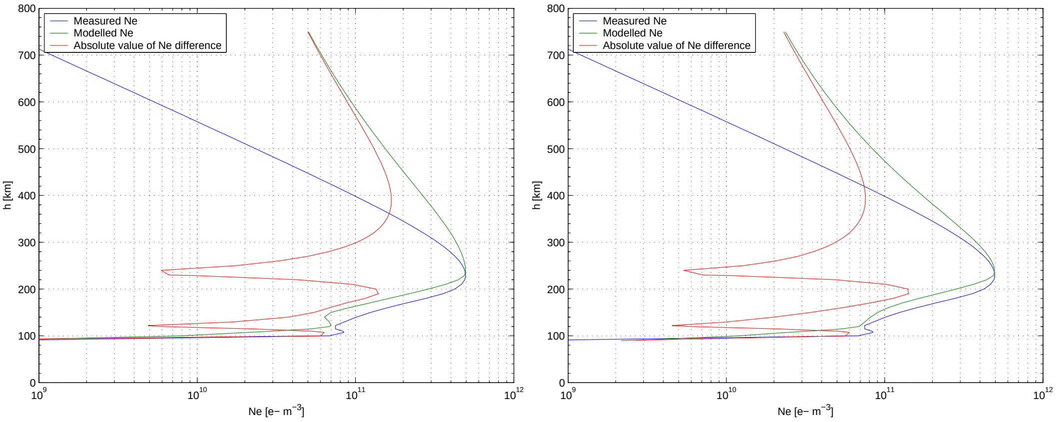

Figure 3.34: Measured and modelled profiles for December 9th, 2006 at 13 UT (v1 left and v2 right)

	Reference	v1	v2
$TEC\ [TECu]$	8.2	16.5	12.1
$TEC_{bot}\ [TECu]$	3.1	2.5	2.6
$TEC_{top}\ [TECu]$	5.1	14.0	9.5
$B_{bot}^{eq}\ [km]$	31.3	25.3	25.9
$B_{bot}^{F_2}\ [km]$		20.6	
$B_{top}^{F_2}\ [km]$		78.4	53.2
Ratio		3.80	2.58

Table 3.10: Profiles characteristics for December 9th, 2006 at 13 UT

3.4.5 Synthesis

The electron density profiles analysis allowed us to detail our description of the evolution between both versions of NeQuick and its remaining weaknesses considering different regions and characteristics.

- We highlighted the consequences of the unification of **topside** shape parameter k leading to better results especially in autumn and winter (e.g. second and fourth cases). Furthermore we showed through a TEC dissociation process that the topside remains the **region of prime interest**. It involves indeed **most of the total electron content** and it still displays **problematic situations** in the above-mentioned period (major residual overestimation) and during the rest of the year (small overestimation, e.g. September in high solar activity, or underestimation, e.g. June in low solar activity).

- We exposed also progresses in the **bottomside** which seemed generally not dense enough and showed **unrealistic features**. These where **suppressed** thanks to the developments in the E and F_1 layers resulting in a higher reinforcement than for other cases. This could partially explain the higher average TEC values for spring and summer in high solar activity which remain nevertheless too low. We illustrated that the bottomside could play a role in this underestimation so that it should be **investigated further** about various questions: a globally too high profile, differences for the E and F_1 peaks or F_2 **bottomside thickness parameter**. The latest appears indeed as a key feature of which the formulation did not change between NeQuick versions.

- Finally we exhibited the **interaction between bottom and topsides** which can present complementary weaknesses resulting in a global good adequation. More formally, the topside depends on the bottomside through its thickness and shape parameters ($B_{top}^{F_2} = k \ B_{bot}^{F_2}$). Moreover k formulation was derived using $B_{bot}^{F_2}$ current values so that it should be reassessed if the latter changed.

To go forward in this study, we could generalize the TEC dissociation process performing a similar statistical analysis to the one realized for global TEC. We should also consider other cases (other hours in particular) and investigate ionograms.

3.5 Discussion for navigation

NeQuick assessment provided us with some characteristic values of mid-latitude vertical TEC and associated TEC difference i.e. **residual modelling error**. The latter constitutes of course only a part of a more general ionospheric residual error we could be willing to estimate for the GALILEO ionospheric correction algorithm for single frequency users (cf. subsection 2.3.2). Indeed we used NeQuick in a different way primarily substituting measured DGS parameters to the CCIR maps and thus making it inconsistent to define an effective ionization level Az. Moreover we examined only the case of mid-latitudes, comparing vertical – and not slant – TEC computed from measurements at one station.

Nevertheless we can apply the concepts of DOP and mapping function (cf. subsections 2.2.2 and 2.2.3) to **convert** theoretically characteristic TEC values **to positioning errors** (cf. table 3.11).

1. We choose *average measured TEC and RMS TEC difference* from v2 yearly statistics (cf. table 3.4) as typical values for global and residual ionospheric effects i.e. before and after modelling. We are indeed not interested in negative differences as we want to consider the absolute distance from an accurate position. Note however the higher TEC values often observed (cf. figures 2.7 and 2.8) and the proportions of differences included in an interval of plus or minus RMS (77.6% for 2002 and 79.9% for 2006).

2. We *convert* them *to slant TEC* dividing by $\cos\chi_{IP} = \sqrt{1 - \left(\frac{R_E \sin\chi}{R_E + h_i}\right)^2} \simeq 0.7$ with an average satellite zenith angle $\chi = 50^\circ$ [RMI a], the thin shell height $h_i = 350\ km$ and the Earth radius $R_E = 6371\ km$.

3. We compute corresponding *range errors* I multiplying by $\frac{40.3}{f^2} \simeq 0.16\ m$ with $f = 1575.42\ MHz$ for the $E_2 - L_1 - E_1$ GALILEO carrier, interoperable with GPS L_1, which will be used by single frequency civilian receivers (cf. subsection 2.2.2).

4. Finally we obtain contributions to *horizontal and vertical accuracies* (ϵ_H^I and ϵ_V^I) employing average values of acceptable HDOP and VDOP respectively 2.5 and 3.5 [USACE, 2003].

	2002		2006	
	Original	Residual	Original	Residual
$vTEC\ [TECu]$	24.6	5.2	6.9	2.1
$sTEC\ [TECu]$	35.8	7.6	10.0	3.1
$I\ [m]$	5.8	1.2	1.6	0.5
$\epsilon_H^I\ [m]$	14.5	3.1	4.1	1.3
$\epsilon_V^I\ [m]$	20.3	4.3	5.7	1.8

Table 3.11: Characteristic values of ionospheric contributions to the positioning accuracy

Chapter 4

Conclusion and perspectives

4.1 NeQuick evolution

As a corner stone in the GALILEO single frequency ionospheric correction algorithm, the **NeQuick model evolves** thanks to several studies. The present assessment lies within this scope insofar as it investigates the model and its latest developments for a mid-latitude station collecting collocated ionosonde and GPS TEC data.

Conditioning NeQuick with ionosonde data, we first analyzed statistically the difference between GPS-derived vertical TEC for Dourbes station and corresponding modelled values for the latest years (for solar maximum in 2002 and minimum in 2006). We found **relative RMS values of 21% in 2002 and 31% in 2006** for the latest version of NeQuick associated respectively to **improvements of 36.4% and 43.8%** of the results for the official GALILEO baseline available on line. We attribute this progress to the **unification of the topside shape parameter** k as the two former formulas corresponded with periods exhibiting opposite behaviours. Indeed the average TEC, overestimated in autumn and winter on the one hand, decreases between both versions. On the other hand, in spring and summer, it increases towards measured values in high solar activity period but decreases a little below reference data for low solar activity level.

To deepen our understanding and confirm our assertions, we studied in detail four representative situations: two best days on relative RMS sense, near autumn equinox and summer solstice respectively for high and low solar activity levels, associated to average measured TEC maxima ; and two worst days, in december for both years, showing the lowest average TEC values.

In these cases, we examined the daily TEC graphs and electron density profiles for an hour near the measured TEC maximum around local noon.

- We verified the consequences of the modification in the **topside** description, improving drastically the worst cases but not necessarily the best ones e.g. low solar activity summer solstice. Moreover we noticed **remaining problems** in this region including the greatest part of the electron content thanks to a TEC dissociation process.

- The latter showed us indeed the apparent **compensation between bottom and topsides** sometimes hiding behind a global good adequation. Further progress in the topside could then come from changes in the bottomside as the thickness parameter of the first depends on the one of the second among others.
- Nevertheless we watched **unrealistic features disappearing** in the **bottomside** of which the possible underestimation diminishes thanks to evolutions in the E and F_1 layers. However in the chosen situations, the bottomside profile stays generally not dense enough so that we wondered about potential modifications in the F_2 **bottomside thickness parameter**, unchanged between NeQuick versions.

4.2 Future work

Even if these results appear already very promising, we would feel even more confident about them by getting more acquainted with the **data**. We should check and improve their quality and availability if possible, in particular for the ionosonde in 2006, and investigate other filtering methods than with the only geomagnetic indices. Studying the ionograms and considering other days and hours would help us understanding the underlying mechanisms.

On the one hand, a systematization of the **TEC dissociation process** and a **parameters analysis** could then provide us with some ideas of concrete evolutions to implement. On the other hand, a generalization to **other stations**, first at mid-latitudes then for all regions, would allow us to discuss the geographical representation of TEC.

Going back to a more global use of the model, we could afterwards analyse the performances **with the CCIR maps** and associated data ingestion and finally assess the **GALILEO single frequency ionospheric correction algorithm** with potential suitable evolutions of NeQuick.

This work follows an engineering master thesis undergone in the framework of an internship in the ESTEC Wave Interaction & Propagation section. These few months paved the way for a PhD thesis in the Unit of Geomatics at University of Liège. As a research fellow of the Belgian Fund for Scientific Research (FNRS), I hope to have the occasion to bring my contribution in these constantly evolving topics and to continue to share enthusiasm about science and technology as a Belgian scientist...

Appendix A

NeQuick details

A.1 Variables and parameters

Variables and units The main variables used in NeQuick and their units are given in table A.1.

Position and geomagnetism	
Height	h $[km]$
Latitude	ϕ $[^{\circ}]$
Longitude	θ $[^{\circ}]$
Magnetic latitude	λ $[^{\circ}]$
Magnetic dip	I $[^{\circ}]$
Modified dip latitude	μ $[^{\circ}]$ (cf. equation 2.1)
Solar activity	
Monthly mean of $F10.7$	Φ $[10^{-22}\ W\ m^{-2}\ Hz^{-1}]$
Monthly smoothed sunspot number	R_{12} (cf. equation 2.3)
Time and season	
Universal time	UT [hours]
Month	month
Zenith angle of the sun	χ $[^{\circ}]$

Table A.1: Main variables and units for NeQuick

Parameters and units The main parameters[1] used in NeQuick and their units are given in table A.2.

Electron density of layer L	N^L $[10^{11}\ el.\ m^3]$
Peak electron density of layer L	N^L_{max} $[10^{11}\ el.\ m^3]$
Global electron density at the peak height of layer L	N_mL $[10^{11}\ el.\ m^3]$
Peak height of layer L	h_mL $[km]$
Thickness parameter of layer L	B^L $[km]$
Critical frequency of layer L	f_oL $[MHz]$
Transmission factor	$M(3000)F_2$

Table A.2: Main parameters and units for NeQuick

A.2 Version 1 (ITU-R)

Electron density NeQuick models the *bottomside* ionosphere electron density (cf. equation A.1 when $100\ km \leq h \leq h_mF_2$) as a sum of five semi-Epstein layers (cf. equation 2.29) [Di Giovanni et Radicella, 1990][2]. The height h determines whether to use the top thickness parameter B^L_{top} or the bottom one B^L_{bot}. A fading out effect in the shape of a coefficient $\zeta(h)$ has also been added to the E and F_1 layers in the vicinity of the F_2 layer peak to avoid secondary maxima and ensure that the electron density at the F_2 layer peak corresponds exactly to f_0F_2 [Leitinger et al. 1999][3].

$$\begin{aligned}
N_{bot}(h) &= N^{F_2}(h) + N^{F_1}(h) + N^{E}(h) \\
&= 4\ N^{F_2}_{max}\ \frac{e^{\frac{h-h_mF_2}{B^{F_2}}}}{\left(1+e^{\frac{h-h_mF_2}{B^{F_2}}}\right)^2} + 4\ N^{F_1}_{max}\ \frac{e^{\zeta(h)\frac{h-h_mF_1}{B^{F_1}}}}{\left(1+e^{\zeta(h)\frac{h-h_mF_1}{B^{F_1}}}\right)^2} \\
&\qquad + 4\ N^{E}_{max}\ \frac{e^{\zeta(h)\frac{h-h_mE}{B^{E}}}}{\left(1+e^{\zeta(h)\frac{h-h_mE}{B^{E}}}\right)^2} \qquad \text{(A.1)}
\end{aligned}$$

$$\zeta(h) = e^{\frac{10}{1+2|h-h_mF_2|}}$$

---

[1] L stands for the layer index which possible values are E, F_1 and F_2.

[2] The latest publication including most of NeQuick equations is [Leitinger et al., 2005].

[3] The second and third terms corresponding to the F_1 and E layers are equalled to 0 if $|\zeta(h)\frac{h-h_mL}{B^L}| > 25$.

The *topside* ($h > h_m F_2$) corresponds to a sixth semi-Epstein layer with a height-dependent thickness parameter H.

$$N_{top}(h) = 4\ N_{max}^{F_2}\ \frac{e^{\frac{h-h_mF_2}{H}}}{\left(1+e^{\frac{h-h_mF_2}{H}}\right)^2} \tag{A.2}$$

For the *lowest part* of the ionosphere ($h < 100\ km$), a Chapman formulation (equation A.3) is used to avoid unrealistically high electron densities below 90 km from very thick lower F_1 layer in lower latitudes [Leitinger et al. 1999]. The equation for b is translated from the code[4].

$$N_{low}(h) = N_{bot}(100)\ e^{1-\ b\frac{h-100}{10}\ -\ e^{-\frac{h-100}{10}}} \tag{A.3}$$

$$\begin{aligned}
b &= 1 - \left[\frac{1}{N_{bot}(h)}\frac{dN_{bot}}{dh}(h)\right]_{h=100} \\
&= 1 - \frac{10}{N_{bot}(100)}\left[\frac{4\ N_{max}^{F_2}\left(1-e^{\frac{100-h_mF_2}{B_{bot}^{F_2}}}\right)\ e^{\frac{100-h_mF_2}{B_{bot}^{F_2}}}}{B_{bot}^{F_2}\left(1+e^{\frac{100-h_mF_2}{B_{bot}^{F_2}}}\right)^3}\right. \\
&\quad + \frac{4\ N_{max}^{F_1}\left(1-e^{\zeta(100)\frac{100-h_mF_1}{B_{bot}^{F_1}}}\right)\ e^{\zeta(100)\frac{100-h_mF_1}{B_{bot}^{F_1}}}}{B_{bot}^{F_1}\left(1+e^{\zeta(100)\frac{100-h_mF_1}{B_{bot}^{F_1}}}\right)^3} \\
&\quad \left. + \frac{4\ N_{max}^{E}\left(1-e^{\zeta(100)\frac{100-h_mE}{B_{bot}^{E}}}\right)\ e^{\zeta(100)\frac{100-h_mE}{B_{bot}^{E}}}}{B_{bot}^{E}\left(1+e^{\zeta(100)\frac{100-h_mE}{B_{bot}^{E}}}\right)^3}\right]
\end{aligned}$$

$$\zeta(100) = e^{\frac{10}{1+2|100-h_mF_2|}}$$

---

[4] The second and third terms in the parenthesis corresponding to the F_1 and E layers are equalled to 0 if $|\zeta(100)\frac{100-h_mL}{B^L}| > 25$.

Peak electron densities
The following equation [RADICELLA et ZHANG, 1995] was derived

- taking into account the fading out effect of E and F_1 layers near the F_2-layer peak to explain equation A.4,
- neglecting the E layer when considering the F_1 layer,
- but using original Epstein layers to compute their values at the other peaks in the following equations[5].

$$N_{max}^{F_2} = N(h_m F_2) = N_m F_2 \tag{A.4}$$

$$\begin{aligned} N_{max}^{F_1} &= N(h_m F_1) - N^{E}(h_m F_1) - N^{F_2}(h_m F_1) \\ &= N_m F_1 - N^{F_2}(h_m F_1) \end{aligned} \tag{A.5}$$

$$\begin{aligned} N_{max}^{E} &= N(h_m E) - N^{F_1}(h_m E) - N^{F_2}(h_m E) \\ &= N_m E - N^{F_1}(h_m E) - N^{F_2}(h_m E) \end{aligned} \tag{A.6}$$

The *global electron densities* at the peak height of layer L $N_m L$ are calculated from the critical frequencies $f_o L$ by means of equation 2.4 repeated here under with the appropriate units.

$$N_m L = 0.124\ f_o L^2 \tag{A.7}$$

Peak heights The following equations [RADICELLA et ZHANG, 1995] are based on DUDENEY's form [DUDENEY, 1983] of the BRADLEY and DUDENEY formula [BRADLEY et DUDENEY, 1973][6].

$$\begin{aligned} h_m F_2 &= \frac{1490\ MF}{M + DM} - 176 \\ DM &= \frac{0.253}{f_o F_2 / f_o E - 1.215} - 0.012 \\ MF &= M\sqrt{\frac{0.0196 M^2 + 1}{1.2967 M^2 - 1}} \\ M &= M(3000)F_2 \end{aligned} \tag{A.8}$$

---

[5] $N_{max}^{F_1}$ and N_{max}^{E} are limited at a minimum value of 0.05. The transition is computed by means of equation A.34 with $\alpha = 60$.

[6] The ratio $f_o F_2 / f_o E$ is limited at a minimum value of 1.75. The transition is computed by means of equation A.34 with $\alpha = 20$.

The following equation can be found into [Radicella et Zhang, 1995] ([Leitinger et al., 2005] for a correct version)[7].

$$h_m F_1 = 108.8 + 14\ N_m F_1 + 0.71\ |I| \tag{A.9}$$

$$h_m E = 120 km \tag{A.10}$$

Thickness parameters

The following equations can be found into [Radicella et Zhang, 1995].

$$\begin{aligned} B_{bot}^{F_2} &= \frac{0.385\ N_m F_2}{0.01\ (dN/dh)_{max}} \\ \ln\left((dN/dh)_{max}\right) &= -3.467 + 0.857 \ln\left(f_o F_2\right)^2 \\ &\quad + 2.02 \ln\left(M(3000)F_2\right) \end{aligned} \tag{A.11}$$

$(dN/dh)_{max}$ $[10^9\ el.\ m^{-3}\ km^{-1}]$ is the gradient of $N(h)$ at the characteristic point at the base of the F_2 layer i.e. the first derivative of equation 2.29 for F_2 layer at the inflection point.

The following equations can be found into [Radicella et Zhang, 1995] and [Radicella et Leitinger, 2001] ([Leitinger et al., 2005] for a correct version of H)[8].

$$H = B_{top}^{F_2} \left(1 + \frac{12.5(h - h_m F_2)}{100 B_{top}^{F_2} + 0.125(h - h_m F_2)}\right) \tag{A.12}$$

$$\begin{gathered} B_{top}^{F_2} = \frac{k\ B_{bot}^{F_2}}{\nu} \\ k = \begin{cases} -7.77 + 0.097 \left(\frac{h_m F_2}{B_{bot}^{F_2}}\right)^2 + 0.153\ N_m F_2 & \text{from October to March} \\ 6.705 - 0.014\ R_{12} - 0.008\ h_m F_2 & \text{from April to September} \end{cases} \\ 2 \leq k \leq 8 \\ \nu = (0.041163\ x - 0.183981)\ x + 1.424472 \\ x = \frac{k\ B_{bot}^{F_2} - 150}{100} \end{gathered} \tag{A.13}$$

---

[7] The transition at $I = 0$ is computed by means of equation A.34 with $\alpha = 12$.

[8] The transitions at $k = 2$ and $k = 8$ are computed by means of equation A.34 with $\alpha = 1$.

The formula for $B_{top}^{F_1}$ [Radicella et Zhang, 1995] is obtained from a simplification of the top F_1 semi-Epstein layer without fading out effect (equation 2.29 adapted to F_1), the shape of F_1 peak amplitude from equation A.2 and assuming the value of NF_1 at the F_2-layer peak[9].

$$\begin{aligned} NF_1(h_mF_2) &\approx 4\ N_{max}^{F_1}\ e^{-\frac{h_mF_2-h_mF_1}{B_{top}^{F_1}}} \\ &\approx 4\ \left(N_mF_1 - N^{F_2}(h_mF_1)\right)\ e^{-\frac{h_mF_2-h_mF_1}{B_{top}^{F_1}}} \\ &\approx 0.1\ N_mF_1 \end{aligned} \tag{A.14}$$

$$B_{top}^{F_1} = \frac{h_mF_2 - h_mF_1}{\ln\left(4\ \frac{N_mF_1 - N^{F_2}(h_mF_1)}{0.1\ N_mF_1}\right)} \tag{A.15}$$

The following equations can be found into [Radicella et Zhang, 1995].

$$B_{bot}^{F_1} = 0.7\ B_{top}^{F_1} \tag{A.16}$$

$$B_{top}^{E} = \begin{cases} 0.5\ B_{top}^{F_1} & \text{if } F_1 \text{ is present} \\ 7km & \text{if not} \end{cases} \tag{A.17}$$

$$B_{bot}^{E} = 5km \tag{A.18}$$

Critical frequencies and transmission factor The following equations [Leitinger et al. 1999] allow to compute the effective critical frequencies for the E and F_1 layers[10].

$$\begin{aligned} (f_oE)^2 &= a_E^2\ \sqrt{\Phi}\ \cos^{0.6}\chi_{eff} + 0.49 \\ a_E &= 1.112 - 0.019\ s_E\ \frac{e^{0.3\phi}-1}{e^{0.3\phi}+1} \\ s_E &= \begin{cases} -1 & \text{for "Winter" (November to February)} \\ 0 & \text{for "Equinox" (March, April, September and October)} \\ 1 & \text{for "Summer" (May to August)} \end{cases} \end{aligned} \tag{A.19}$$

---

[9] The ratio $4\frac{N_mF_1 - N^{F_2}(h_mF_1)}{0.1\ N_mF_1}$ is limited at a minimum value of 1.5. The transition is computed by means of equation A.34 with $\alpha = 20$.
$B_{top}^{F_1}$ is limited at a maximum value of $B_{bot}^{F_2} + 50$. The transition is computed by means of equation A.34 with $\alpha = 20$.

[10] The transitions between day and night for χ_{eff} and f_oF_1 at $\chi = \chi_0$ are computed by means of equation A.34 with $\alpha = 12$.

$$\chi_{eff} = \begin{cases} \chi & \text{for daytime } (\chi < \chi_0) \\ 90 - 0.24\ e^{20-0.2\chi} & \text{for nighttime } (\chi > \chi_0) \end{cases}$$

$\chi_0 = 86.23^\circ$ denotes the limit between day and night.

$$f_oF_1 = \begin{cases} 1.4\ f_oE & \text{for daytime } (\chi < \chi_0) \\ 0 & \text{for nighttime } (\chi > \chi_0) \end{cases} \tag{A.20}$$

The following equation can be found into [ITU-R, 1997]. This general form of the *numerical map* function Ω providing the evaluation of the monthly median of f_oF_2 or $M(3000)F_2$ has the shape of a Fourier time series.

$$\Omega(\phi,\theta,T) = \sum_{k=0}^{K} U_{0,k} G_k(\phi,\theta) + \sum_{j=1}^{H}\sum_{k=0}^{K} \left[U_{2j,k}\cos(jT) + U_{2j-1,k}\sin(jT)\right] G_k(\phi,\theta) \tag{A.21}$$

T denotes the universal time UT expressed as an angle ($-180^\circ \leq T \leq 180^\circ$).

H denotes the maximum number of harmonics used to represent the diurnal variation (6 for f_oF_2 and 4 for $M(3000)F_2$).

The coefficients $U_{i,k}$ are calculated from the CCIR files by linear combination with R_{12} as weighting coefficient (low solar activity: $R_{12} = 0$, $U^-_{i,k}$; high solar activity: $R_{12} = 100$, $U^+_{i,k}$).

$$U_{i,k} = U^-_{i,k}\left(1 - \frac{R_{12}}{100}\right) + U^+_{i,k}\frac{R_{12}}{100} \tag{A.22}$$

The geographic coordinate functions G_k are composed of three trigonometric functions in the following way.

$$G_k(\phi,\theta) = \sin^{q(k)}\mu\ \cos^{m(k)}\phi \left\{ \begin{array}{c} \cos \\ \sin \end{array} \right\} (m(k)\theta) \tag{A.23}$$

$q(k)$, the order in modified dip latitude, and $m(k)$, the order in longitude, are linked to the order of current harmonic.

The following formulation allows to *understand the code easier*.

$$\Omega(\mu,\phi,\theta,UT) = \sum_{L=1}^{q(1)+1} C_{i(1,L)}(UT)\ \sin^{L-1}\mu$$
$$+\sum_{j=2}^{k_1}\sum_{L=1}^{q(j)+1}\left[C_{i(j,L)}(UT)\ \cos\left((j-1)\theta\right)+C_{i(j,L)+1}(UT)\ \sin\left((j-1)\theta\right)\right]$$
$$\cos^{j-1}\phi\ \sin^{L-1}\mu \quad \text{(A.24)}$$

The first term could be included in the sum noticing that, for $j=1$, $\cos^{j-1}\phi = 1$, $\cos\left((j-1)\theta\right)=1$ and $\sin\left((j-1)\theta\right)=0$.

$q(j)$ denotes the maximum order in modified dip latitude for current order in longitude.

k_1 denotes the maximum order in longitude.

$$i(j,L)=\begin{cases} L & \text{if } j=1 \\ q(1)+2\left(\sum_{l=2}^{j-1} q(l)+j+L\right)-4 & \text{else}\end{cases}$$

$$C_i(UT) = U_{1,i}+\sum_{j=1}^{H} U_{2j,i}\sin\left(j\left(\frac{\pi}{12}UT-\pi\right)\right)+U_{2j+1,i}\cos\left(j\left(\frac{\pi}{12}UT-\pi\right)\right) \quad \text{(A.25)}$$

A.3 Version 2

Epstein parameters The first modifications related to the *peak electron densities* are translated from the code as they are not published yet.

As a consequence of the modified formulation of f_oF_1 (cf. equation A.32), $N_{max}^{F_1}$ is equalled to 0 if $f_oF_1 \leq 0.5$ and N_{max}^{E} is obtained from equation A.6 taking into account the disappearing of the F_1 layer. In the other case, $N_{max}^{F_1}$ and N_{max}^{E} are calculated by means of five successive iterations of equations A.26 and A.6[11].

$$N_{max}^{F_1} = N_mF_1 - N^{F_2}(h_mF_1) - N^E(h_mF_1) \tag{A.26}$$

The equations of the F_1 *peak height* and the *thickness parameters* from section A.2 were also updated as follows [Leitinger et al., 2005]. The latest and major revision concerns the topside shape parameter k [Coïsson et al., 2006].

$$h_mF_1 = \frac{h_mF_2 + h_mE}{2} \tag{A.27}$$

$$\begin{gathered} B_{top}^{F_2} = k \ B_{bot}^{F_2} \\ k = 3.22 - 0.0538 \ f_oF_2 - 0.00664 \ h_mF_2 + 0.113 \frac{h_mF_2}{B_{bot}^{F_2}} + 0.00257 \ R_{12} \\ k \geq 1 \end{gathered} \tag{A.28}$$

$$B_{top}^{F_1} = 0.3 \ (h_mF_2 - h_mF_1) \tag{A.29}$$

$$B_{bot}^{F_1} = 0.5 \ (h_mF_1 - h_mE) \tag{A.30}$$

$$B_{top}^{E} = \max \left\{ \begin{array}{c} 0.5 \ (h_mF_1 - h_mE) \\ 7km \end{array} \right\} \tag{A.31}$$

---

[11] N_{max}^{E} is still limited at a minimum value of 0.05 and the transition is still computed by means of equation A.34 with $\alpha = 60$.
At each iteration, $N_{max}^{F_1}$ is limited at a minimum value of $0.2 \ N_mF_1$. The transition is computed by means of equation A.34 with $\alpha = 1$.

Ionosonde parameters The following modifications to equation A.20 are described into [Leitinger et al., 2005].

$$f_oF_1 = \begin{cases} 1.4\ f_oE & f_oE \geq 2 \\ 0 & f_oE < 2 \\ 0.85\ 1.4\ f_oE & 1.4\ f_oE > 0.85\ f_oF_2 \end{cases} \tag{A.32}$$

The last condition corresponds a 15% reduction when f_oE is too close to f_oF_2.

A.4 Implementation tools

To represent the *piecewise function* $f(x)$ (cf. equation A.33), NeQuick uses an exponential transition (cf. equation A.34) depending on the (steepness) parameter α related to steepness of the transition between the two pieces $f_+(x)$ and $f_-(x)$. An interesting interpretation of this formulation is obtained considering the limits for $x \rightarrow \pm\infty$.

$$f(x) = \begin{cases} f_+(x) & \text{if } x > 0 \\ f_-(x) & \text{if } x < 0 \end{cases} \tag{A.33}$$

The following equation is translated from the code.

$$f(x) = \frac{f_+(x)\ e^{\alpha x} + f_-(x)}{e^{\alpha x} + 1} \tag{A.34}$$

Finally it is important to mention that NeQuick *restricts the argument of exponential functions* within the interval $[-80, 80]$ to avoid extreme values which could result (cf. equation A.35).

$$e_*^x = \begin{cases} e^{80} \approx 5.5406\ 10^{34} & \text{if } x > 80 \\ e^x & \text{if } -80 \leq x \leq 80 \\ e^{-80} \approx 1.8049\ 10^{-35} & \text{if } x < -80 \end{cases} \tag{A.35}$$

List of Figures

List of Tables

Bibliography

[Anderson et Fuller-Rowell, 1999] Anderson, D., Fuller-Rowell, T. "The Ionosphere" [on line]. In *Space Environment Topics*. Boulder: SEC, 1999, SE-14, 4 p. Available on `http://www.sec.noaa.gov/info/Iono.pdf`. (cited August 26th, 2007)

[Arbesser-Rastburg, 2006] Arbesser-Rastburg, B. "The Galileo Single Frequency Ionospheric Correction Algorithm" [on line]. Presented at the *3rd Third European Space Weather Week*, Brussels, 2006. Available on `http://sidc.oma.be/esww3/presentations/Session4/Arbesser.pdf`. (cited August 30th, 2007)

[Arbesser-Rastburg et Prieto-Cerdeira, 2005] Arbesser-Rastburg, B., Prieto-Cerdeira, R. *GALILEO Ionospheric Model for Single Frequency Receivers*. ESA-APPNG-SPEC/00344-BAR. Issue 5. Noordwijk: ESA, 2005, 21 p.

[Bidaine, 2006] Bidaine, B. *Ionosphere Crossing of GALILEO Signals*. M.S. thesis. Liège: ULg (FSA), 2006, 120 p.

[Bidaine et al, 2006] Bidaine, B., Prieto-Cerdeira, R., Orus, R. "NeQuick: In-Depth Analysis and New Developments". In *Proceedings of the 3rd ESA Workshop on Satellite Navigation User Equipment Technologies NAVITEC 2006* [CD-Rom], Noordwijk, The Netherlands, 2006.

[Bradley et Dudeney, 1973] Bradley, P. A., Dudeney, J. R. "A simple model of the vertical distribution of electron concentration in the ionosphere". *J. Atmos. Terr. Phys.*, 1973, Vol. 35, p. 2131-2146.

[Cander et al, 1998] Cander, L., Leitinger, R., Levy, M. "Ionospheric models including the auroral environment" [on line]. In *Proceedings of the ESA Workshop on Space Weather*, Noordwijk, The Netherlands, 1998. ESA WPP-155. Available on `http://esa-spaceweather.net/spweather/workshops/proceedings_w1/SESSION3/cander_ionmod.pdf`. (cited August 28th, 2007)

[Coïsson et al., 2006] Coïsson, P., Radicella, S. M., Leitinger, R., Nava, B. "Topside electron density in IRI and NeQuick: Features and limitations" [on line]. *Adv. Space Res.*, 2006, Vol. 37, No. 5, p. 937-942. Available on http://dx.doi.org/10.1016/j.asr.2005.09.015. (cited August 18th, 2007)

[Davies, 1990] Davies, K. *Ionospheric Radio.* London: Peter Peregrinus, 1990, 580 p. (IEE, Electromagnetic Wave Series 31). ISBN 0-86341-186X

[Di Giovanni et Radicella, 1990] Di Giovanni, G., Radicella, S. M. "An analytical model of the electron density profile in the ionosphere". *Adv. Space Res.*, 1990, Vol. 10, No. 11, p. 27-30.

[Dudeney, 1983] Dudeney, J. R. "The accuracy of simple methods for determining the height of the maximum electron concentration of the F_2-layer from scaled ionospheric characteristics" *J. Atmos. Terr. Phys.*, 1983, Vol. 45, p. 629-640.

[EPN Central Bureau] EUREF Permanent Network Central Bureau. *Site information > DOUR* [on line]. Available on http://www.epncb.oma.be/_trackingnetwork/siteinfo4onestation.php?station=DOUR. (cited August 27th, 2007)

[EU] EU. Directorate-General Energy and Transport. *GALILEO* [on line]. Available on http://ec.europa.eu/dgs/energy_transport/galileo. (cited August 27th, 2007)

[GFZ Potsdam] GeoForschungsZentrum Potsdam. *Indices of Global Geomagnetic Activity* [on line]. Available on http://www.gfz-potsdam.de/pb2/pb23/GeoMag/niemegk/kp_index/. (cited August 26th, 2007)

[Gérard, 2004] Gérard, J. C. "L'ionosphère" ["The ionosphere"]. In *Physique de l'atmosphère et de l'environnement terrestres* [*Physics of terrestrial atmosphere and environment*]. Master course ASTR0208. Liège: ULg (AGO), 2004, Chap. V, p. 152-167.

[Huang et Reinisch, 1996] Huang, X., Reinisch, B.W. "Vertical electron density profiles from the Digisonde network" [on line]. *Adv. Space Res.*, 1996, Vol. 18, No. 6, p. 121-129. Available on http://dx.doi.org/10.1016/0273-1177(95)00912-4. (cited August 20th, 2007)

[Hochegger et al., 2000] Hochegger, G., Nava, B., Radicella, S. M. et al. "A Family of Ionospheric Models for Different Uses" [on line]. *Phys. Chem. Earth (C)*, 2000, Vol. 25, No. 4, p. 307-310. Available on http://dx.doi.org/10.1016/S1464-1917(00)00022-2. (cited September 2nd, 2007)

[ICTP] ICTP. *Aeronomy and RadioPropagation Laboratory* [on line]. Available on http://arpl.ictp.trieste.it/. (cited August 30th, 2007)

[ITU-R, 1997] ITU-R. *Reference ionospheric characteristics.* Rec. ITU-R P.1239, 1997.

[ITU-R, 1999] ITU-R. *Choice of indices for long-term ionospheric predictions.* Rec. ITU-R P.371-8, 1999.

[ITU-R, 2002] ITU-R. *NeQuick software* [on line]. Rec. P.531, 2002. Available on http://www.itu.int/ITU-R/study-groups/software/rsg3-p531-electron-density.zip. (cited May 5th, 2006)

[Kintner et Ledvina, 2005] Kintner, P. M., Ledvina, B. M. "The ionosphere, radio navigation and global navigation satellite systems" [on line]. *Adv. Space Res.*, 2005, Vol. 35, No. 5, p. 788-811. Available on http://dx.doi.org/10.1016/j.asr.2004.12.076. (cited August 26th, 2007)

[Klobuchar, 1987] Klobuchar, J. A. "Ionospheric Time-Delay Algorithm for Single-Frequency GPS Users". *IEEE Transactions on Aerospace and Electronic Systems*, 1987, Vol. AES-23, No. 3, p. 324-331.

[Kunches, 1995] Kunches, J. "Navigation" [on line]. In *Space Environment Topics.* Boulder: SEC, 1995, SE-11, 4 p. Available on http://www.sec.noaa.gov/info/Navigation.pdf. (cited August 26th, 2007)

[Leitinger et al. 1999] Leitinger, R., Radicella, S. M., Nava, B., Hochegger, G., Hafher, J. "NeQuick - COSTprof - NeUoG-plas, a family of 3D electron density models". In *Proceedings of the COST 251 Madeira Workshop*, Madeira, 1999. p. 75-89.

[Leitinger et al., 2005] Leitinger, R., Zhang, M.-L., Radicella, S. M. "An improved bottomside for the ionospheric electron density model NeQuick" [on line]. *Ann. Geophys.*, 2005, Vol. 48, No. 3, p. 525-534. Available on http://www.earth-prints.org/bitstream/2122/920/1/12Leitinger1.pdf. (cited August 18th, 2007)

[Nava, 2007] Nava, B. *Personnal communication.* 2007.

[NGDC] National Geophysical Data Center. Solar Terrestrial Physics. *Solar and Interplanetary Phenomena: Penticton/Ottawa 2800 MHz Solar Flux* [on line]. Available on http://www.ngdc.noaa.gov/stp/SOLAR/FLUX/flux.html. (cited August 26th, 2007)

[NOAA, 2007] NOAA. "Researchers find Global Positioning System is significantly impacted by powerful solar radio burst" [on line]. *NOAA News Story Archive*, April 4th, 2007. Available on http://www.noaanews.noaa.gov/stories2007/s2831.htm. (cited August 21st, 2007)

[Odijk, 2002] Odijk, D. "The ionospheric error in GPS observations" [on line]. In *Fast precise GPS positioning in the presence of ionospheric delays*. Ph.D thesis. Delft: TU Delft, 2002, PoG 52, Chap. 4, p. 69-102. ISBN 90-6132-278-2 Available on http://www.ncg.knaw.nl/Publicaties/Geodesy/pdf/52Odijk.pdf. (cited August 27th, 2007)

[Pierrard et Warnant, 2007] Pierrard, V., Warnant, R. *Physique de la haute atmosphère et de l'espace* [*Upper atmosphere and space physics*]. Master course PHY2162. Louvain-la-Neuve: UCL, 2007.

[Piggot et Rawer, 1978] Piggot, P., Rawer, K. "Determination of hourly numerical values" [on line]. In *URSI handbook of ionogram interpretation and reduction*. 2nd ed. Report UAG-23A. Boulder: World Data Center A for Solar-Terrestrial Physics, 1978, Chap. 2, p. 29-64. Available on http://www.ips.gov.au/IPSHosted/INAG/uag_23a/UAG_23A_indexed.pdf. (cited August 18th, 2007)

[Prieto-Cerdeira et al, 2006] Prieto-Cerdeira, R., Orus, R., Arbesser-Rastburg, B. "Assessment of the Ionospheric correction algorithm for GALILEO Single Frequency Receivers". In *Proceedings of the 3rd ESA Workshop on Satellite Navigation User Equipment Technologies NAVITEC 2006* [CD-Rom], Noordwijk, The Netherlands, 2006.

[Radicella, 2003] Radicella, S. M., Arbesser-Rastburg, B., Leitinger, R. "An improved Ionospheric Correction Model for Single Frequency Satellite Navigation". Presented at the *7th SBAS meeting*, Graz, 2003.

[Radicella et Leitinger, 2001] Radicella, S. M., Leitinger, R. "The evolution of the DGR approach to model electron density profiles" [on line]. *Adv. Space Res.*, 2001, Vol. 27, No. 1, p. 35-40. Available on http://dx.doi.org/10.1016/S0273-1177(00)00138-1. (cited September 2nd, 2007)

[Radicella et Zhang, 1995] Radicella, S. M., Zhang, M.-L. "The improved DGR analytical model of electron density height profile and total electron content in the ionosphere". *Ann. Geofis*, 1995, Vol. XXXVIII, No. 1, p. 35-41.

[Rawer, 1963] Rawer, K. "Propagation of Decameter Waves (HF-Band)". In Landmark, B. Ed. *Meteorological and Astronomical Influences on Radio Wave Propagation*. New York: Academic Press, 1963, Chap. 11, p. 221-250.

[Rawer, 1982] Rawer, K. "Replacement of the present sub-peak plasma density profile by a unique expression". *Adv. Space Res.*, 1982, Vol. 2, No. 10, p. 183-190.

[Reinisch et Huang, 2001] Reinisch, B.W., Huang, X., "Deducing topside profiles and total electron content from bottomside ionograms" [on line]. *Adv. Space Res.*, 2001, Vol. 27, No. 1, p. 23-30. Available on `http://dx.doi.org/10.1016/S0273-1177(00)00136-8`. (cited August 20th, 2007)

[Reinisch et al, 2005] Reinisch, B. W., Huang, X., Galkin, I. A., Paznukhov, V., Kozlov, A. "Recent advances in real-time analysis of ionograms and ionospheric drift measurements with digisondes" [on line]. *J. Atmos. Sol.-Terr. Phys.*, 2005, Vol. 67, No. 12, p. 1054-1062. Available on `http://dx.doi.org/10.1016/j.jastp.2005.01.009`. (cited August 20th, 2007)

[RMI a] Royal Meteorological Institute. *Atmospheric Effects in Global Navigation Satellite Systems* [on line]. Available on `http://gpsatm.oma.be`. (cited August 26th, 2007)

[RMI b] RMI. *Centre de Physique du Globe de l'IRM à Dourbes* [*RMI Geophysical Centre at Dourbes*] [on line]. Available on `http://www.meteo.be/CPG/Index.htm`. (cited August 27th, 2007)

[RMI et UMLCAR] RMI, UMLCAR. *Dourbes Digisonde 256* [on line]. Available on `http://digisonde.oma.be/`. (cited August 27th, 2007)

[Shimazaki, 1955] Shimazaki, T. "World-wide variations in the height of the maximum electron density of the ionospheric F_2 layer". *J. Radio Res. Labs.*, Japan, 1955, Vol. 2, p. 85-97.

[SIDC] Solar Influences Data analysis Center. World Data Center for the Sunspot Index. Royal Observatory of Belgium. *Monthly Report on the International Sunspot Number. Online catalogue of the sunspot index* [on line]. Available on `http://www.sidc.be/sunspot-data`. (cited September 2nd, 2007)

[Stankov, 2002] Stankov, S.M. *Ionosphere-plasmasphere system behaviour at disturbed and extreme magnetic conditions*. OSTC Final Scientific Report. Brussels: Royal Meteorological Institute of Belgium, 2002.

[The Aerospace Corporation] The Aerospace Corporation. *GPS Primer* [on line]. Available on http://www.aero.org/education/primers/gps/index.html. (cited August 27th, 2007)

[UMLCAR] University Massachusetts Lowell Center for Atmospheric Research. *Lowell Digisonde* [on line]. Available on http://ulcar.uml.edu/digisonde.html. (cited August 27th, 2007)

[USACE, 2003] US Army Corps of Engineers. *Engineering and Design - NAVSTAR Global Positioning System Surveying* [on line]. Engineer Manual 1110-1-1003. Washington DC: USACE, 2003. Available on http://www.usace.army.mil/publications/eng-manuals/em1110-1-1003/toc.htm. (cited August 27th, 2007)

[Warnant, 1996] Warnant, R. *Etude du comportement du Contenu Electronique Total et de ses irrégularités dans une station de latitude moyenne. Application aux calculs de positions relatives par le GPS* [*Study of the behaviour of Total Electron Content and its irregularities in a mid-latitude station. Application to the calculations of relative positions by means of the GPS*]. Ph.D thesis. Brussels: Royal Observatory of Belgium, 1996, Série Géophysique (N. Hors-Série).

[Warnant, 2006] Warnant, R. *Topographie : théorie des erreurs et GNSS* [*Topography: error theory and GNSS*]. Master course GEOG0615. Liège: ULg (Geography), 2006.

[Warnant et Pottiaux, 2000] Warnant, R., Pottiaux, E. "The increase of the ionospheric activity as measured by GPS" [on line]. *Earth Planets Space*, 2000, Vol. 52, No. 11, pp. 1055-1060. Available on http://www.terrapub.co.jp/journals/EPS/pdf/5211/52111055.pdf. (cited August 20th, 2007)

[WDC Geomagnetism] World Data Center for Geomagnetism, Kyoto. *Geomagnetic Data Service* [on line]. Available on http://swdcwww.kugi.kyoto-u.ac.jp/wdc/Sec3.html. (cited August 26th, 2007)

[Weisstein a] Weisstein, E. W. "Legendre-Gauss Quadrature" [on line]. In *MathWorld - A Wolfram Web Resource*. Available on http://mathworld.wolfram.com/Legendre-GaussQuadrature.html. (cited August 25th, 2007)

[Weisstein b] Weisstein, E. W. "Richardson Extrapolation" [on line]. In *MathWorld - A Wolfram Web Resource*. Available on http://mathworld.wolfram.com/RichardsonExtrapolation.html. (cited August 25th, 2007)

[WEISSTEIN c] WEISSTEIN, E. W. "Trapezoidal Rule" [on line]. In *MathWorld - A Wolfram Web Resource*. Available on http://mathworld.wolfram.com/TrapezoidalRule.html. (cited August 25th, 2007)

[ZHANG et al., 1999] ZHANG, S.-R., FUKAO, S., OLIVER, W. L., OTSUKA, Y. "The height of the maximum ionospheric electron density over the MU radar" [on line]. *J. Atmos. Sol.-Terr. Phys.*, 1999, Vol. 61, No. 18, p. 1367-1383. Available on http://dx.doi.org/10.1016/S1364-6826(99)00088-7. (cited August 20th, 2007)